Probing topological states, Fermi surface and scattering mechanism in some three-dimensional Dirac semimetals

By

ARNAB KUMAR PARIARI

PHYS05201304007

Condensed Matter Physics Division

Saha Institute of Nuclear Physics, Kolkata

A thesis submitted to the
Board of Studies in Physical Sciences

In partial fulfillment of requirements

for the Degree of

DOCTOR OF PHILOSOPHY

of

HOMI BHABHA NATIONAL INSTITUTE

June, 2018

Homi Bhabha National Institute[1]

Recommendations of the Viva Voce Committee

As members of the Viva Voce Committee, we certify that we have read the dissertation prepared by Arnab Kumar Pariari entitled " Probing topological states, Fermi surface and scattering mechanism in some three-dimensional Dirac semimetals" and recommend that it may be accepted as fulfilling the thesis requirement for the award of Degree of Doctor of Philosophy.

Chairman - Prof. Satyaranjan Bhattacharyya	SBhattacharyya	**Date:** 13/8/2018
Guide / Convener - Prof. Prabhat Mandal	P. Mandal	**Date:** 13/8/2018
Co-guide -		**Date:**
Examiner - Prof. Goutam Sheet		**Date:** 13/08/2018
Member 1- Prof. Biswajit Karmakar	Biswajit Karmakar	**Date:** 13/8/18
Member 2- Prof. Arti Garg		**Date:** 13/8/2018

Final approval and acceptance of this thesis is contingent upon the candidate's submission of the final copies of the thesis to HBNI.

I hereby certify that I have read this thesis prepared under my direction and recommend that it may be accepted as fulfilling the thesis requirement.

Date: 13.08.2018

Place: SINP, Kolkata

P. Mandal.

Prof. Prabhat Mandal

Guide

STATEMENT BY AUTHOR

This dissertation has been submitted in partial fulfillment of requirements for an advanced degree at Homi Bhabha National Institute (HBNI) and is deposited in the Library to be made available to borrowers under rules of the HBNI.

Brief quotations from this dissertation are allowable without special permission, provided that accurate acknowledgement of source is made. Requests for permission for extended quotation from or reproduction of this manuscript in whole or in part may be granted by the Competent Authority of HBNI when in his or her judgment the proposed use of the material is in the interests of scholarship. In all other instances, however, permission must be obtained from the author.

Arnab Kumar Pariari

Arnab Kumar Pariari

DECLARATION

I, hereby declare that the investigation presented in the thesis has been carried out by me. The work is original and has not been submitted earlier as a whole or in part for a degree / diploma at this or any other Institution / University.

Arnab Kumar Pariari

Arnab Kumar Pariari

List of Publications

A. Publications in peer-reviewed journals
(Included in the thesis)

1. "Probing the Fermi surface of three-dimensional Dirac semimetal Cd_3As_2 through the de Haas–van Alphen technique", **Arnab Pariari**, P. Dutta, and P. Mandal, *Physical Review B*, **2015**, *91*, 155139.

2. "Tuning the scattering mechanism in the three-dimensional Dirac semimetal Cd3As2", **Arnab Pariari**, N. Khan, R. Singha, B. Satpati, and P. Mandal, *Physical Review B*, **2016**, *94*, 165139.

3. "Coexistence of topological Dirac fermions in the surface and three-dimensional Dirac cone state in the bulk of $ZrTe_5$ single crystal", **Arnab Pariari** and Prabhat Mandal, *Scientific Reports*, **2017**, *7*, 40327.

4. "Anisotropic transverse magnetoresistance and Fermi surface in $TaSb_2$", **Arnab Pariari**, Ratnadwip Singha, Shubhankar Roy, Biswarup Satpati, Prabhat Mandal, *Scientific Reports,* **2018**, 8, 10527.

(Not included in the thesis)

5. "Large nonsaturating magnetoresistance and signature of nondegenerate Dirac nodes in ZrSiS", Ratnadwip Singha, **Arnab Kumar Pariari**, Biswarup Satpati, and Prabhat Mandal, *Proceedings of the National Academy of Sciences*, **2017**, *114*, 2468-2473.

6. "Prominent metallic surface conduction and the singular magnetic response of topological Dirac fermion in three-dimensional topological insulator $Bi_{1.5}Sb_{0.5}Te_{1.7}Se_{1.3}$", Prithwish Dutta, **Arnab Pariari**, Prabhat Mandal, *Scientific Reports*, **2017**, *7*, 4883.

7. "Magnetotransport properties and evidence of a topological insulating state in LaSbTe", Ratnadwip Singha, **Arnab Pariari**, Biswarup Satpati, Prabhat Mandal, *Physical Review B*, **2017**, *96*, 245138.

8. "Probing the Fermi surface and magnetotransport properties in $MoAs_2$", Ratnadwip Singha, **Arnab Pariari**, Prabhat Mandal, Gaurav Kumar Gupta, Tanmoy Das, *Physical Review B*, **2018**, *97*, 155120.

9. “Magneto-transport properties of proposed triply degenerate topological semimetal $Pd_3Bi_2S_2$”, Shubhankar Roy, **Arnab Pariari**, Ratnadwip Singha, Biswarup Satpati, Prabhat Mandal, *Applied Physics Letters*, **2018**, *112*, 162402.

10. “Probing lattice dynamics and electron-phonon coupling in topological nodal-line semimetal ZrSiS”, Ratnadwip Singha, Sudeshna Samanta, Swastika Chatterjee, **Arnab Pariari**, Dipanwita Majumdar, Biswarup Satpati, Lin Wang, Achintya Singha, Prabhat Mandal, *Physical Review B*, **2018**, *97*, 094112.

11. “Effect of pressure on normal and superconducting state properties of iron based superconductor $PrFeAsO_{0.6}F_y$ (y = 0.12, 0.14)”, S. Arumugam, C. Ganguli, R. Thiyagarajan, D. Bhoi, G. Kalai Selvan, K. Manikandan, **Arnab Pariari**, P. Mandal, and Y. Uwatoko, *Scientific Reports*, **2017**, 7, 11731.

12. “Planar Hall effect in the type-II Dirac semimetal VAl_3”, Ratnadwip Singha, Shubhankar Roy, **Arnab Pariari**, Biswarup Satpati, and Prabhat Mandal, *Physicsl Review B 98,* **2018**, 98, 081103(R).

B. Conference papers/presentations

1. “Three-dimensional Dirac Semimetal Cd3As2 as a potential candidate for thermoelectric applications", **Arnab Pariari**, Nazir Khan, and Prabhat Mandal, presented in International Workshop on Advanced Materials (**IWAM-2017**) and proceedings will be published by American Institute of Physics.

2. “Coexistence of topological Dirac fermions in the surface and three-dimensional Dirac cone state in the bulk of $ZrTe_5$ single crystal", **Arnab Pariari** and Prabhat Mandal, presented in **Young Physicists Colloquium - 2016** (organized by Indian Physical Society, August 2016).

3. “Prominent metallic surface conduction and the singular magnetic response of topological Dirac fermion in three-dimensional topological insulator $Bi_{1.5}Sb_{0.5}Te_{1.7}Se_{1.3}$", Prithwish Dutta, **Arnab Pariari**, and Prabhat Mandal, presented in **Young Physicists**

Colloquium - 2017 (organized by Indian Physical Society, August 2017).

4. "Magnetotransport properties and evidence of a topological insulating state in LaSbTe", Ratnadwip Singha, **Arnab Pariari**, Biswarup Satpati, and Prabhat Mandal, presented in **National Conference on Quantum Condensed Matter** at IISER Mohali, India, July, 2018

Arnab Kumar Pariari

Arnab Kumar Pariari

DEDICATIONS

This Thesis is dedicated to
my Wife,
and
my Guide

ACKNOWLEDGEMENTS

At first, I would like to thank my advisor Prof. Prabhat Mandal for providing me the opportunity to work under him, his guidance and support. He has been a constant source of encouragement and advice throughout my graduate studies. He made me realise in every step of my thesis work that we have to keep fighting against any sorts of difficulty with our limited facility to get success. He also made me understand that, as there is no well-defined path to success in the field of research, we have to keep trying. Moreover, I am grateful for the freedom he gave me to pursue individual interests in my research work. He always encouraged and allowed me to consult with the experts in relevant areas, and introduced me with the researchers from different institutes. Apart from the academic relation, I have discovered him as a friend in need. When we felt any sorts of difficulty or got sick, he stood beside us physically, mentally and financially. I sincerely express my gratitude to Prof. Prabhat Mandal for every single aspect of my graduate research. He is a true friend, philosopher and guide of mine.

I am also indebted to my seniors Dr. Dilip Kumar Bhoi, Dr. Nazir Khan, Dr. Arindam Midya, Prithwish Dutta, Dr. Moumita Nandi, Dr. Prosenjit Sarkar, Dr. Biswanath Samantaray, and our laboratory technician Arun Kumar Pal for introducing me with different experimental techniques and with different instruments. I thank Dr. Dilip Kumar Bhoi for introducing me into the group and helping me to settle down. I am lucky to have a fully furnished laboratory to execute my thesis work, which mostly has been designed and built by Dr. Nazir Khan, Dr. Arindam Midya, Dr. Dilip Kumar Bhoi, and Arun Kumar Pal. I am highly obliged to all of them. I thank all of my teammates Dr. Nazir Khan, Prithwish Dutta, Ratnadwip Singha, and Shubhankar Roy.

Without their help, it would not be possible for me to complete the thesis work. I thank Prof. Biswarup Satpati for TEM characterization of our grown single crystal samples. He was always ready to help and sent results on short notices. The timely response from him was crucially important in our competitive research. I am truly lucky to have greatly active and highly motivated researcher Ratnadwip Singha and Shubhankar Roy as my juniors. Without them, it would not be possible to publish several standard works on different materials from our laboratory. I thank my other labmates Susmita Roy and Moumita Das for their cooperation in sharing all the lab equipments. I also thank Susmita Roy for being a good friend.

I thank Prof. Arti Garg, Prof. P.K. Mohanty, Prof. Bikas Chakrabarti, Prof. Biswajit Karmakar, Prof. Biswarup Satpati, Prof. Palash Baran Pal, and Prof. Asit Kumar De for introducing me with the several advance topics of Condensed matter physics, Mathematics and Quantum mechanics. I am grateful to Prof. Arti Garg for giving me her valuable time, when I needed any theoretical help and support on fundamental understandings. I also thankful to her for her encouragement. I am grateful to Prof. P.K. Mohanty for his constant support and several sudden hug for encouragement. I am obliged to Amit Kumar Chatterjee for being a great friend in my personal life.

I am very thankful to Saha Institute of Nuclear Physics, HBNI, Department of Atomic energy, Government of India for the generous financial support through the student fellowship and travel grants, and for the research facilities. I am also thankful to Department of Science and Technology, Government of India for financially supporting me through the INSPIRE fellowship during my B. Sc and M.Sc period.

I am extremely grateful to my parents for bringing me into the earth, for their love, for their encouragement to assimilate the right cultural and for the financial support in early stage of my career. Finally, I express my deepest gratitude to my wife Priyanka for always being there, for bearing my complaints, for sharing my happiness, for encouragement, for many personal sacrifices, and for boosting my self-confidence whenever it was low. I am extremely grateful to her for the care she has taken during my PhD tenure, and for making me realize the impact of love in human life from family members.

Contents

Synopsis **i**

List of figures **xiv**

List of tables **xxx**

1 Introduction **1**

1.1 Band theory and conventional electronic phases 2

1.2 The Integer Quantum Hall State and introduction of topology in electronic systems 4

1.2.1 Experimental discovery and the strange observation 4

1.2.2 Topology in Geometry 6

1.2.3 Topology in Quantum Hall Physics 8

1.3 Quantum Spin Hall (QSH) State 10

1.3.1 Discovery of QSH effect and failure of TKNN characterization 10

1.3.2 Role of time-reversal symmetry 12

1.3.3 $\mathbb{Z}_2$ topological classification 14

1.4 Three-dimensional Topological Insulators 16

1.4.1 Weak topological insulators 16

1.4.2 Strong topological insulators 18

1.5 Three-dimensional Dirac semimetal 21

1.5.1 3D Dirac semimetal state at quantum critical point 22

1.5.2 Crystalline symmetry protected 3D Dirac semimetal 25

1.5.3 Understanding TWS as a transmuted state of TDS 27

1.5.4 Experimental discovery of TDS 29

1.6 Context, goal and outline of the thesis 30

2 Experimental details **33**

2.1 Sample preparation 33

2.1.1 Chemical vapor transport technique 34

2.2 Characterization 36

2.2.1 Powder x-ray diffraction 36

2.2.2 Transmission electron microscope (TEM) 38

2.3 Physical and magnetic properties measurements 41
2.3.1 Electrical resistivity 41
2.3.2 Seebeck coefficient 43
2.3.3 dc magnetization 44

3 Probing the Fermi surface of three-dimensional Dirac semimetal Cd_3As_2 through the de Haas-van Alphen technique 47
3.1 Introduction 47
3.2 Sample preparation, characterization, and experimental details . . . 49
3.3 Results and Discussions 50
3.4 Conclusion 59

4 Tuning the scattering mechanism in three-dimensional Dirac semimetal Cd_3As_2 60
4.1 Introduction 60
4.2 Sample preparation, characterization, and experimental details . . . 62
4.3 Results and Discussions 64
4.3.1 Resistivity and Hall resistance of Cd_3As_2 single crystal . . . 64
4.3.2 Temperature and magnetic field dependence of the Seebeck coefficient of Cd_3As_2 65
4.3.3 Analysis of the magnetic field evolution of the scattering time in Cd_3As_2 67
4.3.4 Tuning of charge carrier by In doping 69
4.3.5 Analysis of magnetoresistance and Shubnikov-de Haas oscillations in $(Cd_{0.98}In_{0.02})_3As_2$ crystal 70
4.3.6 Temperature dependence of S in $(Cd_{0.98}In_{0.02})_3As_2$ 74
4.3.7 Magnetotransport and thermoelectric properties of $(Cd_{0.96}In_{0.04})_3As_2$ crystal 75
4.4 Conclusion 79

5 Coexistence of topological Dirac fermions on the surface and three-dimensional Dirac cone state in the bulk of $ZrTe_5$ single crystal 81
5.1 Introduction 81
5.2 Sample preparation, characterization, and experimental details . . . 83
5.3 Results 85

5.3.1 Temperature dependence of resistivity both in presence and absence of external magnetic field . . . 85
5.3.2 Hall resistivity and transverse magnetoresistance . . . 86
5.3.3 Longitudinal magnetoresistance and Chiral anomaly . . . 88
5.3.4 Signature of topological surface state from magnetization measurements . . . 92
5.4 Discussion . . . 96
5.5 Conclusion . . . 98

6 Anisotropic transverse magnetoresistance and Fermi surface in $TaSb_2$ 99
6.1 Introduction . . . 99
6.2 Sample preparation, characterization, and experimental details . . . 100
6.2.1 Sample preparation . . . 100
6.2.2 Characterization . . . 101
6.2.3 Experimental details . . . 103
6.3 Results . . . 103
6.3.1 Temperature dependence of resistivity . . . 103
6.3.2 Angular dependence of magnetoresistance . . . 105
6.3.3 Field dependence of MR . . . 107
6.3.4 Hall measurements and multi-band analysis . . . 108
6.3.5 Probing the Fermi surface through de Haas-van Alphen oscillation . . . 111
6.4 Discussions . . . 118
6.5 Conclusion . . . 120

7 Summary and future directions 122
7.1 Summary . . . 122
7.2 Future directions . . . 125
7.2.1 Thickness-dependent magneto-transport in thin films of Dirac/Weyl semimetals . . . 126
7.2.2 Study of quantum phenomena under extreme conditions (high magnetic field and pressure) . . . 127

7.2.3 Probing electronic transport and Fermi surface of novel materials beyond Dirac/Weyl semimetals 127

8 Appendix **129**

8.1 Appendix A 129

8.1.1 Magnetization measurements of standard diamagnetic and paramagnetic compounds 129

8.1.2 Magnetization measurements of a representative 3D topological insulator 131

References **132**

SYNOPSIS

Introduction: Over the last decade, the topological insulating phase of matter has emerged through the continuous evolution from two-dimensional (2D) quantum spin Hall (QSH) state to three-dimensional (3D) topological insulators (TI) [1]. The materials with 3D topological insulating state exhibit bulk band gap like an ordinary insulator, but have protected conducting state on the surfaces. The novelty of this conducting surface state is the linear energy-momentum dispersion of charge carriers, unlike quadratic dispersion in conventional materials, and the spin-momentum locking associated to the motion of the charge carrier, which makes the transport insensitive to non-magnetic impurity [1]. 3D Dirac and Weyl type electronic materials are the most recently (2014-15) discovered quantum phases of matter, described as topological semimetal (TSM) [2, 3, 4]. Unlike topological insulator, they exhibit semimetallic bulk with linear electronic dispersion and as a consequence, the quasi-particles behave as the relativistic Dirac/Weyl fermion in three dimensions. The surface state of TSMs is also distinct from the closed constant energy contour in 3D TIs, identified as Fermi arc. Due to the unique band topology, these materials show different exotic electronic properties of both fundamental and technological interest, mostly governed by the bulk electronic contribution [5, 6, 7, 8]. The aim of the present thesis work is, to explore different exotic magneto-transport properties, nature of Fermi surfaces, topological response and thermoelectronic properties in some 3D Dirac semimetals.

Experimental Details: The materials which have been studied in this thesis work are Cd_3As_2, $ZrTe_5$ and $TaSb_2$. Single crystals were grown by standard vapor transport technique. Phase purity and the structural analysis were done by using high-resolution powder x-ray diffraction (XRD) and high-resolution trans-

mission electron microscopy (HRTEM). The transport measurements were done by standard four-probe technique in a 9 T physical property measurement system (Quantum Design) and cryogen free measurement system (Cryogenic). Magnetization was measured in a 7 T MPMS3 (Quantum Design).

Probing the Fermi surface of three-dimensional Dirac semimetal Cd_3As_2 through the de Haas-van Alphen technique: After the discovery of 3D Dirac semimetal phase in Cd_3As_2, angle-resolved photoemission spectroscopy (ARPES) measurements have shown that two almost identical ellipsoidal Fermi surfaces are located on opposite sides of the Γ point along the k_z direction [9]. Band structure calculation suggests that these two Fermi pockets touch each other at the critical value of the Fermi energy ($\sim$133 meV), known as Lifshitz saddle point [8]. The Fermi energy of Cd_3As_2 has been reported to have much larger value than the critical one [5]. So, the complex mixing of Fermi surfaces is expected to happen above the Lifshitz transition. However, the analysis of Shubnikov-de Haas (SdH) oscillations suggests the existence of single or two equivalent Fermi surface cross sections, associated to the single frequency of oscillation [5]. In this context, probing the Fermi surface (FS) of Cd_3As_2 using the de Haas-van Alphen (dHvA) oscillation, which has been established to be more accurate technique due to absence of local heating and quantum interference effects or noise from the electrical contacts, may provide some finer details of the FS [10].

As shown in Fig.1(a), good match between the experimental and calculated intensities in XRD peaks implies the absence of any impurity phase. Resistivity (ρ_{xx}) shows metallic behaviour over the whole range of temperature with a residual resistivity ratio $[\rho_{xx}(300\text{ K})/\rho_{xx}(2\text{ K})] \sim 6$ [Fig.1(b)]. Large and non-saturating MR ($= \frac{\rho_{xx}(B)-\rho_{xx}(0)}{\rho_{xx}(0)} \times 100\%$) with prominent signature of Shubnikov-de Haas oscilla-

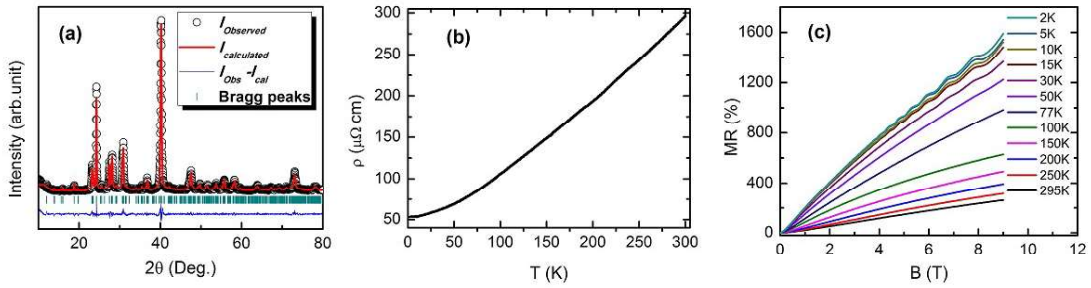

Figure 1: (a) X-ray diffraction pattern of powdered sample of Cd_3As_2 single crystal. (b) Resistivity (ρ_{xx}) as a function of temperature. (c) Magnetic field (B) dependence of the transverse magnetoresistance (TMR) when B||[100] and I||[012] direction.

tions are evident from Figure 1(c).

The fast Fourier transform (FFT) spectra of ΔR_{xx} versus $1/B$ curve shows only

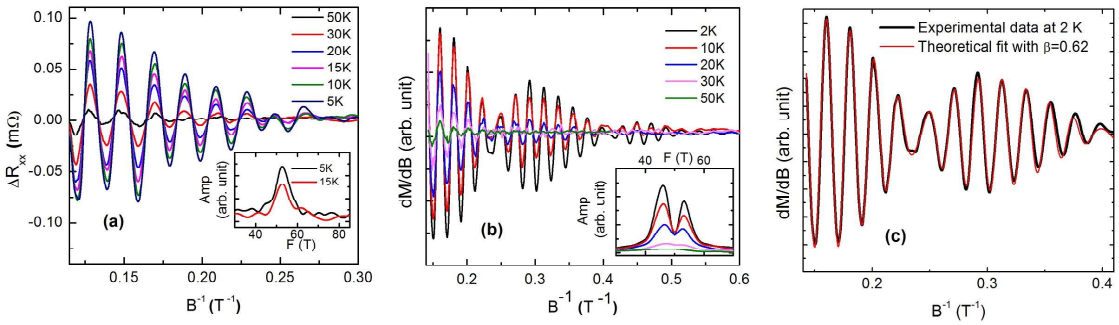

Figure 2: (a) The oscillatory component ΔR_{xx} of MR as a function of $1/B$ for B||[100]; the inset shows the corresponding fast Fourier transformation spectrum. (b) Oscillating part of the susceptibility $\Delta\chi = d(M)/dB$ versus $1/B$ for B along the [100] direction. The inset shows the corresponding FFT spectrum. (c) Theoretical fitting to the $\Delta\chi$ vs $1/B$ plot at representative temperature 2 K for the detection of Berry's phase.

one oscillation frequency at around 53 T [inset of Fig. 2(a)] for B||[100]. The SdH oscillations for the other directions of B also give single frequency. This implies the presence of single or two equivalent Fermi surfaces, similar to that observed in earlier SdH oscillation study [5]. However, the dHvA oscillation revealed two well-resolved frequency at 46 T and 53 T [inset of Fig. 2(b)] for the same direction

of B. This indicates two inequivalent FS cross-sections in the present material. For better understanding, we have performed magnetization measurements with $B\|[02\bar{1}]$ and $B\|[012]$. But, single frequency has been detected for both the configurations. The above study clearly demonstrates that two ellipsoidal Fermi surfaces superpose with each other along certain directions and form a complex nesting, without merging into a single contour. Later on, it has been confirmed by other group [11]. The theoretical fit to $\Delta\chi$ vs $1/B$ plot [Fig. 2(c)] with Lifshitz-Kosevich formula [10] for the superposition of two oscillating components gives the value of Berry's phase $[2\pi\beta] \sim 1.24\pi$. This value is within the range $2\pi[\frac{1}{2}\pm\frac{1}{8}]$ for 3D Dirac fermion, and far away from the value 0 for Schrodinger fermion.

Tuning the scattering mechanism in three-dimensional Dirac semimetal Cd_3As_2: From the magnetoresistivity and Hall measurements, a strong field dependence of scattering time has been observed in Cd_3As_2 and this behavior has been ascribed to the field-induced changes in the FS [6]. But, the measurement of resistivity alone is not sufficient to understand the details of the scattering mechanism. As thermoelectric power (S) is a powerful tool to probe the relaxation process in metals and semiconductors and provides complementary information to resistivity, we use S as a probe to study the effects of the FS evolution on the scattering of charge carrier in Cd_3As_2, under application of magnetic field and with carrier doping.

In Fig. 3(a), S is plotted as a function of T up to 350 K at 0, 5 and 9 T magnetic fields for Cd_3As_2. The negative sign suggests electron as majority carrier. Remarkably, S shows linear T dependence almost up to 350 K at zero and 9 T magnetic field, whereas at 5 T, it shows a weak sublinear behavior at high temperature. As shown in Fig. 3(b), S increases monotonically with field and tends to saturate

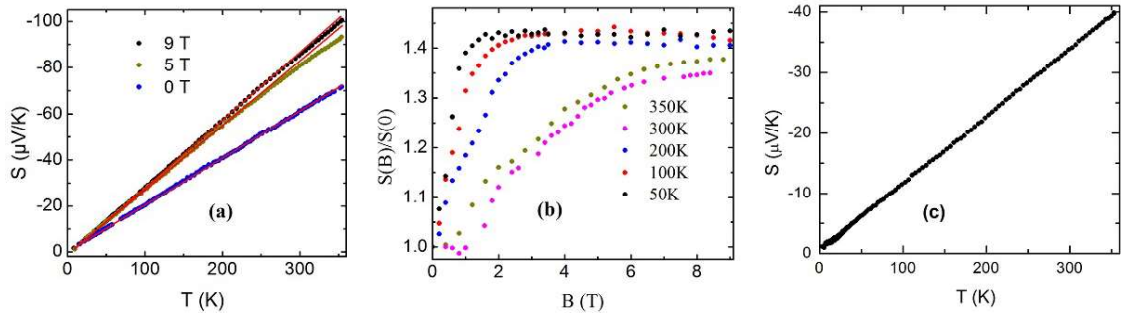

Figure 3: (a) Temperature dependence of thermoelectric power (S) up to 350 K at 0, 5 and 9 T fields for Cd_3As_2. Solid line is the guide to eye for the linear T dependence of S. (b) B dependence of the normalized S for the undoped sample. (c) T dependence of S for $(Cd_{0.98}In_{0.02})_3As_2$ up to 350 K.

at high fields. Irrespective of temperature, the $S(B)/S(0)$ emerges to a definite value with the increase in B. However, $S(B)/S(0)$ converges faster at lower temperature. According to the theory of Korenblit and Sherstobitov, the saturation value of S (S_∞) at high field in terms of the energy (ε) dependence of the electron concentration (p) at the Fermi energy (E_F) is given by [12, 13], $S_\infty = \frac{\pi^2 k_B}{3e}\frac{k_B T}{E_F}\frac{d\ln p}{d\ln \varepsilon}$. Considering $p \propto \varepsilon^s$, the expression simplifies to $S_\infty = \frac{\pi^2 k_B}{3e}\frac{k_B T}{E_F} s$. In three dimensions, s is 3/2 for a usual parabolic band and 3 for a linear band [12, 13]. Now, using the values of E_F (∼270 meV from quantum oscillation) and S_∞, we find that s is ∼ 3 for all T. Thus, $S(B)$ clearly demonstrates linear dispersion due to 3D Dirac semimetal state in Cd_3As_2. Considering linear dispersion and energy-dependent scattering time ($\tau \propto \varepsilon^m$), a simplified expression of the Mott's semiclassical formula for thermoelectric power [14], $S = \frac{\pi^2 k_B}{3e}\frac{k_B T}{E_F}(m+2)$ has been obtained. Using the slope of S vs. T plot, both at zero and at applied field, it has been found that the scattering time crosses over from being nearly energy independent (m∼0.15) to a regime of linear dependence with the increase in B. On the other hand, it is evident from $S(T)$ in Fig. 3(c) that the τ enters into the inverse energy-dependent regime with 2% In doping at Cd site.

TMR of $(Cd_{0.98}In_{0.02})_3As_2$ single crystal is measured in B||[100] and I||[012] con-

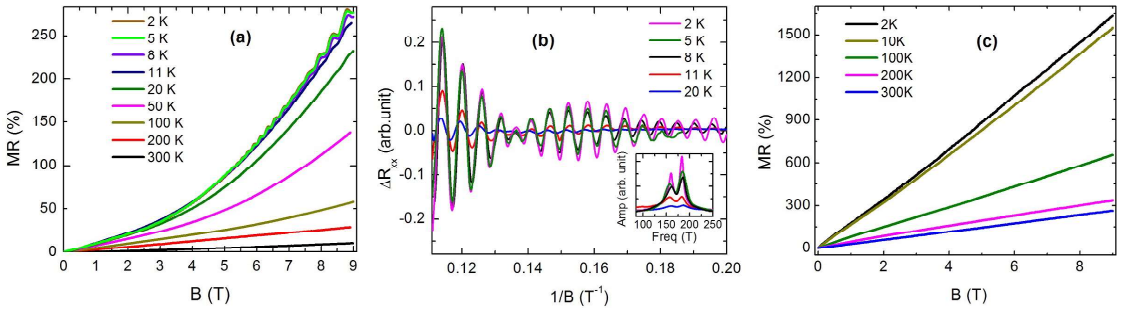

Figure 4: (a) B dependence of MR for $(Cd_{0.98}In_{0.02})_3As_2$ single crystal. (b) The oscillatory component $\triangle R_{xx}$ of MR as a function of $1/B$ in B||[100] configuration; the inset shows the corresponding FFT spectrum. (c) B dependence of MR for $(Cd_{0.96}In_{0.04})_3As_2$ single crystal.

figurations [Fig. 4(a)]. Unlike the parent compound, MR is small and non-linear in B in In-doped single crystal. At 2 K and 9 T, MR is about 280 % which suppresses to only ∼10% at 300 K. Analysing the SdH oscillation [Fig. 4(b)], two distinct frequencies (F) at 159.3 and 184.6 T have been obtained, which indicate two much larger FS cross-sections in the doped sample compared to the single smaller cross-sectional area in Cd_3As_2. This also suggests larger overlap between the two Fermi surfaces beyond Lifshitz transition in the doped sample. Fig. 4(c) shows large and nearly linear MR for $(Cd_{0.96}In_{0.04})_3As_2$ like the undoped sample. At 9 T, MR is as high as ∼ 1650% at 2 K and ∼ 250% at room temperature. But, due to large disorder, SdH oscillation has not been observed within the experimental field and temperature range. The observed behaviour of MR is consistent with the statistical model, which states that large spatial fluctuation in carrier mobility due to presence of disorder, can generate large linear MR [15].

Coexistence of topological Dirac fermions on the surface and three-dimensional Dirac cone state in the bulk of $ZrTe_5$ single crystal: Although, the long-standing debate on the anomalous resistivity peak of $ZrTe_5$ has

been explained recently by ARPES [16], the exact topological nature of the electronic band structure was remained elusive. Theoretical calculations predicted that bulk $ZrTe_5$ to be either a weak or a strong 3D TI [17]. However, the ARPES and transport measurements clearly demonstrate 3D Dirac cone state with a small mass gap between the valence band and conduction band in the bulk [16, 18]. Do theory and experiment contradict each other or the 2D Dirac cone surface state and 3D Dirac cone state in the bulk can coexist simultaneously in $ZrTe_5$? The aim of the present work is to resolve the ambiguity.

Typical size and morphology of single crystals of $ZrTe_5$ are shown in Fig. 5(a).

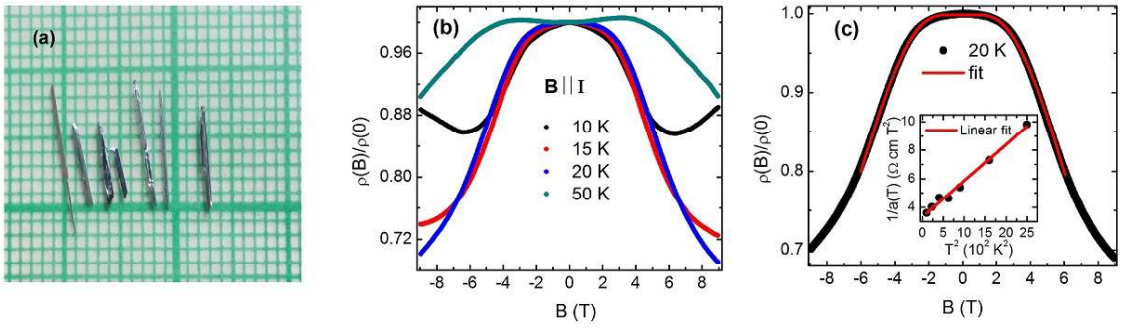

Figure 5: (a) Typical size and morphology of $ZrTe_5$ single crystal. (b) B dependence of MR at $I||B$ configuration. (c) MR (B) at 20 K, fitted with the theoretical expression, $\rho_c = \frac{1}{[\sigma_0 + a(T).B^2] + \frac{1}{\rho_0 + A.B^2}}$. Inset shows the T dependence of $1/a$.

The consequence of Adler-Bell-Jackiw (ABJ) chiral anomaly [19] in condensed matter electronic systems with 3D Dirac Fermion as quasi-particle excitation is the negative MR in $\vec{E}||\vec{B}$ configuration [20]. B dependence of this negative longitudinal MR (LMR) along with the small conventional positive MR contribution is given by, $\rho_c = \frac{1}{[\sigma_0 + a(T).B^2] + \frac{1}{\rho_0 + A.B^2}}$ [18]. The constant due to ABJ chiral anomaly, $a(T)$, exhibits inverse T^2 dependence [18]. The chiral anomaly induced negative LMR in $ZrTe_5$ has been confirmed in earlier magneto-transport study [18]. For the sake of completeness, we have also measured LMR of present $ZrTe_5$ crystal by

applying both I and B along the **a** axis. As shown in Fig. 5(b), ρ gradually decreases with increasing field until an upturn occurs at high field. A positive TMR component due to unavoidable misalignment between I and B in parallel configuration is responsible for this high field upturn. The negative LMR region is well fitted with the above mentioned theoretical expression and shown at a representative temperature 20 K in Figure 5(c). By fitting LMR at several temperatures, we have calculated the values of a. One can see from the inset of Fig. 3(c) that a^{-1} is almost linear in T^2, as predicted theoretically [18]. This B and T dependence of LMR confirms 3D Dirac fermionic excitation in the bulk state of $ZrTe_5$.

The low-energy physics of the surface state for a 3D TI can be described by

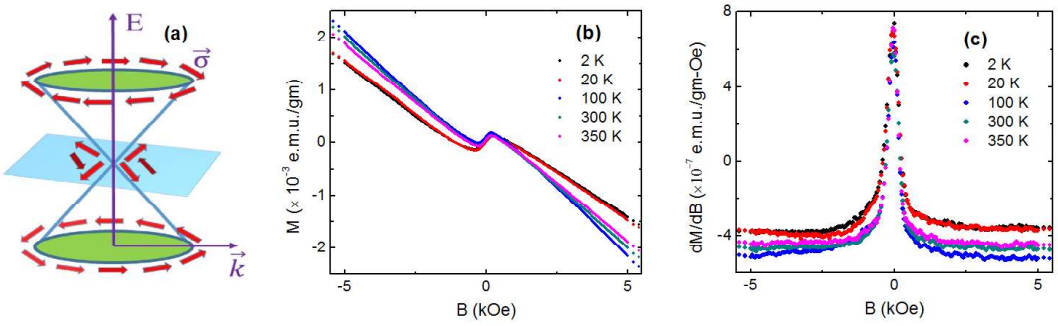

Figure 6: (a) Surface Dirac cone of 3D TI and its spin-momentum texture. (b) Magnetization as a function of B for $ZrTe_5$ single crystal. (c) $\chi = \frac{dM}{dB}$ as a function of B.

the Dirac type effective Hamiltonian, $H_{sur}(k_x,k_y) = \hbar v_F(\sigma^x k_y - \sigma^y k_x)$, where v_F is the Fermi velocity. As a consequence, the spin ($\vec{\sigma}$) is always perpendicular to its momentum ($\vec{k}$) for the eigenstate of the Hamiltonian. This leads to left-handed spin texture for the upper Dirac cone and right-handed spin texture for the lower Dirac cone [Fig. 6(a)]. Whereas at the Dirac point, the electron spin should be free to align along B due to the singularity in spin orientation [21]. This predicts a low-field paramagnetic peak in susceptibility ($\chi(B)$).

The magnetization of $ZrTe_5$ with B along the **a** axis is shown in Fig. 6(b). Over the whole range of temperature from 2 to 350 K, it shows diamagnetic signal except a paramagnetic upturn in the low-field region, unlike standard diamagnetic materials. Fig. 6(c) shows that a cusp-like paramagnetic susceptibility sharply rises above the diamagnetic floor in a narrow field range of $\sim$2 kOe around zero field. The height of the peak from the diamagnetic floor and its sharpness are insensitive to T. Similar robust and singular paramagnetic response have been reported for 3D TI candidates Bi_2Se_3, Sb_2Te_3 and Bi_2Te_3 [21]. Thus, the complete results of magnetization and magneto-transport measurements allow one to conclude that $ZrTe_5$ is a novel quantum phase of matter, which hosts both topological Dirac fermions on the surface and 3D Dirac cone state in the bulk.

Anisotropic Fermi surface probed by the de Haas-van Alphen oscillation in proposed Dirac Semimetal $TaSb_2$: $TaSb_2$ has been predicted theoretically to be a weak topological insulator [22]. Whereas, the earlier magnetotransport experiment has established it as a topological semimetal [23]. In the previous work, the Shubnikov-de Haas oscillation has been analyzed to probe the FS, with magnetic field along a particular crystallographic axis only [23]. However, the crystallographic direction dependence of magnetotransport properties and the anisotropy of the Fermi surfaces have not been probed. Due to lower crystal symmetry (monoclinic) of $TaSb_2$, the above mentioned knowledge is important from both the fundamental and application point of view.

Fig. 7(a) shows a representative piece of $TaSb_2$ single crystal with different crystal directions. To probe the anisotropy in MR and FS, we have considered three mutually perpendicular directions on the crystal [**a**-axis, **b**-axis, and perpendicular to **ab** plane, i.e., **(001)** direction] as references. The zero-field resistivity (ρ_{xx}) is

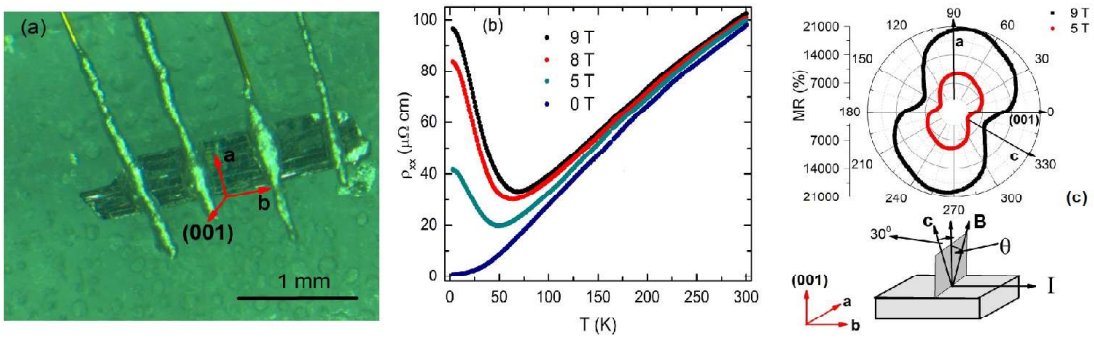

Figure 7: (a) Typical morphology and different crystallographic directions of a representative single crystal of $TaSb_2$. (b) $\rho_{xx}(T)$ both in presence and absence of B at $I\|$**b**-axis and $B\perp$**ab**-plane. (c) Angular variation of MR at 2 K when the direction of B changes from **(001)** to **a**-axis, making an angle θ.

metallic over the whole temperature range, as shown in Fig. 7 (b). With the application of B, the low-temperature resistivity is enhanced drastically. As a result, a metal to semiconductor-like crossover behavior starts to appear with decreasing T. At low T, $\rho_{xx}(T)$ shows a saturation-like behavior. Fig. 7(c) shows TMR ($B \perp I$) at 2 K with the rotation of sample about **b**-axis, making an angle θ with the field direction. At $B\|$**(001)**, the MR is $\sim 1.3\times10^4\%$ at 9 T. As the direction of B is changed from **(001)** towards **a** direction, the value of MR is observed to increase and becomes maximum ($\sim 2\times10^4\%$ at 9 T) at around $\theta = 75°$. The minimum value of MR is found to be $\sim 9500\%$ at around 165°. The two-fold rotational symmetry in MR(θ), which is expected for monoclinic crystal structure, is evident from the polar plot. The tilted pattern of MR(θ) with respect to the crystallographic axis may be due to the complex geometry of the Fermi surfaces and their relative contribution to transport [24].

The FFT spectrum of $d(M)/dB$ vs $1/B$ in Fig. 8(a) for $B\|$**a** configuration shows three distinct oscillation frequencies (F) at 156, 327 and 598 T, which im-

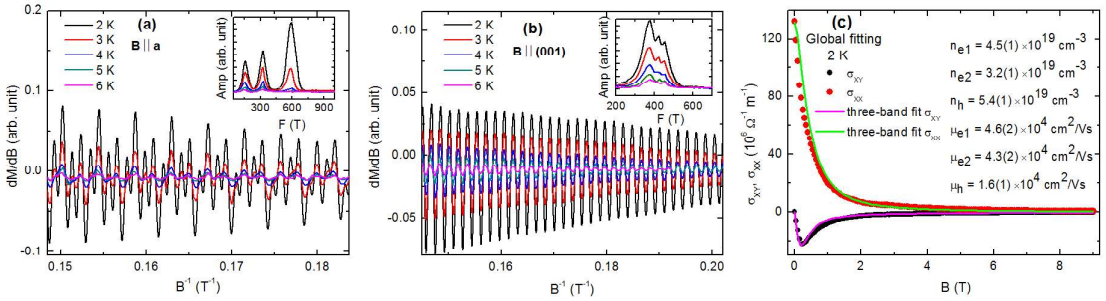

Figure 8: (a) $\Delta\chi = d(M)/dB$ versus $1/B$ at $B\|\mathbf{a}$ configuration for $TaSb_2$ crystal. Inset shows the corresponding oscillation frequency. (b) $d(M)/dB$ versus $1/B$ for $B\|\mathbf{(001)}$. The FFT spectrum has been shown in the inset. (c) Simultaneous three-band fit to the electrical conductivity (σ_{xx}) and Hall conductivity (σ_{xy}) data with the expression, $\sigma_{xx} = \sum_{i=1}^{3} \frac{en_i\mu_i}{1+\mu_i^2B^2}$ and $\sigma_{xy} = \sum_{i=1}^{3} S_i \frac{en_i\mu_i^2B}{1+\mu_i^2B^2}$, respectively, at representative temperature 2 K. The density and mobility for each types of charge carrier have been mentioned in the inset.

plies the presence of three Fermi pockets in $TaSb_2$. The dHvA oscillation for $B\|\mathbf{(001)}$ direction gives three closely spaced frequency peaks at 370, 421 and 452 T [Fig. 8(b)]. Similar magnetic measurements have also been done for $B\ \|\mathbf{b}$ and three closely spaced frequency at 462, 512 and 548 T have been found. The details analysis of oscillation amplitude by Lifshitz-Kosevich formula implies that the smallest Fermi pocket is $\sim$ 140% and the medium one is $\sim$ 30% higher in $B\ \|\mathbf{(001)}$ than the corresponding smallest and medium ones in $B\ \|\mathbf{a}$, respectively. Whereas, the largest cross-sectional area in $B\ \|\mathbf{(001)}$ configuration is 25% smaller compared to its counterpart in $B\ \|\mathbf{a}$. The values of effective mass of the charge carrier (m_{eff}) in $B\ \|\mathbf{(001)}$ for the two lighter Fermi pockets are nearly equal to that observed in $B\ \|\mathbf{a}$, and the massive one (also the largest one) is only 30% less in the previous configuration compared to later. The three-band fit to $\sigma_{xy}(B)$, as shown in Fig.8(c), reveals two high mobility ($\sim$3.48$\times$10^4 cm^2/Vs) electron-type Fermi pockets of smaller volume and one large hole-type Fermi pocket of very low mobility ($\sim$ 0.42$\times$10^4 cm^2/Vs).

TMR of orbital origin has been determined by the component of the mobility (μ) tensor in the plane perpendicular to B and it increases with increasing μ [24]. Again, μ is set by the ratio of the scattering time (τ) to m_{eff}, $\mu \sim \frac{\tau}{m_{eff}}$. Cross-sectional area ($A_F$) of Fermi pockets for $B \parallel$**(001)** and $B \parallel$**a** implies smaller phase space for the scattering of charge carrier from the two electron-type Fermi pockets in the plane perpendicular to **a**-axis, and as a result, the value of τ is larger [24]. Whereas, the m_{eff} for the two pockets remains almost equal for the two directions. As a consequence, the mobility of the charge carriers in the plane perpendicular to **a** appears to be higher for these channels of charge conduction. On the other hand, A_F and m_{eff} of largest hole-type Fermi pocket have been found to be 25% and 30% smaller, respectively, for $B \parallel$**(001)** compared to the $B \parallel$**a** configuration. So, it appears that the larger Fermi pocket has higher mobility for $B \parallel$**(001)**, unlike to that observed in two smaller Fermi pockets. However, μ of hole-type carriers from the largest Fermi pocket is itself very small; close to one-third of the values for electron-type charge carriers from the smaller Fermi pockets. Thus, the transport properties in $TaSb_2$ will be dominated by the two electron pockets of small and intermediate volume. As a consequence, the value of magnetoresistance is expected to enhance with the rotation of field from **(001)** to **a** direction.

References

[1] M. Z. Hasan and C. L. Kane, Rev. Mod. Phys. **82**, 3045âĂŞ3067 (2010).

[2] Z. J. Wang *et al.*, Phys. Rev. B **85**, 195320 (2012).

[3] Z. K. Liu *et al.*, Nat. Mater. **13**, 677 (2014).

[4] S. Y. Xu *et al.*, Science **349**, 6248 (2015).

[5] L. P. He *et al.*, Phys. Rev. Lett. **113**, 246402 (2014).

[6] T. Liang *et al.*, Nat. Mater. **14**, 280 (2015)

[7] J. Xiong *et al.*, Science **350**, 413 (2015).

[8] J. Feng *et al.*, Phys. Rev. B **92**, 081306 (2015).

[9] M. Neupane *et al.*, Nat. Commun. **5**, 3786 (2014).

[10] D. Shoenberg, *Magnetic Oscillations in Metals* (Cambridge Univ. Press, Cambridge, England, 1984).

[11] Y. Zhao *et al.*, Phys. Rev. X **5**, 031037 (2015).

[12] L. L. Korenblit and V. E. Sherstobitov, Sov. Phys. Semicond. **2**, 573 (1968).

[13] D. Armitage and H. J. Goldsmid, J . Phys. C **2**, 2389 (1969).

[14] E. H. Hwang *et al.*, Phys. Rev. B **80**, 235415 (2009).

[15] M. M. Parish *et al.*, Nature (London) **426**, 162 (2003).

[16] G. Manzoni *et al.*, Phys. Rev. Lett. **115**, 207402 (2015).

[17] H. Weng *et al.*, Phys. Rev. X **4**, 011002 (2014).

[18] Q. Li *et al.*, Nat. Phys. **12**, 550-554 (2016).

[19] J. S. Bell and R. A. Jackiw, Il Nuovo Cimento A **60**, 47-61 (1969).

[20] H. B. Nielsen and M. Ninomiya, Phys. Lett. B **130**, 389-396 (1983).

[21] L. Zhao *et al.*, Nat. Mater. **13**, 580 (2014).

[22] C. Xu *et al.*, Phys. Rev. B **93**, 195106 (2016).

[23] Y. Li *et al.*, Phys. Rev. B **94**, 121115(R) (2016).

[24] A. Collaudin *et al.*, Phys. Rev. X **5**, 021022 (2015).

List of Figures

1 (a) X-ray diffraction pattern of powdered sample of Cd_3As_2 single crystal. (b) Resistivity (ρ_{xx}) as a function of temperature. (c) Magnetic field (B) dependence of the transverse magnetoresistance (TMR) when B||[100] and I||[012] direction. iii

2 (a) The oscillatory component ΔR_{xx} of MR as a function of $1/B$ for B||[100]; the inset shows the corresponding fast Fourier transformation spectrum. (b) Oscillating part of the susceptibility $\Delta\chi = d(M)/dB$ versus $1/B$ for B along the [100] direction. The inset shows the corresponding FFT spectrum. (c) Theoretical fitting to the $\Delta\chi$ vs $1/B$ plot at representative temperature 2 K for the detection of Berry's phase. iii

3 (a) Temperature dependence of thermoelectric power (S) up to 350 K at 0, 5 and 9 T fields for Cd_3As_2. Solid line is the guide to eye for the linear T dependence of S. (b) B dependence of the normalized S for the undoped sample. (c) T dependence of S for $(Cd_{0.98}In_{0.02})_3As_2$ up to 350 K. v

4 (a) B dependence of MR for $(Cd_{0.98}In_{0.02})_3As_2$ single crystal. (b) The oscillatory component $\triangle R_{xx}$ of MR as a function of $1/B$ in B||[100] configuration; the inset shows the corresponding FFT spectrum. (c) B dependence of MR for $(Cd_{0.96}In_{0.04})_3As_2$ single crystal. vi

5 (a) Typical size and morphology of $ZrTe_5$ single crystal. (b) B dependence of MR at $I||B$ configuration. (c) MR (B) at 20 K, fitted with the theoretical expression, $\rho_c = \frac{1}{[\sigma_0 + a(T).B^2] + \frac{1}{\rho_0 + A.B^2}}$. Inset shows the T dependence of $1/a$. vii

6 (a) Surface Dirac cone of 3D TI and its spin-momentum texture. (b) Magnetization as a function of B for $ZrTe_5$ single crystal. (c) $\chi=\frac{dM}{dB}$ as a function of B. viii

7 (a) Typical morphology and different crystallographic directions of a representative single crystal of $TaSb_2$. (b) $\rho_{xx}(T)$ both in presence and absence of B at $I\|\mathbf{b}$-axis and $B\perp\mathbf{ab}$-plane. (c) Angular variation of MR at 2 K when the direction of B changes from **(001)** to **a**-axis, making an angle θ. x

8 (a) $\Delta\chi= d(M)/dB$ versus $1/B$ at $B\|\mathbf{a}$ configuration for $TaSb_2$ crystal. Inset shows the corresponding oscillation frequency. (b) $d(M)/dB$ versus $1/B$ for $B\|$**(001)**. The FFT spectrum has been shown in the inset. (c) Simultaneous three-band fit to the electrical conductivity (σ_{xx}) and Hall conductivity (σ_{xy}) data with the expression, $\sigma_{xx}=\sum_{i=1}^{3}\frac{en_i\mu_i}{1+\mu_i^2B^2}$ and $\sigma_{xy}=\sum_{i=1}^{3}S_i\frac{en_i\mu_i^2B}{1+\mu_i^2B^2}$, respectively, at representative temperature 2 K. The density and mobility for each types of charge carrier have been mentioned in the inset. xi

1.1 A schematic diagram to show the discrete energy levels of an isolated atom and energy band of crystalline solid. Reproduced from Ref. [1]. 2

1.2 Electronic phases of matter classified by band theory. 3

1.3 (a) Schematic of two-dimensional electron gas under out-of-plane external magnetic field. (b) Formation of Landau levels under application of magnetic field, and the variation in the electronic density of states across the Fermi level with the increasing field. (c) Hall measurement configuration. V_H is the Hall voltage. 5

1.4 Geometrical objects with different topology. The objects are classified by the value of Genus, which is basically the number of holes in the object. 7
1.5 (a) The interface between a quantum Hall ground state and an trivial insulator/vacuum. (b) The electronic band structure, where a single edge state connects the bulk valence band to the bulk conduction band. Reproduced from Ref. [2]. 9
1.6 Schematic picture of the QSH system as a superposition of two QH systems. Reproduced from Ref. [8]. 10
1.7 (a) The edge states cross the Fermi level an even (zero) number of times. (b) The edge states cross the Fermi level once. (c) The edge states cross the Fermi level an odd number of times. Reproduced from Ref. [2]. 13
1.8 (a) The interface between a QSH insulator and an ordinary insulator.(b) The edge state dispersion. (c) High-symmetry points in 2D bulk Brillouin zone. Figure (a) and (b) are reproduced from Ref. [2]. 14
1.9 (a) Weak three-dimensional topological insulators. (b) High-symmetry points in 3D bulk Brillouin zone. 17
1.10 (a) High-symmetry points in 3D bulk Brillouin zone. (b) Constant energy contour at the Fermi level. (c) 2D Dirac cone surface state and spin-momentum locking. 18

1.11 (a)-(d) Energy and momentum dependence of the local density of states for the Bi_2Se_3 family of materials on the [111] surface. A warmer color represents a higher local density of states. Red regions indicate bulk energy bands and blue regions indicate a bulk energy gap. The surface states can be clearly seen around the Γ point as red lines dispersing inside the bulk gap. Reproduced from Ref. [18]. 20

1.12 Left: Honeycomb lattice of graphene. **A** and **B** are the two types of lattice, identified for band structure calculations, using tight-binding model. Right: Energy bands of graphene obtained from the tight-binding model and zoom around the Dirac point at K. Reproduced from Ref. [23]. 22

1.13 Schematic band inversion between two bands: The trivial band gap in (a) closes at a critical point in (b), and reopens inverted in (c) with the two states swapping their orbital characters at the symmetry point. 23

1.14 Topological phase transition in $BiTl(S_{1-\delta}Se_{\delta})_2$. (A) High-resolution ARPES dispersion maps from a spin-orbit band insulator (left panel) to a topological insulator (right panel). Topological quantum numbers (TQN) are denoted by topological invariant ν_0. (B) ARPES-mapped native Fermi surfaces and their spin-texture for different chemical compositions (from left to right, $\delta = 0.0$ to $\delta = 1.0$). (C) Left and right panels: Energy distribution curves for stoichiometric compositions $\delta = 0.0$ and $\delta = 1.0$, respectively. Center panels: ARPES spectra indicating band gap and Dirac node for compositions $\delta = 0.2$ to $\delta = 0.8$. Figures are adopted from Ref. [25]. 24

1.15 (a) C_4 rotational symmetry protected unavoidable band crossing in Cd_3As_2, as a representative. Here, k_3 is the third momentum direction, i.e., k_3 direction. (b) Schematic of the spin-polarized surface states in a 3D TI. (c) Schematic of a TDS with spin-polarized Fermi arcs on its surface connecting projections of two bulk Dirac nodes. The red and blue balls, surrounded by a black boundary indicates that one Dirac node is the degeneracy of two Weyl nodes, which will be discussed in the following section. Figure (b) and (c) are reproduced from Ref. [29]. 26

1.16 Weyl nodes of opposite chirality. The arrows indicate the direction of the spin vector, which can be parallel or antiparallel to the momentum vector. 27

1.17 (a) A four-component 3D Dirac node in a TDS as a superposition of two two-component Weyl nodes, and the splitting of Dirac cone into two Weyl cones of opposite chirality under broken time-reversal symmetry. (b) Schematic of a WSM with spin-polarized Fermi arcs on its surfaces connecting the projections of two Weyl nodes with opposite chirality. The red and blue colors of the bulk Weyl cones and the corresponding projection points on the surfaces represent opposite chirality of the Weyl nodes. The red arrows on the surfaces indicate the spin texture of the Fermi arcs. Figure (b) is reproduced from Ref. [29]. 28

1.18 Stacking plot of constant-energy contours at different binding energies shows Dirac cone band structure. (a) White dashed lines are the guide to the eye that trace the linear dispersions in Na_3Bi. Figure reproduced from Ref. [36]. (b) Red dotted lines are guide to the eye that indicate the linear dispersions and intersect at the Dirac point in Cd_3As_2. Figure reproduced from Ref. [37] 30

2.1 Schematic of experimental set-up for chemical vapor transport. . . . 35

2.2 Schematic diagram of x-ray diffraction by crystallographic planes. . 38

2.3 (a) Simplified diagram of a transmission electron microscope. (b)A schematic diagram showing different types scattered and transmitted electrons, and emitted x-ray, which are produced by the interaction of electron beam and sample. 40

2.4 Schematic diagram of thermal and electrical connections to the sample with heater and sensors. T_{hot} and T_{cold} are the temperatures of two Cernox chip thermometers, V+ and V- are the two voltage leads, I+ and I- are the current leads and Q representing the heater terminal. Reproduced from Ref.[48]. 43

2.5 A simplified schematic diagram of SQUID VSM detection system. Figure reproduced from Ref.[49]. 45

3.1 (a) Image of a representative piece of Cd_3As_2 single crystal with electrical contacts. (b) X-ray diffraction pattern of powdered single crystals of Cd_3As_2. Black, experimental data; red, the calculated pattern; blue, the difference between experimental and calculated intensities; green, the Bragg positions. 50

3.2 (a) Temperature dependence of the resistivity of Cd_3As_2 crystal. (b) Magnetic field dependence of magnetoresistance (MR) at various temperatures when the field was applied along the [100] direction. The inset shows the temperature dependence of MR at a field of 9 T. 51

3.3 (a) The oscillatory component ΔR_{xx} of MR (after subtracting a smooth background) as a function of $1/B$ at various temperatures with magnetic field along the $[02\bar{1}]$ direction; the inset shows the oscillation frequency after fast Fourier transform. (b) ΔR_{xx} for magnetic field along the [100] direction; the inset shows the corresponding frequency. 52

3.4 (a) Magnetic field (along the [100] direction) dependence of the diamagnetic moment at temperature of 2 and 20 K. (b) Oscillating part of the susceptibility $\Delta\chi = d(M)/dB$ versus $1/B$; de Haas-van Alphen (dHvA) effect. The inset shows the oscillation frequency after the fast Fourier transform is found from the dHvA effect. . . . 53

3.5 (a) Oscillating part of susceptibility $\Delta\chi = d(M)/dB$ vs $1/B$ (dHvA effect) for magnetic field along the $[02\bar{1}]$ direction; the inset shows oscillation frequency at 55.20 T after the fast Fourier transformation. (b) Oscillating part of magnetization $\triangle m$ vs $1/B$ (dHvA effect) for magnetic field along the [012] direction; the inset shows the frequency of oscillation after fast Fourier transform found from dHvA effect. (c) Schematic diagram of the possible nested Fermi surface above the Lifshitz transition, and the Fermi surface cross-sections along different crystallographic directions. 55

3.6 (a) Temperature dependence of the relative amplitude of quantum oscillation for the ninth Landau level, where *Ra* and *Rb* are the oscillation amplitudes in the SdH oscillation for $B\|[02\bar{1}]$ and $B\|[100]$, respectively, and m corresponds to the oscillation amplitudes in $\Delta\chi$ for $B\|[100]$. The solid line is a fit to the thermal damping term (R_T) of Lifshitz-Kosevich formula [Equation 3.1]. (b) Landau index n plotted against $1/B$ (Solid circles denote the peak positions) from the SdH oscillations. Solid lines are the linear fit to the experimental data points. From the linear extrapolation of the fitted lines, as shown in the inset, the obtained values of **x**-axis intercept are ~ 0.20 and ~ 0.32 for $B \parallel [100]$ and $B \parallel [02\bar{1}]$, respectively. (c) Theoretical fitting to the $\Delta\chi(1/B)$ for $B\|[100]$ by the two-band LK formula, at representative temperature 2 K. 56

4.1 (a) X-ray diffraction pattern of powdered single crystals of $(Cd_{0.98}In_{0.02})_3As_2$. Black ($Y_{obs}$), experimental data; red (Y_{cal}), the calculated pattern; blue (Y_{obs}-Y_{cal}), the difference between experimental and calculated intensities; green, the Bragg positions. (b) X-ray diffraction pattern of powdered single crystals of $(Cd_{0.96}In_{0.04})_3As_2$. (c) Selective area electron diffraction (SAD) pattern obtained through HRTEM measurement for $(Cd_{0.98}In_{0.02})_3As_2$. 62

4.2 (a) A representative image of electrical and thermal contacts on a piece of Cd_3As_2 single crystal. 1, 2, 3, and 4 are the terminals for electrical resistivity and thermopower measurements. 5 and 6 are the voltage terminals in Hall resistivity measurements. (b) Temperature dependence of resistivity (ρ_{xx}) of Cd_3As_2 single crystal from 2 to 350 K. (c) The field dependence of the Hall resistance at 2 K. . 64

4.3 (a) Temperature dependence of the Seebeck coefficient (S) of Cd_3As_2 single crystal up to 350 K at 0, 5 and 9 T fields. Solid line shows the linear T dependence of S. (b) Magnetic field dependence of the normalized thermoelectric power at different temperatures between 50 and 350 K up to 9 T, where $S(0)$ is the zero-field Seebeck coefficient at the respective temperatures. 65

4.4 (a) Field dependence of the Hall resistance (R_{xy}) at some representative temperatures and (b) temperature dependence of resistivity (ρ_{xx}) for different applied fields for $(Cd_{0.98}In_{0.02})_3As_2$ single crystal. (c) $\ln(\rho_{xx})$ versus $1000T^{-1}$ plot for $(Cd_{0.98}In_{0.02})_3As_2$ crystal. Using the slope in linear region, the thermal activation energy gap induced by the magnetic field has been calculated. Inset shows the field variation of the energy gap above 7 T. 71

4.5 (a) Magnetoresistance of $(Cd_{0.98}In_{0.02})_3As_2$ single crystal at some selected temperatures between 2 to 300 K. (b) The first-order derivative of MR [d(MR)/dB] at 50 K. The black and green solid lines represents linear MR and quadratic MR region respectively. (c) d(MR)/dB at some representative temperatures above 50 K. 72

4.6 (a) The oscillatory component $\triangle R_{xx}$ of MR as a function of $1/B$ at various temperatures with magnetic field along the [100] direction; the inset shows the oscillation frequency after fast Fourier transform in $(Cd_{0.98}In_{0.02})_3As_2$. (b) Thermal damping of oscillation amplitude in $(Cd_{0.98}In_{0.02})_3As_2$ crystal. Solid points are the experimental data and the red line is the fit to the experimental data. (c) The oscillatory component $\triangle R_{xx}$ of MR at 2 K (after subtracting a smooth background). Black, experimental curve; green, fit with β=0; red, fit with non-zero value of β. 73

4.7 (a) Temperature dependence of the thermoelectric power (S) of $(Cd_{0.98}In_{0.02})_3As_2$ up to 350 K. (b) High resolution transmission electron microscopy (HRTEM) image of the crystal. 75

4.8 (a) Resistivity (ρ_{xx}) as a function of temperature for $(Cd_{0.96}In_{0.04})_3As_2$. (b) Field dependence of the Hall resistance (R_{xy}) at 2 and 300 K. . 78

4.9 (a) Magnetoresistance of $(Cd_{0.96}In_{0.04})_3As_2$ at a few representative temperatures from 2 to 300 K. (b) Temperature dependence of the thermoelectric power (S) of $(Cd_{0.96}In_{0.04})_3As_2$ up to 300 K. 78

5.1 (a) Typical size and morphology of few representative single crystals of $ZrTe_5$. (b) X-ray diffraction pattern of powdered single crystals of $ZrTe_5$. Black open circle, experimental data; red, the calculated pattern; blue, the difference between experimental and calculated intensities; green, the Bragg positions. (c) Atomic structure of $ZrTe_5$. Reproduced from Ref. [40]. 84

5.2 (a) Different crystallographic directions and electrical contacts in a representative piece of $ZrTe_5$ single crystals. (b) Temperature dependence of resistivity (ρ) both in presence and absence of external magnetic field. 86

5.3 (a) Hall resistivity (ρ_{xy}) of $ZrTe_5$ single crystal at several representative temperatures over the range 2-300 K. (b) Transverse magnetoresistance ($I \perp \vec{B}$) normalized to the zero field value upto 9 T. . . 87

5.4 (a) Magnetoresistance measured at temperatures from 10 to 50 K, when applied current and magnetic field are parallel to each other, (b) Magnetoresistance at 20 K, fitted with the theoretical expression, $\rho_c = \frac{1}{[\sigma_0 + a(T).B^2] + \frac{1}{\rho_0 + A.B^2}}$, and (c) Temperature dependence of $1/a$, where a is in the units of S cm^{-1} T^{-2}. 89

5.5 (a) Longitudinal magnetoresistance measured at temperatures 5 K, 25 K, 30 K and 40 K, when applied current and magnetic field are parallel to each other. (b), (c), (d), (e) and (f) are the fit to the experimental data with the theoretical expression, $\rho_c = \frac{1}{[\sigma_0 + a(T).B^2] + \frac{1}{\rho_0 + A.B^2}}$, at several representative temperatures. 90

5.6 (a) Magnetization of $ZrTe_5$ single crystal, measured at several representative temperatures from 2 to 350 K. (b) Differential susceptibility ($\chi = \frac{dM}{dB}$) obtained after taking derivative of the magnetization with respect to external magnetic field. Inset shows the linear B dependence of χ, as B tending towards zero on both side of the zero field cusp at representative temperature 350 K. 93

5.7 (Color online) (a) Magnetization of $ZrTe_5$ single crystal, which was kept for three weeks in desiccator from the first measurements [Figure 5.6]. (b) Differential susceptibility ($\chi=\frac{dM}{dB}$) obtained after taking derivative of the magnetization with respect to external magnetic field. Inset shows the linear B dependence of χ as B tending towards zero on both sides of the zero field cusp at representative temperature 350 K. 94

5.8 A schematic diagram, representing the minimum nontrivial topological nature of the electronic band structure of $ZrTe_5$ single crystal. $ZrTe_5$ monolayers, which lie in the **ac**-plane, stack together along the **b**-axis by weak van der Waals attraction. Independent conducting edge state of monolayers, as shown by the blue arrows in the figure, forms a topological surface state in bulk sample, known as weak three-dimensional topological insulating state. 96

6.1 (a) High resolution TEM image, taken on a representative piece of $TaSb_2$ single crystal. Inset shows the Fourier-filtered image of the red dotted region. (b) and (c) are the selected area electron diffraction (SAD) patterns taken along [100] and [110] zone axis, respectively. (d) The energy-dispersive X-ray (EDX) spectroscopy data. 102

6.2 (a) X-ray diffraction pattern of powdered single crystals of $TaSb_2$. Black open circles are experimental data (Y_{obs}), red line is the calculated pattern (Y_{cal}), blue line is the difference between experimental and calculated intensities (Y_{obs}-Y_{cal}), and green lines show the Bragg positions. (b) Schematic diagram for the crystal structure of $TaSb_2$. 103

6.3 (a) Typical morphology and different crystallographic directions of a representative single crystal of $TaSb_2$, and (b) Temperature dependence of resistivity (ρ_{xx}) both in presence and absence of external magnetic field. Current (I) is applied along **b**-axis and magnetic field (B) is perpendicular to the **ab** plane. Inset shows the first order derivative of ρ_{xx} with respect to T. Metal- to semiconductor-like crossover temperature is named as T_m, and T_i is the temperature for the inflection point of $\rho_{xx}(T)$. 105

6.4 (a) Anisotropic magnetoresistance of a representative $TaSb_2$ single crystal at 2 K when the sample is rotated form $B \parallel(001)$ to $B \parallel$**a**-axis configuration, making an angle θ between B and (001) direction. (b) Magnetoresistance of the same piece of single crystal at 2 K when the angle (90° - ϕ) between I and B has been changed at two representative field strengths 5 and 9 T. 106

6.5 Magnetoresistance as a function of magnetic field at some representative temperatures for (a) $B \parallel I \parallel$**b** configuration, (b) $B\parallel(001)$ and $I\parallel$**b** configuration, and (c) for $B\parallel$**a** and $I\parallel$**b** configuration. 108

6.6 (a) The field dependence of Hall resistivity (ρ_{yx}) and its evolution with temperature. The Hall measurement has been performed in $B\|(001)$ and $I\|\mathbf{b}$ configuration. Inset shows the schematic of the Hall measurement setup. (b), (c), (d), and (e) show the simultaneous (i.e., global) three-band analysis of electrical conductivity (σ_{xx}) and Hall conductivity (σ_{xy}) data at 2 K, 50 K, 100 K, and 200 K, respectively. The black dots represent the field dependence of Hall conductivity (σ_{xy}) and the red dots represent the field dependence of electrical conductivity (σ_{xx}). The green and magenta curves are the three-band fit to the experimental data with the expression, $\sigma_{xx}=\sum_{i=1}^{3}\frac{en_i\mu_i}{1+\mu_i^2B^2}$ and $\sigma_{xy}=\sum_{i=1}^{3}S_i\frac{en_i\mu_i^2B}{1+\mu_i^2B^2}$, respectively. The density and mobility for each types of charge carrier have been mentioned in the inset. 109

6.7 Field dependence of magnetization (M) for (a) $B\ \|\mathbf{a}$, (b) $B\ \|(001)$, and (c) $B\ \|\mathbf{b}$ configurations. 111

6.8 (a) Oscillating part of dc susceptibility ($\Delta\chi$), which has been obtained by taking the first order derivative of magnetization (M), as a function of $1/B$ for $B\|\mathbf{a}$-axis configuration. (b) The oscillation frequencies after the fast Fourier transformation (FFT). Oscillations in the field range 4 to 7 T has been used for FFT. (c) Thermal damping of the normalized FFT peak intensity. The solid line is a fit to the Lifshitz-Kosevich formula [equation (1)]. 114

6.9 a) $\Delta\chi$ versus $1/B$ for $B\|(001)$ configuration. (b) The oscillation frequencies after the fast Fourier transformation. Oscillations in the field range 4 to 7 T has been used for FFT. (c) Theoretical fitting of the frequency distribution plot for $B\|(001)$ configuration has been shown at different temperatures. The solid circles are the experimental data and the continuous lines are the theoretical fit with the expression, y=$\frac{a}{1+b(x-f_1)^2}+\frac{c}{1+d(x-f_2)^2}+\frac{e}{1+f(x-f_3)^2}$. (d) Temperature dependence of the normalized FFT peak intensity. The solid line is a fit to the Lifshitz-Kosevich formula [equation (1)]. 115

6.10 (a) $\Delta\chi$ versus $1/B$ for $B\|$**b**-axis configuration. (b) The oscillation frequencies after the fast Fourier transformation. Oscillations in the field range 4 to 7 T has been used for FFT. A specimen of the theoretical fitting to the frequency distribution plots has been shown in the inset at 2 K. (c) Thermal damping of the normalized FFT peak intensity. The solid line is a fit to the Lifshitz-Kosevich formula [equation (1)]. 117

8.1 (a) Magnetization measured in SQUID-VSM (Quantum Design) at several representative temperatures for standard diamagnetic bismuth sample. (b) Differential susceptibility ($\chi=\frac{dM}{dB}$) obtained after taking numerical derivative of the magnetization with respect to external magnetic field. 130

8.2 (a) Magnetization of standard paramagnetic palladium sample at 2 and 300 K, (b) $\frac{dM}{dB}$, and (c) Magnetization of single crystal of 3D Dirac semimetal Cd_3As_2. Solid line implies linear fit to the experimental data. 131

8.3 (a) Magnetization (M) vs B of freshly cleaved single crystal of $Bi_{1.5}Sb_{0.5}Te_{1.7}Se_{1.3}$ at temperatures 5 K and 280 K, (b) Susceptibility ($\chi = \frac{dM}{dB}$). 131

List of Tables

4.1 The values of Seebeck coefficient at 300 K (S_{300K}), resistivity at 2 K (ρ_{2K}), carrier density (n), carrier mobility (μ) and magnetoresistance at 2 K and 9 T for Cd_3As_2, 2% indium-doped [$Cd_3As_2(02)$] and 4% indium-doped [$Cd_3As_2(04)$] samples. 79

6.1 Parameters associated to the Fermi surface of $TaSb_2$, when the field is applied along the **a**-axis. A_F is the Fermi surface cross-section. m_{eff} is the effective mass of the charge carrier and v_F is the Fermi velocity. 114

6.2 Parameters associated to the Fermi surface of $TaSb_2$, when the field is applied perpendicular to ab plane i.e., along the (001) direction. . 114

6.3 Parameters associated to the Fermi surface of $TaSb_2$, when the field is applied along the **b**-axis direction. 118

1

Introduction

In this chapter, we review the theoretical foundation and experimental discovery of different topological electronic states of material. As phonon plays no role in determining the topological nature of these electronic states, all the physical phenomena associated to electronic band topology can be explained without incorporating temperature as a parameter, i.e., without considering the Boltzmann statistics. At first, we briefly discuss the conventional electronic states, which have been realized in band theory of solid. Next, the simplest non-trivial insulating phase (known as Integer Quantum Hall State), and the topological order in condensed matter electronic system are introduced. Depending on the presence of symmetries in an electronic system and its dimensionality, the non-trivial insulating states can have different topological structure. In the following section, we present Quantum Spin Hall (QSH) State in two dimensions (2D) and another type of topological classification in solid state electronic systems. We review the theoretical and experimental developments from 2D QSH state to 3D topological insulators (TI). Finally, a brief description on recently discovered 3D Dirac and

Weyl semimetals is given, which are characterized as topological semimetals. We discuss the earlier experimental advancements, and elaborate how these previous works inspire us to look for different electronic properties and its possible microscopic origin, to verify the non-trivial nature of electronic band structure, and to discover new electronic phases allowed by topological fine structure.

1.1 Band theory and conventional electronic phases

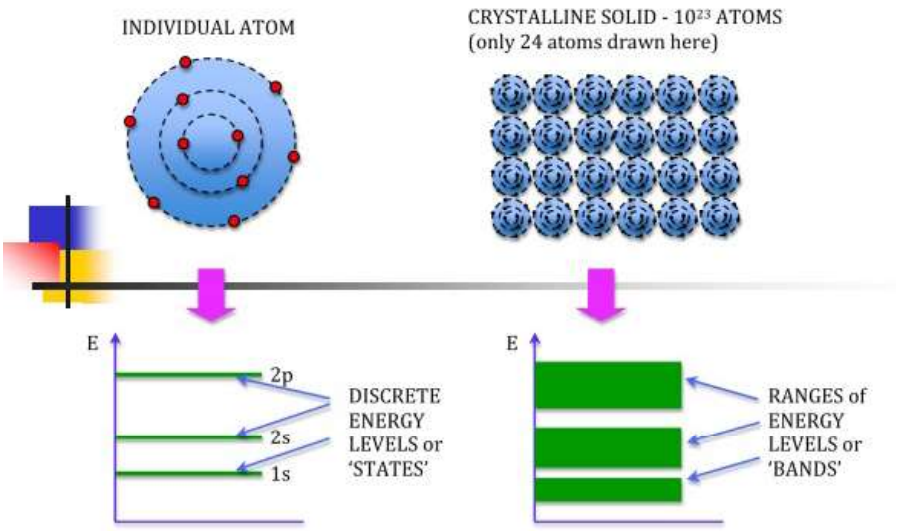

Figure 1.1: A schematic diagram to show the discrete energy levels of an isolated atom and energy band of crystalline solid. Reproduced from Ref. [1].

In the case of a single isolated atom, there are various discrete energy levels, known as atomic orbitals. When two atoms join together to form a molecule, their atomic orbitals overlap, and each atomic orbital splits into two molecular orbitals of different energy. In a solid, a large number of atoms are arranged systematically in space lattice and each atom is influenced by neighbouring atoms. As a consequence, each atomic orbital splits into large number of discrete molecular

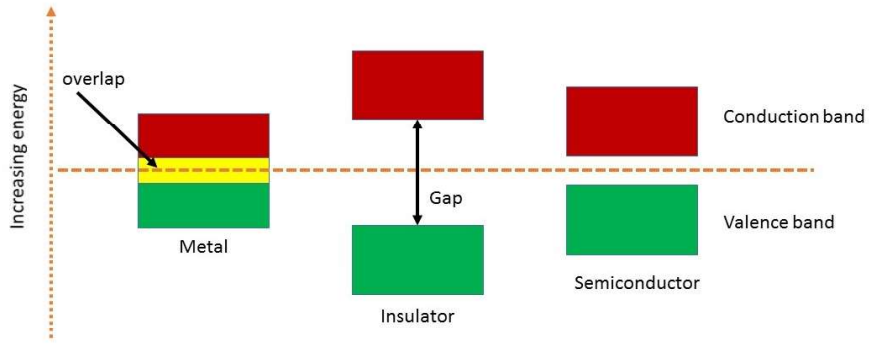

Figure 1.2: Electronic phases of matter classified by band theory.

orbitals, each with a different energy. The energy of adjacent levels is so close that they can be considered as a continuum, forming an energy band. Figure 1.1 is a schematic diagram, representing the above discussion. The highest completely occupied band is called the valence band and the partially filled or completely empty band is known as conduction band. For the conduction of electrical energy in a material, there must be partially filled band. In case of a metal, as shown in Figure 1.2, the valence and conduction band overlap with each other in such a way that the conduction band is partially filled and participates in charge conduction. A semimetal, where the valence and conduction band just touch at a point without introducing any well-defined Fermi surface, is also a conductor of charge. For an insulator, due to gap between valence and conduction band, the conduction band is completely empty and there is no charge conduction under external electric field. In the materials where the gap is small ($\lesssim 1$ eV), electrons thermally excited from valence to conduction band near room temperature, and participate in charge conduction. These materials are known as semiconductors. It can be shown that via smooth deformation of the Hamiltonian, an insulating gap can be tuned to an arbitrarily small value or to an exceptionally large value, without closing the gap. In mathematical language, all the conventional insulating states are related

via an equivalence relation. In that sense, vacuum, which, according to the Dirac equation, has a band gap that corresponds to the pair production ($\sim 10^6$ eV), is also a trivial insulator. Thus, the band theory of solid is extremely successful in grouping a wide variety of materials into just two categories: metals and insulators. It has been thought to be most powerful quantum mechanical tool available to understand the electronic properties of crystalline solids, until the discovery of Integer Quantum Hall Effect (IQHE).

1.2 The Integer Quantum Hall State and introduction of topology in electronic systems

1.2.1 Experimental discovery and the strange observation

The experimental discovery of Integer Quantum Hall Effect in 1980 by von Klitzing, led to think a different classification paradigm, beyond conventional band theory of solid [2, 3]. IQHE is the simplest example of insulator which is fundamentally not equivalent to vacuum. Two-dimensional electron gas under application of out-of-plane external magnetic field forms cyclotron orbits well-inside the boundary [Figure 1.3(a)]. The single particle Hamiltonian (H) describing the motion of electron is given by the expression,

$$H = \frac{(\mathbf{p} - e\mathbf{A})^2}{2m}, \tag{1.1}$$

where p, m, and $\mathbf{A}$ are momentum of electron, effective mass, and magnetic vector potential, respectively. In this situation, each electronic energy band of parent state splits into several sub-bands, known as Landau levels. The energy of nth Lan-

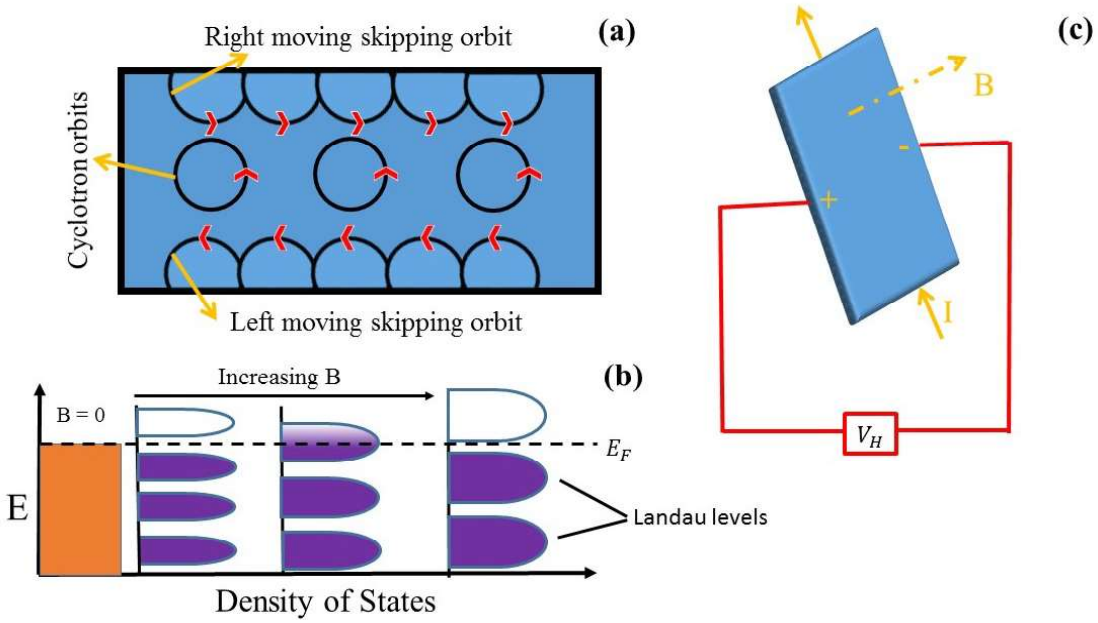

Figure 1.3: (a) Schematic of two-dimensional electron gas under out-of-plane external magnetic field. (b) Formation of Landau levels under application of magnetic field, and the variation in the electronic density of states across the Fermi level with the increasing field. (c) Hall measurement configuration. V_H is the Hall voltage.

dau level is $E_n = \hbar\omega_c(n + \frac{1}{2})$, where $\omega_c = eB/m_c^\star$ and $m_c^\star$ is the effective cyclotron mass of the charge carrier. When N Landau levels are filled, there is an energy gap between N^{th} filled band and $(N+1)^{th}$ empty band, which causes the bulk to behave as an insulator. Being a function of external magnetic field, the degeneracy of Landau levels increases with increasing field strength. As a consequence, the Landau levels pass through the Fermi level of the system, which results in oscillations of the electronic density of states at the Fermi level. This phenomenon produces oscillations in several electronic properties of a material including electrical resistance (Shubnikov-de Haas effect) and magnetization (de Haas-van Alphen effect), which is familiar as quantum oscillations. The frequency of this oscillation in a material is proportional to the cross-sectional area of the Fermi surface, perpendicular to the direction of magnetic field. By applying magnetic field along different

directions of a crystals, one can measure the cross sections of the Fermi surface. This technique has been established as a powerful tool to probe the Fermi surface of a material.

However, the electrons at the edge of the two-dimensional electron gas will behave differently from that of the bulk, as shown in Figure 1.3(a). Due to the bending of the path by the Lorentz force, electrons form skipping orbits. Hall conductivity (σ_{xy}), which has been obtained by measuring the Hall resistivity as shown in Figure 1.3(c), is found to be finite, unlike trivial insulators, and σ_{xy} is quantized depending on the number (N) of filled Landau levels. The quantized value of Hall conductivity is given by the expression, $\sigma_{xy} = \frac{Ne^2}{h}$ [2, 4]. The mysterious thing about the value of σ_{xy} is that the quantization can be measured to an accuracy 1 part in a billion. Irrespective of material forming the two-dimensional electron system and presence of disorder, which modify the Hamiltonian of the system, the value of σ_{xy} has been found to have such precise quantization. To explain the robust and quantized value of σ_{xy}, concept of topological order has been introduced in solid state electronic systems.

1.2.2 Topology in Geometry

Topology is a mathematical structure in Geometry, and this allows us to study the properties of an object, which remain unaffected by the smooth deformation of shape or size. In Figure 1.4, four three-dimensional objects have been shown, which belong to different topological class. The topological quantity which distinguishes a sphere from a torus, is called genus (g). The values of genus for sphere, torus,

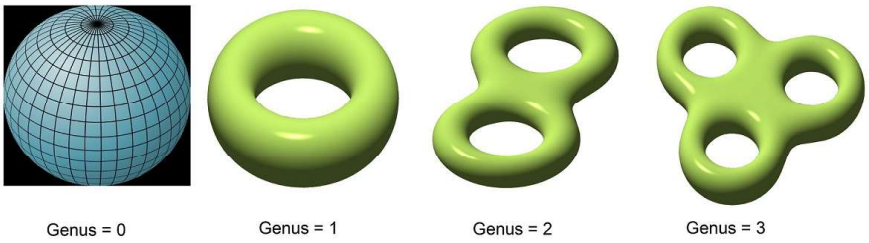

Figure 1.4: Geometrical objects with different topology. The objects are classified by the value of Genus, which is basically the number of holes in the object.

double torus, and triple torus are zero, one, two, and three, respectively. So, the value of g is basically the number of holes in an object. Since an integer can not change smoothly, objects with different genus can not be deformed into one another, and are said to be topologically distinct. In that sense, a clay ball and a plate, both of which have $g = 0$, can be deformed smoothly into one another. In other words, any two objects with the same value of g can be connected by a smooth deformation in size or shape. The genus of an object with arbitrary shape is calculated by the Gauss-Bonnet theorem,

$$\int_{Surface} KdS = 2\pi(2 - 2g), \tag{1.2}$$

where $K = \frac{1}{r_1 r_2}$ is the Gaussian curvature, and r_1 and r_2 are the radius along two perpendicular directions from a point on the surface of an object [2, 5]. Considering, $K = \frac{1}{r^2}$ on the surface of a sphere, $\int_{Surface} KdS$ has been calculated to be 4π. This implies that the value of g for a sphere is zero. If we perform similar calculation for a plate like object, it will give us the same value for g.

1.2.3 Topology in Quantum Hall Physics

How the concept of topology can be used to characterize Integer Quantum Hall states? We will explain this in this paragraph. From the mathematical point of the view, the Gaussian curvature of geometry, the Berry curvature of electronic band theory and magnetic field are same. All of them are described by the same mathematical structure: fiber bundles [5]. Now the question is: How the Berry's phase arises in solid state electronic systems? The band theory of solid classifies electronic states in terms of their crystal momentum $\mathbf{k}$, defined in a periodic Brillouin zone. The Bloch states $|u_m(\mathbf{k})>$, defined in a single unit cell of the crystal, are eigenstates of the Bloch Hamiltonian, $H(\mathbf{k})$. The eigenvalues $E_m(\mathbf{k})$ for all m, collectively form the band structure. However, the Bloch wave function, $|u_m(\mathbf{k})>$, has an intrinsic phase ambiguity, $e^{i\phi(\mathbf{k})}$. The band structure remains unaffected under the transformation, $|u_m(\mathbf{k})> \longrightarrow e^{i\phi(\mathbf{k})}|u_m(\mathbf{k})>$, which is similar to gauge transformation in electromagnetic theory. This leads to introduce a quantity similar to electromagnetic vector potential, which transforms $\mathbf{A}_m \longrightarrow \mathbf{A}_m + \nabla_{\mathbf{k}}\phi(\mathbf{k})$ under gauge transformation. So, there must be an analog of magnetic flux, $F_m = \nabla_{\mathbf{k}} \times \mathbf{A}_m$, which is invariant under the transformation [2]. This quantity is known as Berry curvature, and $\mathbf{A}_m$ is defined as $\mathbf{A}_m = i < u_m|\nabla_{\mathbf{k}}|u_m >$. Thouless, Kohmoto, Nightingale, and den Nijs have found that the surface integral of Berry curvature over the Brillouin zone is an integer, $\int_{B.Z.} F_m d^2k = n_m$, similar to genus in geometry [2, 6]. The topological invariant n_m is called Chern invariant, and the total Chern number, summed over all occupied bands, $n = \sum_{m=1}^{N} \in \mathbb{Z}$ ($\mathbb{Z}$ denotes the integer, i.e., 1, 2, ..., ∞) is invariant, provided the gap separating occupied and empty bands remains finite. n is also known as TKNN invariant. It has been identified that this n is nothing but the

integer number in the expression, $\sigma_{xy} = \frac{Ne^2}{h}$ [6]. Being a topological invariant, n in a system can not be changed under smooth deformation of Hamiltonian, i.e., without closing the gap between the occupied and empty bands. This helps us to explain the robust quantization of σ_{xy} in quantum Hall state.

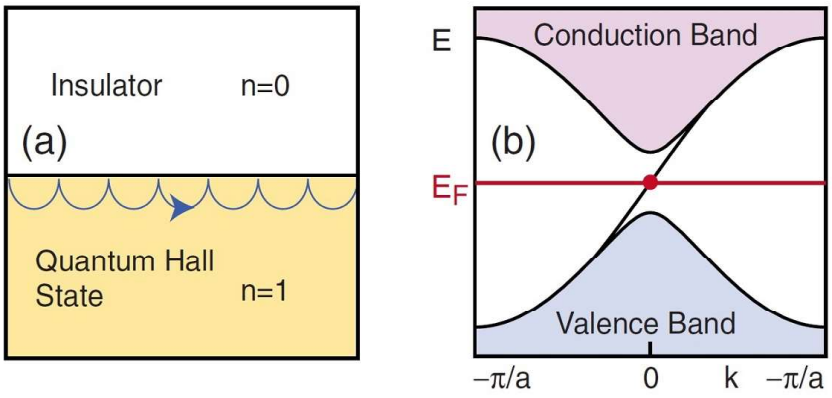

Figure 1.5: (a) The interface between a quantum Hall ground state and an trivial insulator/vacuum. (b) The electronic band structure, where a single edge state connects the bulk valence band to the bulk conduction band. Reproduced from Ref. [2].

The existence of skipping electron orbits or metallic edge state at the interface of Quantum Hall state and vacuum is the fundamental consequence of the topological classification in gapped states. Topological protection prevents states to deform smoothly from one value of n to another, across the interface of two topologically different insulators. As shown in Figure 1.5(a), the Quantum Hall ground state has the value of n equals to one [2]. Whereas, a trivial insulator/vacuum has n equals to zero. As a consequence, the Hamiltonian can not be smoothly deformed from Integer Quantum Hall state to trivial insulating state. The gap between the valence and conduction band must be close to change the value of n at the boundary. This provides an one-dimensional band dispersion for the edge

state, residing in the bulk band gap [Figure 1.5(b)] [2]. The number of edge channels at the interface of two topologically different systems is determined by the 'bulk-boundary correspondence' [2]. This relates the number of edge modes (N) intersecting the Fermi energy to the change in the bulk topological invariant (n) across the interface by the expression, $N = \triangle n$. So, a Quantum Hall state with N number of filled Landau levels will have N number of edge channels at the interface with vacuum.

1.3 Quantum Spin Hall (QSH) State

1.3.1 Discovery of QSH effect and failure of TKNN characterization

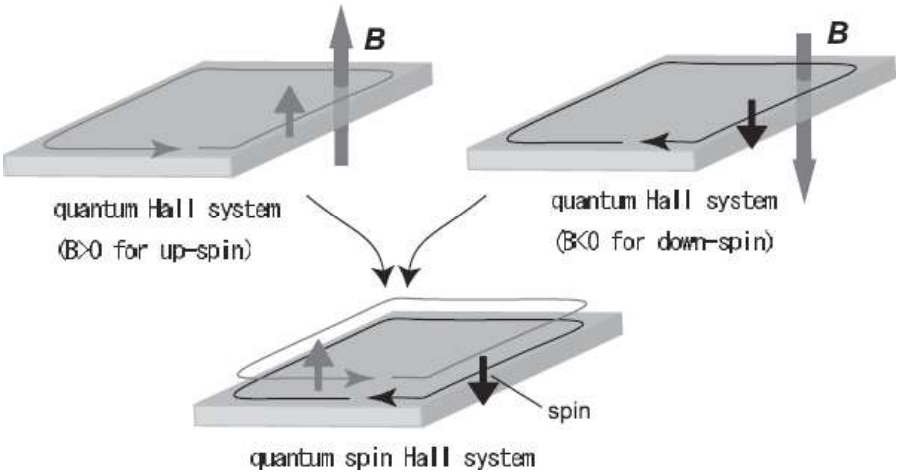

Figure 1.6: Schematic picture of the QSH system as a superposition of two QH systems. Reproduced from Ref. [8].

Discovery of Quantum spin Hall insulator state in HgTe quantum-well by Molenkamp and his collaborators, in the year 2007, is the next milestone in clas-

sifying electronic states of matter in terms of their underlying topology [7]. The two-dimensional quantum-well structure was made by sandwiching a thin layer of mercury telluride (HgTe) between layers of cadmium telluride (CdTe). In QSH state, time reversal symmetry is preserved due to absence of external magnetic field and spin-orbit coupling plays an important role in generating intrinsic magnetic field, unlike IQH state. The single particle effective Hamiltonian, governing the Quantum Spin Hall physics is,

$$H = \frac{(\mathbf{p} - e\mathbf{A}\sigma_z)^2}{2m}, \tag{1.3}$$

where σ_z is the z-component of Pauli matrices. It is evident from the second term (within the bracket) in the numerator that an effective magnetic field acts in the upward direction on up-spin and in the downward direction on down-spin. As a result, electrons with upward spin move in a separate conducting channel, opposite to the spin-down electrons, at the edge of the sample. So, a QSH phase can be realized by a superposition of two quantum Hall systems for the up and down spins, as shown in Figure 1.6 [8]. However, there is no net flow of charge, but net spin current in QSH state. A QSH insulator can not be characterized by the TKNN invariant ($n \in Z$). This is because the integer topological invariant for up-spin electrons ($n\uparrow$) is equal and opposite to the down-spin electrons ($n\downarrow$) in presence of time reversal symmetry, and as a consequence, n ($=n\uparrow + n\downarrow$) is zero. Considering the role of spin-orbit interaction and time-reversal ($\mathcal{T}$) symmetry, Kane, Mele, and others have introduced a new topological invariant, ν [9, 10].

1.3.2 Role of time-reversal symmetry

To understand this new topological class, we have to examine the role of $\mathcal{T}$ symmetry for spin-$\frac{1}{2}$ particles. The $\mathcal{T}$ symmetry in an arbitrary spin system is represented by an anti-unitary operator, $\Theta = exp(\frac{i}{\hbar}\pi S_y)K$, where S_y is the spin operator and K is the complex conjugate. Existence of time-reversal symmetry implies that Θ commutes with the Hamiltonian of the system (where Ψ represents the wave function of the system), i.e.,

$[\Theta, H]\Psi = 0$

$\Rightarrow \Theta H\Psi - H\Theta\Psi = 0$

$\Rightarrow \Theta H\Psi = H\Theta\Psi$

Let, Ψ is the rth eigen state of H, i.e., $H\Psi = \varepsilon_r\Psi$. This implies, $H\Theta\Psi = \varepsilon_r\Theta\Psi$. So, $\Theta\Psi$ is also the rth eigen state of H. Now, there are two possibilities: (a) Ψ and $\Theta\Psi$ are same, and (b) Ψ and $\Theta\Psi$ are different wave functions, i.e., ε_r is doubly degenerate. To identify the right one, we have to consider the following effect of $\mathcal{T}$ symmetry operation on spin-half system. In a spin-half system, Θ flips the direction of the spin by 180^0 and wave function gains a minus sign by the two times operation of Θ, i.e., $\Theta^2\Psi = -\Psi$.

Suppose, $\Psi = \Theta\Psi$

$\Rightarrow \Theta^2\Psi = \Theta\Psi = \Psi$

$\Rightarrow \Psi \neq \Theta\Psi$

So, condition (b) is right, which states Ψ and $\Theta\Psi$ are independent wave functions, i.e., ε_r is doubly degenerate. This is the famous Kramer's theorem, which states that "all eigenstates of a $\mathcal{T}$-invariant Hamiltonian of spin-half system are twofold degenerate".

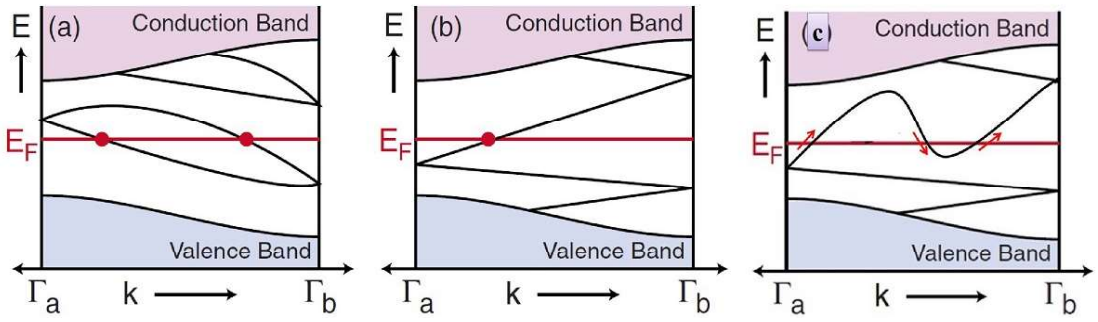

Figure 1.7: (a) The edge states cross the Fermi level an even (zero) number of times. (b) The edge states cross the Fermi level once. (c) The edge states cross the Fermi level an odd number of times. Reproduced from Ref. [2].

If the Kramer's theorem is applied for the Bloch wave state of solid, it will be found that for any Bloch wave state Ψ_k, there is another state $\Theta\Psi_{\mathbf{k}} = \Psi_{-\mathbf{k}}$ of same energy. So, Kramer's doublets are located at different momentum point **k** and **-k**. Only at $\mathbf{k} = 0$ and $\mathbf{k} = \pi$ (considering lattice parameter is a unit quantity), both the points are the same. This implies that at $\mathbf{k} = 0$ and $\mathbf{k} = \pi$, each Bloch state comes in pair. On the other hand, single particle Hamiltonian of an electronic system smoothly deforms from the bulk to edges. If any edge state is induced inside the bulk band gap, at $\mathbf{k} = 0$ and $\mathbf{k} = \pi$, it will be doubly degenerate. Away from these special points, the spin-orbit interaction will split the degeneracy. As electronic band dispersion is continuous, the states at $\mathbf{k} = 0$ and $\mathbf{k} = \pi$ have to be connected. But there is only two possible ways [Figure 1.7], through which they can connect. For the first case [Figure 1.7 (a)], edge state crosses the Fermi level at an even (zero) number of points. So, there will be even numbers of conducting channels or no channel at the edge. In this case, the edge states can be eliminated by tuning the Fermi level, or by smooth deformation of Hamiltonian in such a way that all the Kramer's doublets appear outside the gap. In conclusion, pairwise interconnection of states at $\mathbf{k} = 0$ and $\mathbf{k} = \pi$ gives rise to trivial insulating phase. For

the second case [Figure 1.7(b)], when the edge band crosses the Fermi level once, there is single conducting edge channel. This type of edge state is unavoidable under any smooth deformation of Hamiltonian or shifting of Fermi level. In this context, one can suggest the third possibility [Figure 1.7(c)], where the edge band crosses the Fermi levels three times. However, this type of connection will generate two right-moving and one left-moving channel, and as a consequence, there will be an effective single conducting edge state. The one-to-one connection of states at $\mathbf{k} = 0$ and $\mathbf{k} = \pi$, as shown in Figure 1.7(b) and Figure 1.7(c), leads to topologically protected metallic boundary states. Which of the above-mentioned scenarios will occur at the edge, will be determined by the topological class of the bulk band structure?

1.3.3 $\mathbb{Z}_2$ topological classification

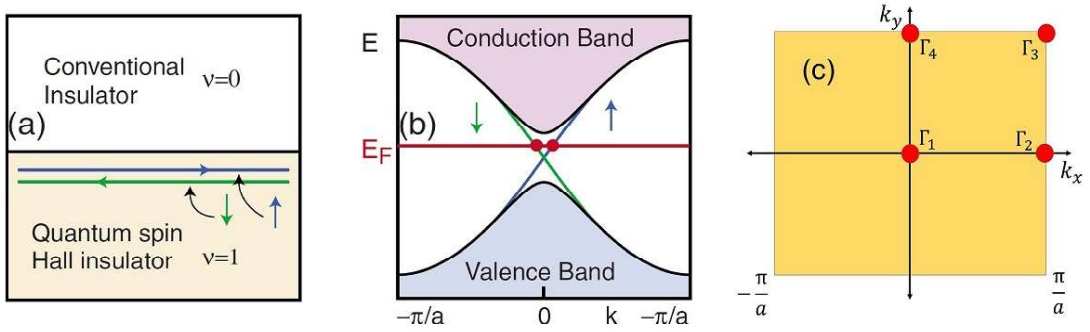

Figure 1.8: (a) The interface between a QSH insulator and an ordinary insulator.(b) The edge state dispersion. (c) High-symmetry points in 2D bulk Brillouin zone. Figure (a) and (b) are reproduced from Ref. [2].

According to the 'bulk-boundary correspondence' principle, the number of edge modes has to be equal to the change in the bulk topological invariant ($\triangle\nu$)

across the interface. This implies that the bulk topological invariant (ν) for two-dimensional insulating states in presence of time-reversal symmetry, has to be either zero or one. ν obeys all the group operations of two-dimensional cyclic group ($\mathbb{Z}_2$) such as, $\mathbf{a} \oplus \mathbf{a} = \mathbf{a}$, $\mathbf{a} \oplus \mathbf{b} = \mathbf{b}$ and $\mathbf{b} \oplus \mathbf{b} = \mathbf{a}$, where $\mathbf{a}$ and $\mathbf{b}$ are the two group elements, and $\mathbf{a}$ is the unity element of $\mathbb{Z}_2$. As a consequence, ν has been named as '$\mathbb{Z}_2$ topological invariant'. As shown in Figure 1.8(a), for Quantum Spin Hall insulator, ν encounters a unit change across the interface with trivial insulator/vacuum. This leads to single edge state for spin-up electron state and spin-down electron state, separately. Figure 1.8(b) shows the corresponding band structure in first Brillouin zone. Now the question is: "how the value of ν is determined for a two-dimensional insulating state in presence of time-reversal symmetry?" There are several mathematical formalisms for determining the value of ν, however, the method, which has been developed by Fu and Kane, will be mentioned here [11]. In order to calculate ν, the authors have initially defined a unitary matrix $w_{mn}(\mathbf{k}) =< u_m(\mathbf{k}) \mid \Theta \mid u_n(\mathbf{k}) >$, using the occupied Bloch functions. As $\Theta^2 = -1$, it can be shown that $w^T(\mathbf{k}) = -w(-\mathbf{k})$. For a two-dimensional electronic system, there are four inequivalent special points in the bulk Brillouin zone, which have been identified as $\Gamma_{a=1,2,3,4}$, in Figure 1.8(c). In these points, $\mathbf{k}$ and -$\mathbf{k}$ are equivalent, which makes $w(\Gamma_a)$ antisymmetric matrix. The determinant of an antisymmetric matrix is the square of its pfaffian, which allows us to define a quantity, $\delta_a = \frac{\mathrm{Pf}[w(\Gamma_a)]}{\sqrt{\det[w(\Gamma_a)]}} = \pm 1$. The invariant ν is determined by the expression,

$$(-1)^{\nu} = \prod_{a=1}^{4} \delta_a. \tag{1.4}$$

1.4 Three-dimensional Topological Insulators

Shortly after the discovery of QSH insulator in two-dimension, its three-dimensional (3D) counterpart has been realized theoretically, which has been named as ' 3D topological insulator (3D TI)' [12, 13]. Similar to the conducting edge state of 2D-QSHI, 3D TI has topology protected surface state which crosses the Fermi level, residing in the bulk band gap. Time-reversal invariant 3D bulk insulating state has also been characterized by $\mathbb{Z}_2$ topological invariant. However, 3D topological insulators are described by four $\mathbb{Z}_2$ topological invariants $(\nu_0;\nu_1\nu_2\nu_3)$, instead of single invariant in two dimensions. ν_0 is known as strong topological index, and the other three are known as weak topological indices. It is customary to write the combination of the four invariants in the form $(\nu_0;\nu_1\nu_2\nu_3)$, because $(\nu_1\nu_2\nu_3)$ can be interpreted as Miller indices to specify the direction of vector Γ_a in the reciprocal space. In the following section, we will discuss two types of 3D TI state, depending on the value of ν_0 [2, 3].

1.4.1 Weak topological insulators

$\nu_0 = 0$ represents the simplest 3D TI, which can be understood by stacking the layers of QSHI, with weak interlayer coupling. The orientation of layers is described by $(\nu_1\nu_2\nu_3)$ such as, (0 0 1) represents stacking along **z**-axis. The conducting edge-state of monolayers, as shown by the blue arrows in the Figure 1.9, forms a topological surface state in bulk sample. A simple cubic Brillouin zone for the three-dimensional bulk electronic system has eight time-reversal invariant points, which have been shown by red dots in Figure 1.9(b). Each of the planes in the

Brillouin zone (e.g., $k_i = 0, \pi$ planes) containing four such points, is characterized by a 2D invariant, which is calculated using the equation,

$$(-1)^{\nu_{i=1,2,3}} = \prod_{a=1}^{4} \delta_a. \tag{1.5}$$

Earlier, it was believed that the surface state is present for a clean sample of a weak TI (WTI), but in presence of disorder, it can be localized. Later on, the surface states of WTI are found to be protected from random impurities and disorders, which do not break the time-reversal symmetry and close the bulk energy gap [14]. As a consequence, the surface conductance of a WTI remains finite even in presence of strong disorder. $Bi_{14}Rh_3I_9$ is one of the compounds, which has been experimentally addressed to be a weak TI [15].

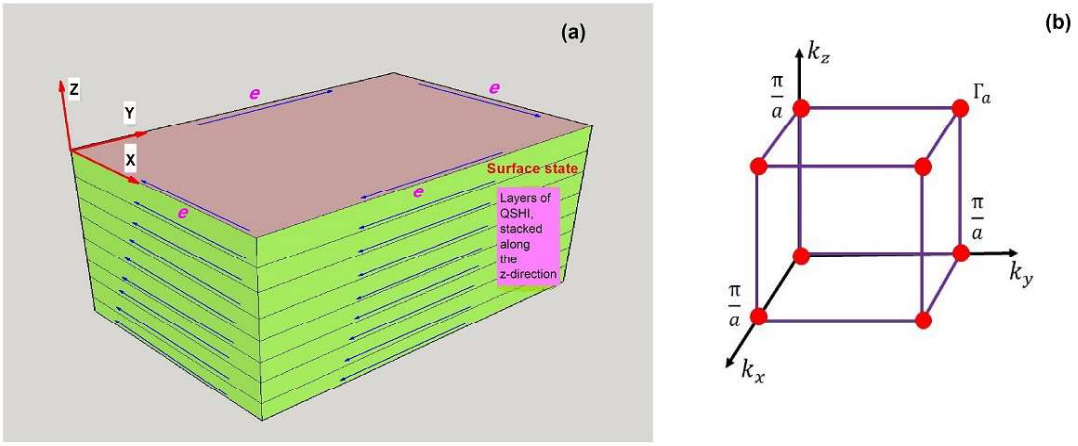

Figure 1.9: (a) Weak three-dimensional topological insulators. (b) High-symmetry points in 3D bulk Brillouin zone.

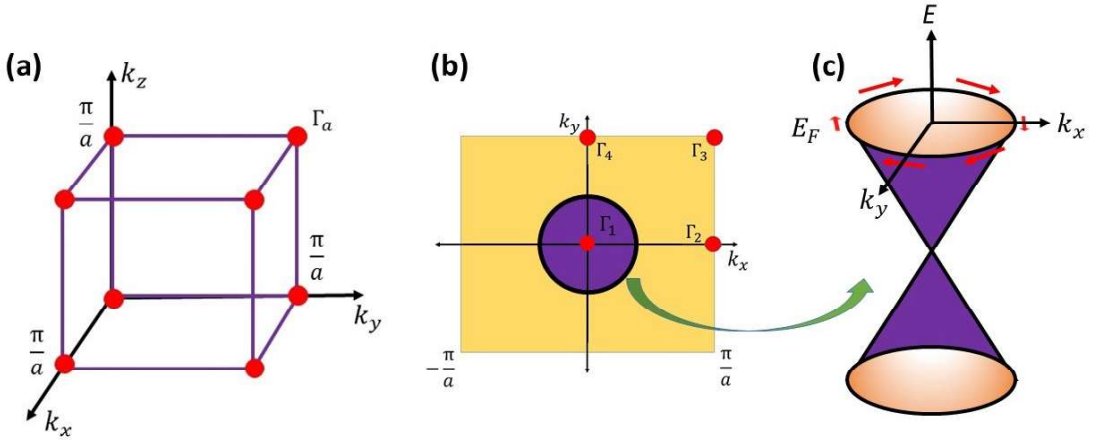

Figure 1.10: (a) High-symmetry points in 3D bulk Brillouin zone. (b) Constant energy contour at the Fermi level. (c) 2D Dirac cone surface state and spin-momentum locking.

1.4.2 Strong topological insulators

The strong topological invariant, ν_0, for a three-dimensional bulk insulating state is determined by the expression,

$$(-1)^{\nu_0} = \prod_{a=1}^{8} \delta_a, \tag{1.6}$$

where 'a' is the index of time-reversal invariant points [Figure 1.10(a)] of bulk Brillouin zone. The materials, where the value of ν_0 is found to be one, are known as strong topological insulators. As all the eight time-reversal invariant points are involved in determining the value of ν_0, strong TI state cannot be interpreted as a descendant of the 2D-QSHI. The surface Brillouin zone, as shown in Figure 1.10(b), consists of four time-reversal invariant points, where the surface state must be Kramers degenerate. Away from these special points, the spin-orbit interaction lifts the degeneracy. As discussed in Section 1.3.2, for non-trivial surface state, the surface band structure must resemble the situation in Figure 1.7(b). By looking

the constant energy contour of the Fermi level [Figure 1.10(b)], one can see that the surface Fermi circle encloses odd number of time-reversal invariant points for strong 3D TI. The novelty of this conducting surface state is the rich physics associated with the electronic band dispersion [2, 3]. It has been found that the dynamics of charge carriers on the surface of a 3D TI is governed by the Dirac-type effective Hamiltonian,

$$H_{sur}(k_x, k_y) = -\hbar v_F \hat{z} \times \vec{\sigma}.\vec{k}. \tag{1.7}$$

As a consequence, the energy and momentum of charge carriers follow gapless linear dispersion [Figure 1.10(c)], unlike conventional electronic system, where the dispersion relation is quadratic in nature. Another interesting characteristic of 3D TI surface state is that the spin of the charge carriers is always perpendicular to its momentum direction, known as spin-momentum locking. This makes the motion of charge carriers robust, against the non-magnetic impurity in a sample. This can be inferred from a simple logic. If there is any non-magnetic impurity in the system, to change the direction of motion of charge carrier, the impurity has to flip the direction of the spin. However, a scalar field (impurity potential) cannot affect a vector field (spin). So, there will be no backscattering of charge carriers.

Following the specific prediction of Fu and Kane [16], the 3D TI state has been first experimentally identified in $Bi_{0.9}Sb_{0.1}$ by Princeton University group led by Hasan, through the angle-resolved photoemission spectroscopy (ARPES) experiment [17]. This material is an alloy of Bi and Sb, which possesses two essential features: (i) band inversion at odd number of time-reversal invariant momentum points in the bulk Brillouin zone, and (ii) opening of band gap at these points. This leads to non-trivial bulk $\mathbb{Z}_2$ topological invariant, which has been identified as (1; 1 1 1). The surface electronic band structure of this compound has been

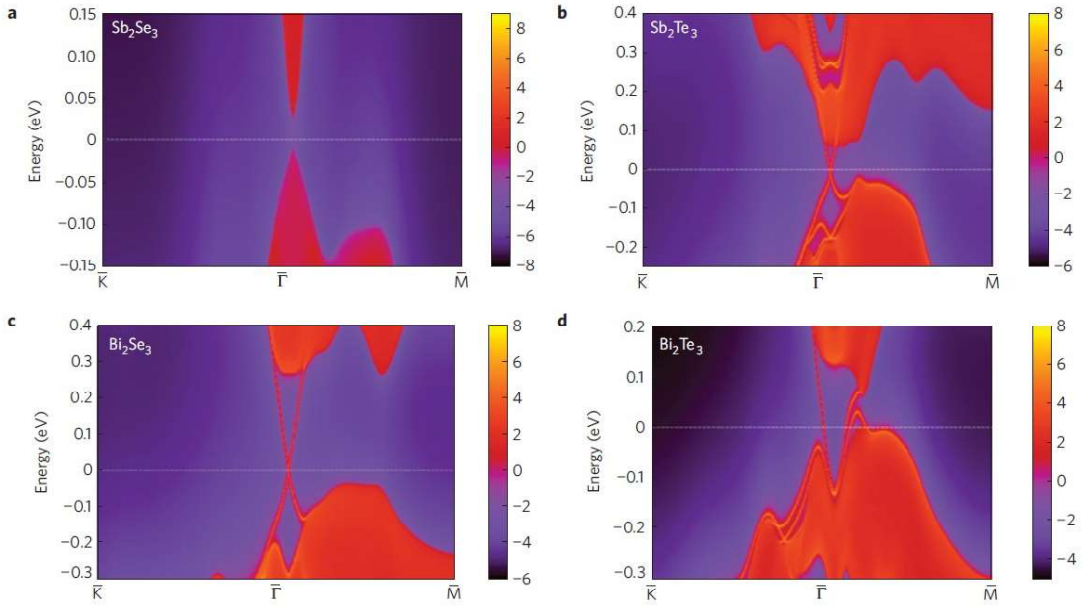

Figure 1.11: (a)-(d) Energy and momentum dependence of the local density of states for the Bi_2Se_3 family of materials on the [111] surface. A warmer color represents a higher local density of states. Red regions indicate bulk energy bands and blue regions indicate a bulk energy gap. The surface states can be clearly seen around the Γ point as red lines dispersing inside the bulk gap. Reproduced from Ref. [18].

found to be complicated and the bulk band has a small insulating gap. As a consequence, at finite temperature, due to presence of thermally excited carriers, the quadratic bulk band has significant contribution in electronic transport. However, the overwhelming goal in the research on 3D TI is the realization of transport properties associated with the conducting surface state and utilization of this in next generation electronic device. To achieve this goal, it is necessary to find new materials, which have single spin-momentum locked Dirac cone surface state and large insulating gap in the bulk. Zhang *et al.* came up with a concrete prediction that Bi_2Se_3, Bi_2Te_3, and Sb_2Te_3 are 3D TIs but Sb_2Se_3 is not [18]. The electronic band structures of these materials, containing isolated surface and bulk states, are shown in Figure 1.11(a)-(d). Experimentally, the existence of a single Dirac-cone

surface state was reported in 2009 for Bi_2Se_3 by Xia *et al.* [19], for Bi_2Te_3 by Chen *et al.*[20] and also by Hsieh *et al.* [21], and for Sb_2Te_3 by Jiang *et al.* [22].

1.5 Three-dimensional Dirac semimetal

The research on TI and the experimental discovery of graphene band structure [Figure 1.12] have triggered a tremendous interest in condensed matter physics, over the past decade. The energy-momentum dispersion of charge carrier as well as the form of the underlying Hamiltonian for the surface state of 3D TI and in the bulk of graphene are reminiscent of those for massless fermions, usually studied in high-energy physics, with two relevant differences. First, the characteristic velocity that appears in condensed matter physics is roughly two orders of magnitude smaller than the speed of light. And second, both in graphene and 3D TIs, the electrons are constrained to move in two spatial dimensions, whereas the framework of relativistic quantum mechanics was established to describe fermions in three spatial dimensions. However, the constant efforts for the realization of relativistic particles in table top experiments result in new quantum phases of matter, which have linear dispersion along all the three momentum (k_x, k_y, k_z) directions in the shape of a cone. The materials, which host this type of electronic band structure are known as 3D Dirac semimetals.

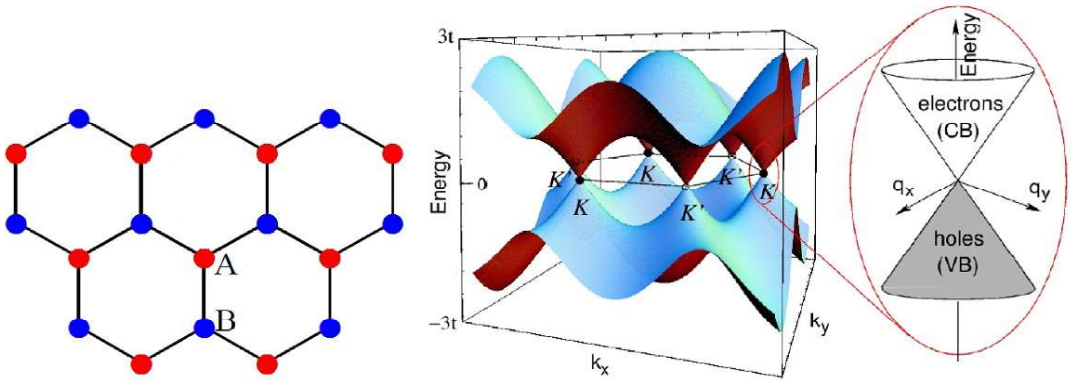

Figure 1.12: Left: Honeycomb lattice of graphene. **A** and **B** are the two types of lattice, identified for band structure calculations, using tight-binding model. Right: Energy bands of graphene obtained from the tight-binding model and zoom around the Dirac point at K. Reproduced from Ref. [23].

1.5.1 3D Dirac semimetal state at quantum critical point

It has been predicted that 3D Dirac semimetal state can be realized at a quantum critical point in the phase transition from a trivial insulator to a topological insulator [8, 16]. In an insulating material, the bulk band gap can be tuned by chemical doping or external pressure, which actually changes the lattice parameters and spin-orbit coupling in the system. This type of physical operation can even change the parity of an insulating gap from trivial to non-trivial, and vice versa. In the process of band evolution, the insulating gap for an inversion symmetric crystal has been found to be zero at some unique value of tuning parameter. At this critical value, the bulk conduction and valence bands touch at a special point in momentum space (which is known as 'Dirac node'), and the dynamics of quasi-particles in the bulk electronic band of the material is governed by the Dirac-type equation

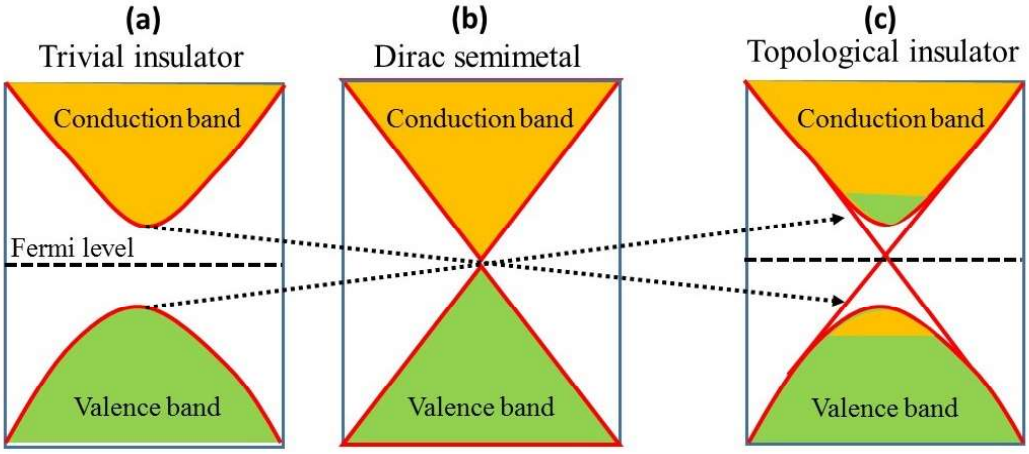

Figure 1.13: Schematic band inversion between two bands: The trivial band gap in (a) closes at a critical point in (b), and reopens inverted in (c) with the two states swapping their orbital characters at the symmetry point.

for massless fermion in three dimensions,

$$i\frac{d\Psi}{dt} = H\Psi = \hbar V_F \begin{pmatrix} \overrightarrow{\sigma}.\overrightarrow{k} & 0 \\ 0 & -\overrightarrow{\sigma}.\overrightarrow{k} \end{pmatrix} \Psi. \tag{1.8}$$

Here, $\overrightarrow{\sigma}$, $\overrightarrow{k}$ and V_F are the Pauli spinor, crystal momentum, and Fermi velocity of charge carriers, respectively. In solid state crystallographic environment, speed of light (c) and linear momentum ($\overrightarrow{p}$) of original Dirac equation are replaced by V_F and $\overrightarrow{k}$, respectively. As the Pauli matrices are two-dimensional, H is a 4×4 matrix, and the Equation 1.8 has four components. Following the theoretical prediction [16, 24], the 3D Dirac semimetal state has been naively identified in $Bi_{1-x}Sb_x$ at a quantum critical point x = 0.04, through ARPES experiment [17]. Later on, similar topological phase transition has been observed in $BiTl(S_{1-\delta}Se_\delta)_2$, which is shown in Figure 1.14 [25]. With increasing selenium concentration, the direct bulk band gap reduces from 0.15 eV at $\delta = 0.0$ to 0.05 eV at $\delta = 0.4$. At $\delta = 0.6$, the bulk

conduction and valence bands touch each other, resulting a 3D Dirac dispersion. For compositions $\delta \geq 0.6$, the material becomes an inverted indirect band gap insulator with spin-polarized topological surface state. However, $Bi_{1-x}Sb_x$ and $BiTl(S_{1-\delta}Se_\delta)_2$ fail to create significant excitement due to some limitations. As the Dirac cone state appears at a particular chemical composition in these compounds, it is not robust against uncontrolled doping during sample preparation. In addition, it has been found that the presence of conventional quadratic band masks the non-trivial band, which undergoes topological phase transition with chemical doping.

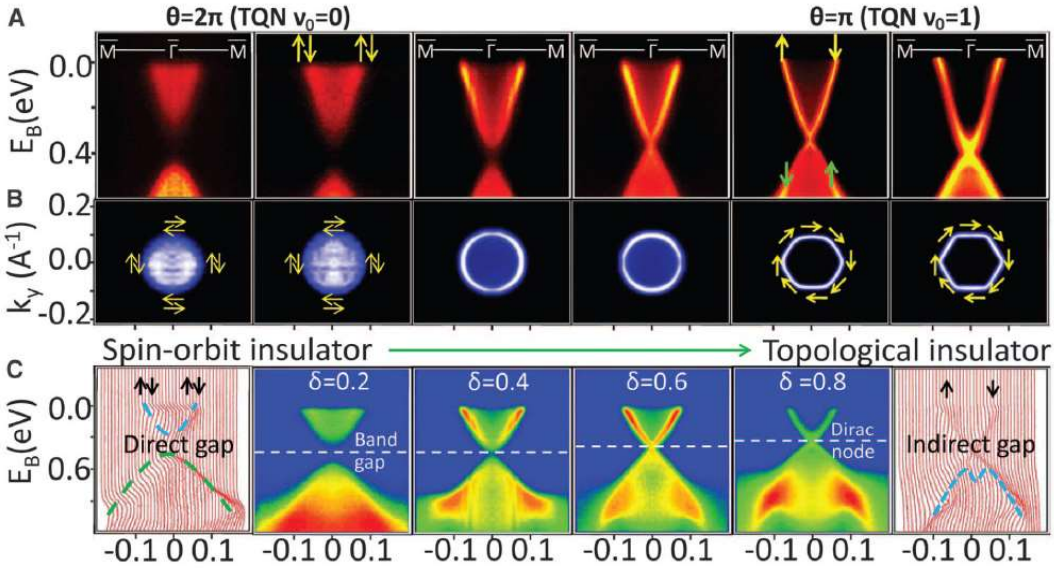

Figure 1.14: Topological phase transition in $BiTl(S_{1-\delta}Se_\delta)_2$. (A) High-resolution ARPES dispersion maps from a spin-orbit band insulator (left panel) to a topological insulator (right panel). Topological quantum numbers (TQN) are denoted by topological invariant ν_0. (B) ARPES-mapped native Fermi surfaces and their spin-texture for different chemical compositions (from left to right, $\delta = 0.0$ to $\delta = 1.0$). (C) Left and right panels: Energy distribution curves for stoichiometric compositions $\delta = 0.0$ and $\delta = 1.0$, respectively. Center panels: ARPES spectra indicating band gap and Dirac node for compositions $\delta = 0.2$ to $\delta = 0.8$. Figures are adopted from Ref. [25].

1.5.2 Crystalline symmetry protected 3D Dirac semimetal

It is important to note that the previously discussed scenario of topological phase transition and the emergence of Dirac cone state at the quantum critical point do not take into account any additional space group symmetries, which, if present may alter the conclusion [8]. Several theoretical studies have predicted the existence of second generation 3D Dirac semimetals, where the Dirac cone band appears from the protection of certain space group crystalline symmetries, and are, therefore, proposed to be more robust to disorders or chemical alloying [26, 27, 28]. For example, theoretical studies have identified Na_3Bi and Cd_3As_2 as 3D Dirac semimetals, which are protected by the C_3 and C_4 crystalline rotational symmetry, respectively [27, 28]. This type of Dirac semimetal, which is also known as 3D topological Dirac semimetal (TDS), differs from the earlier-mentioned type because it possesses strong spin-orbit coupling driven inverted bulk band structure. At the special momentum points along the symmetry axis, the band crossings are protected by the space group symmetry. Since both time-reversal and inversion symmetries are present, there is a fourfold degeneracy at these points, around which the band dispersions can be linearized, resulting in a 3D massless Dirac semimetal. The C_4 rotational symmetry protected unavoidable band crossing in Cd_3As_2 is shown in Figure 1.15(a), as a representative. The surface state of TDS is also distinct from the closed constant energy contour in 3D TIs [Figure 1.15(b)], identified as Fermi arc. As shown in Figure 1.15(c), spin-momentum locked arc-like contour at the Fermi level connects two discrete points in surface Brillouin zone, which are the projection of bulk Dirac nodes on the surface. There is another important difference between the surface state of 3D TI and TDS in the spin texture on the constant energy contour. The magnitude of spin projection perpendicular

to momentum directions is constant throughout the closed loop in case of 3D TI. Whereas, in TDS, it gradually tends to zero as the Fermi-arc approaches towards the points of discontinuity.

Understanding the dynamics of relativistic Dirac fermions in table-top experi-

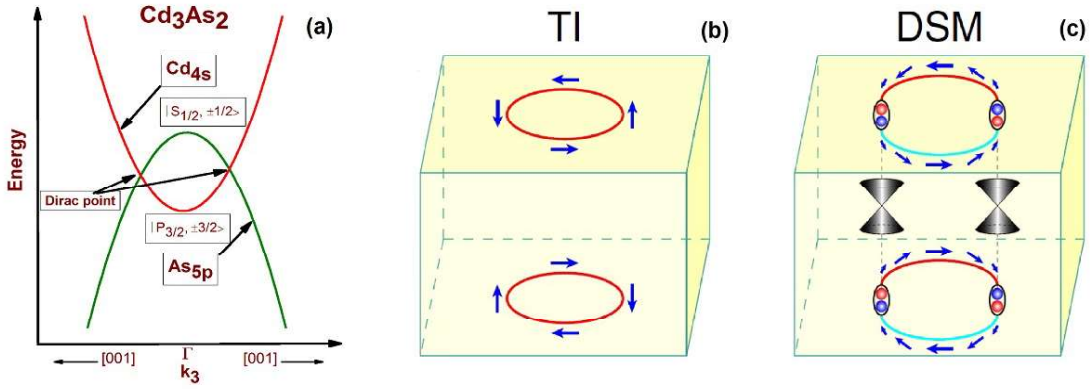

Figure 1.15: (a) C_4 rotational symmetry protected unavoidable band crossing in Cd_3As_2, as a representative. Here, k_3 is the third momentum direction, i.e., k_3 direction. (b) Schematic of the spin-polarized surface states in a 3D TI. (c) Schematic of a TDS with spin-polarized Fermi arcs on its surface connecting projections of two bulk Dirac nodes. The red and blue balls, surrounded by a black boundary indicates that one Dirac node is the degeneracy of two Weyl nodes, which will be discussed in the following section. Figure (b) and (c) are reproduced from Ref. [29].

ments is not the only fundamental importance of TDS phase in solid state electronic systems. It has been predicted that by breaking different symmetries of a crystal, having this novel electronic phase, different new quantum phases of matter can be observed [27, 28]. It has been theoretically understood that under broken time-reversal symmetry scenario, in external magnetic field or upon magnetic impurity doping, TDS acts like a 3D Topological Weyl semimetal (TWS). Breaking the inversion symmetry of a TDS, 3D TI state or TWS state can be induced, depending on the crystalline space group symmetry of the material. By tuning the space group symmetry of a TDS, axion insulator state can be induced. Chemical

doping can also lead to new exotic phases such as, topological superconductivity. However, discussion on all the topological phase transitions is beyond the scope of the present thesis. Only the first one is relevant to this thesis. We will provide a brief overview on TWS state of matter, before going to discuss the experimental discovery of space group symmetry protected Dirac semimetals and the recent advancement in experiment.

1.5.3 Understanding TWS as a transmuted state of TDS

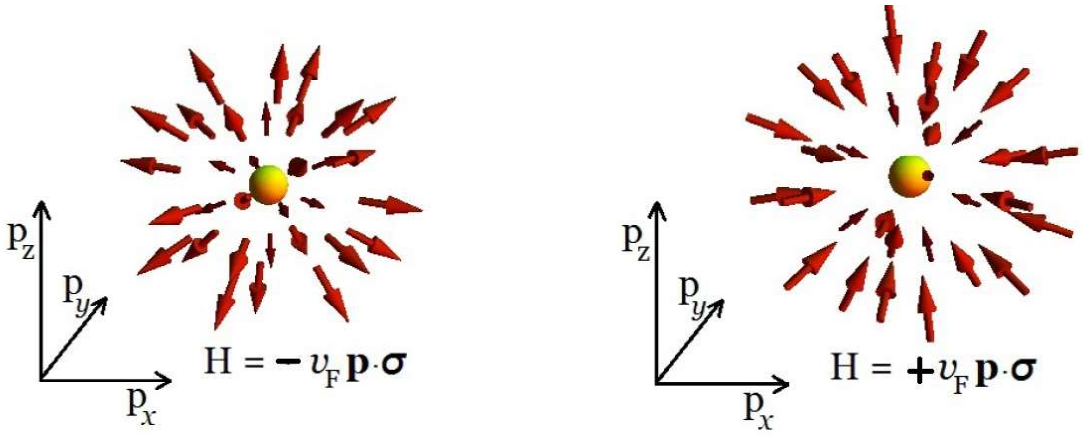

Figure 1.16: Weyl nodes of opposite chirality. The arrows indicate the direction of the spin vector, which can be parallel or antiparallel to the momentum vector.

In the year 1929, Hermann Weyl proposed that a four-component massless Dirac equation [Equation 1.8] in three dimensions can be separated into two two-component equations [30],

$$i\frac{d\Psi}{dt} = H\Psi = \pm c\overrightarrow{\sigma}.\overrightarrow{p}\Psi. \tag{1.9}$$

The above equation describes particles with a definite projection of spin to its

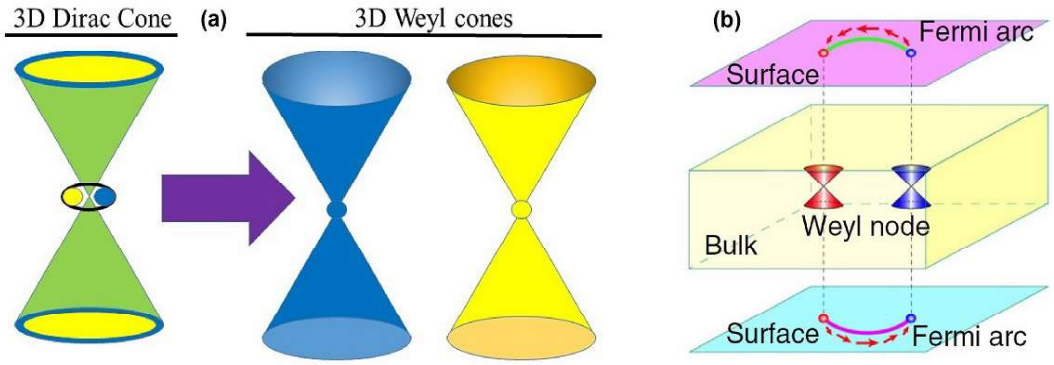

Figure 1.17: (a) A four-component 3D Dirac node in a TDS as a superposition of two two-component Weyl nodes, and the splitting of Dirac cone into two Weyl cones of opposite chirality under broken time-reversal symmetry. (b) Schematic of a WSM with spin-polarized Fermi arcs on its surfaces connecting the projections of two Weyl nodes with opposite chirality. The red and blue colors of the bulk Weyl cones and the corresponding projection points on the surfaces represent opposite chirality of the Weyl nodes. The red arrows on the surfaces indicate the spin texture of the Fermi arcs. Figure (b) is reproduced from Ref. [29].

momentum, known as Weyl fermions. When the sign on the right hand side of the equation is positive, $\overrightarrow{\sigma}$ has to be antiparallel to $\overrightarrow{p}$, to minimize the energy. Massless fermions, obeying this specific spin orientation, are the positive chirality Weyl fermions. Again for the particles, which obey the above-mentioned equation with the negative sign, the spin has to be parallel to the momentum direction. This type of particles are called negative chirality Weyl fermions. If we look at the momentum space [Figure 1.16], it will be found that the expectation value of $\overrightarrow{\sigma}$ in an eigenstate of a given chirality forms a vector field, like a hedgehog. In condensed-matter physics, specifically in solid-state band structures, Weyl fermions appear when two electronic bands cross and low energy effective Hamiltonian around the band crossing point mimics the expression, $H = \pm c\overrightarrow{\sigma}.\overrightarrow{p}$. The crossing point is called a Weyl node, away from which the bands disperse linearly in the lattice momentum, giving rise to 3D Weyl semimetal state. As illustrated in Figure 1.17(a),

the TWS state can also be generated by breaking the time-reversal symmetry or inversion symmetry of a 3D Dirac semimetal, where a single four-component Dirac cone splits into two two-component Weyl cones. Theory also predicts that the materials, which possess Weyl fermions in the bulk electronic state, would exhibit a new kind of surface state: an open Fermi arc that would connect two Weyl nodes and then continue on the opposite surface of the material [Figure 1.17(b)] [31]. In the year 2015, two groups simultaneously predicted the existence of Weyl-type electronic excitations in TaAs, TaP, NbAs, and NbP [32, 33]. Subsequent after the theoretical predictions, the first experimental discovery of Weyl semimetal state in TaAs family of materials has been done by Xu *et al.* [34] and Lv *et al.* [35].

1.5.4 Experimental discovery of TDS

Following the theoretical prediction [27, 28], investigation on electronic band structure of Na_3Bi and Cd_3As_2 through ARPES experiment have established the Dirac cone band dispersion in these compounds [36, 37]. Stacking plots of constant-energy contours at different binding energies for both the compounds are shown in Figure 1.18, where the gradually increasing radius of the circular contours lies on a straight line passing through the Dirac nodes. Immediate after the observation of bulk Dirac cone band, Yi *et al.* and Xu *et al.* have revealed the existence of Fermi-arc surface state in Cd_3As_2 and Na_3Bi [38, 39]. Although both the materials are equally compelling, experimental research on Na_3Bi has been found to be little challenging compared to Cd_3As_2 due to its extreme sensitivity to air. Later on, 3D topological Dirac semimetal phase was theoretically predicted and experimentally proposed in plenty of compounds. However, the existence of this novel electronic phase has been unambiguously established in a very few materials. $ZrTe_5$ and

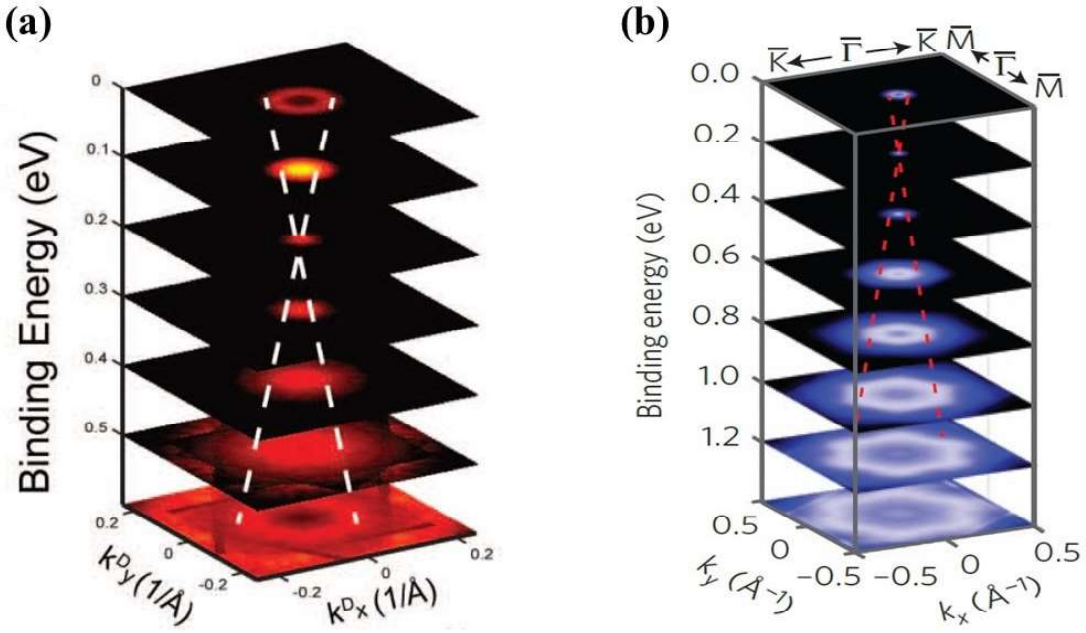

Figure 1.18: Stacking plot of constant-energy contours at different binding energies shows Dirac cone band structure. (a) White dashed lines are the guide to the eye that trace the linear dispersions in Na_3Bi. Figure reproduced from Ref. [36]. (b) Red dotted lines are guide to the eye that indicate the linear dispersions and intersect at the Dirac point in Cd_3As_2. Figure reproduced from Ref. [37]

ZrSiS are the examples of materials, which have emerged as suitable candidates for extensive experimental research [40, 41, 42].

1.6 Context, goal and outline of the thesis

Just after the experimental discovery of topological Dirac semimetal state in Cd_3As_2 and Na_3Bi, we have found great interest to this novel electronic phase of matter. At that time, TDS state in other compounds was not discovered, and very few transport experiments including SdH oscillation study on Cd_3As_2 were reported in preprint server, which will be mentioned in the following chapters. Although the

complete picture of electronic band topology was not known and different unique electronic phenomena were not explored, it was realized that the materials having TDS state are equally compelling for fundamental physics research and technological application. Considering our existing transport and magnetization measurements facility, we have focused our research on different exotic magneto-transport properties, nature and geometry of Fermi surfaces through quantum oscillation, non-trivial electronic or magnetic responses from topological fine structure, and scattering mechanism of charge carriers in some 3D Dirac semimetals. Three compounds Cd_3As_2, $ZrTe_5$, and $TaSb_2$ have been considered for the present thesis. This selection is based on earlier First Principles Calculation, ARPES, or transport experiments. In the respective chapters, we discuss the specific motivation behind each research. The organization of the thesis is as follows.

In Chapter 2, we describe briefly the method through which we have prepared the single crystals of relevant materials. A short description on the instruments and the techniques, which have been used to characterize and measure different physical properties of a material, is also given in this chapter. In chapter 3, we present the results on the Fermi surface of Cd_3As_2, which has been probed by both the de Haas-van Alphen (dHvA) and Shubnikov-de Haas (SdH) oscillations techniques. The geometry of the Fermi surface is determined and the values of the Fermi wave vector, Fermi velocity, and effective cyclotron mass of the charge carrier are calculated. We compare and contrast our results from dHvA technique with the results from SdH oscillations. Chapter 4 is devoted to the systematic temperature and magnetic field dependence study of the Seebeck coefficient (S), to determine the carrier scattering mechanism in Cd_3As_2 single crystal. We also

present the effect of carrier doping on scattering mechanism, magnetotransport properties and Fermi surface, with 2% and 4% In doping at Cd site. In Chapter 5, following the ambiguity between the earlier experimental results and theoretical predictions, we describe the results of our magnetotransport and magnetization measurements on $ZrTe_5$ single crystal. We have measured magnetoresistance in current parallel to magnetic field configuration to detect 3D Dirac fermion in the bulk and magnetization to probe the surface state. We combine the results of transport and magnetic measurements to address the ambiguity in topological nature of electronic band structure. Chapter 6 covers our research on the single crystal of proposed Dirac Semimetal $TaSb_2$. We reveal angular variation in transverse magnetoresistance (TMR) by applying magnetic field along different crystallographic directions through a sample rotator. To probe the anisotropy in the Fermi surface, we have measured dHvA oscillations for the magnetic field applied along **a** and **b** axes as well as perpendicular to **ab** plane of the crystals. We qualitatively explain the angle dependence of TMR using the results of dHvA oscillations and Hall measurements. Finally, a summary of this thesis work has been presented in Chapter 7.

2

Experimental details

2.1 Sample preparation

The key feature of topology protected electronic phases of material is its well defined surface and bulk state, electronically distinct from each other. Delicate electronic properties in these types of materials have been found to exist in extremely clean samples, in absence of any undesirable microscopic factor. The polycrystalline sample of any material is composed of many individual grain, oriented in random fashion. The sizes of individual grains vary from nanometer to micrometers scale. As a consequence, polycrystalline phase can hinder the rich physics of these materials in several ways, unlike bulk single crystalline phase. Due to presence of multiple grains and their boundaries in a piece of polycrystalline sample, the surface and bulk state contribution are ill-defined in electronic transport phenomena. The grain boundary scattering drastically affects the dynamics of high mobility charge carriers in these materials. So, it is almost impossible to identify the unique electronic response. Due to extremely low effective mass of the

charge carriers, these materials show quantum oscillation in moderate magnetic field strength. The quantum oscillation, as mentioned in the earlier chapter, is a fine probe to determine the detail geometry and nature of the Fermi surface. The cyclotron orbit of the charge carriers is comparable to the grains size of polycrystalline sample. As a results, incomplete cyclotron orbit precludes the formation of Landau levels, which is responsible for quantum oscillation. In addition, these materials usually host complex and anisotropic Fermi surface, unlike to that observed in conventional metals. As a consequence, the transport properties are highly anisotropic with respect to the crystallographic directions, which have immense impact in technological applications. The grains in polycrystalline sample are randomly oriented. So, the concept of a crystallographic direction is not valid for a piece of material in polycrystalline phase. One gets a response in electronic transport, averaged over all the crystallographic directions. Form the above discussion, it is evident that high-quality single crystalline sample is necessary for the research on topological 3D Dirac semimetal. All the high purity (at least 3N) chemical elements, which have been used for the sample preparation, are obtained from Alfa-Aesar and Sigma-Aldrich. Single crystals of all the studied materials were grown by chemical vapor transport technique. Details of sample preparation will be discussed in the respective chapters.

2.1.1 Chemical vapor transport technique

A condensed phase has an insufficient pressure for its own volatilization. Chemical vapour transport (CVT) is a process where a condensed phase, typically a solid is volatilised in presence of a gaseous reactant (known as 'transport agent')

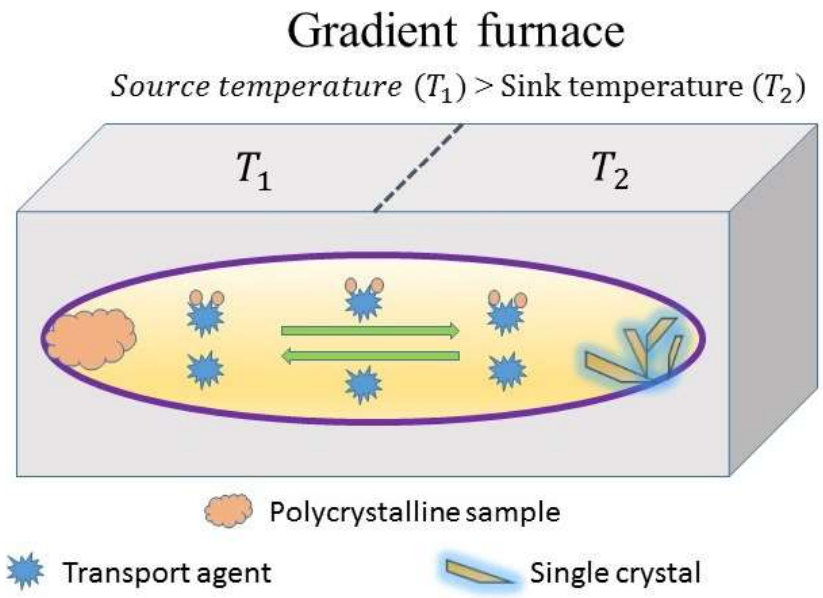

Figure 2.1: Schematic of experimental set-up for chemical vapor transport.

and deposited elsewhere in the form of crystals. The deposition will take place if there are different external conditions for the chemical equilibrium at the position of crystallization (sink) than at the position of volatilization (source). Usually, different temperatures are applied for volatilization and crystallization in a CVT. The various parameters that must be optimised for a successful CVT are growth temperature, transport direction, rate of the mass transport, choice of the transport agent and the free energy of the reaction. Typical transport agents include halogens and halogen compounds such as iodine, bromine, and potassium iodide. The set-up consists of a 2-zone or 3-zone furnace, reactant, and a transport agent. The reactant and transport agent are sealed in an ampoule (such as, quartz tube, tantalum tube) under high vacuum ($\sim 10^{-5}$ Torr). The schematic of experimental set-up and microscopic mechanism have been shown in Figure 2.1. The source end of the ampoule containing the precursor must be maintained at an optimal

temperature (T_1), which is usually higher than the sink end temperature (T_2). The temperature difference between the source and sink has to be optimized for the growth of high quality single crystals at the sink end. Depending on the free energy of the reaction between the species, the source and sink temperature will be adjusted.

2.2 Characterization

We determined the phase purity, structural details, crystalline nature, and chemical stoichiometry of the crystals using x-ray diffraction (XRD) and transmission electron microscope (TEM). Structural and phase purity analysis were done by high-resolution XRD of the powdered sample using Rietveld profile refinement. To confirm crystalline nature and chemical stoichiometry of grown samples, selected area diffraction (SAD), TEM image, and energy dispersive X-ray (EDX) measurements were done for some crystals, using high-resolution transmission electron microscopy (HRTEM).

2.2.1 Powder x-ray diffraction

Powder x-ray diffraction (XRD) is perhaps the most widely used technique for the characterization of materials. The term powder means that the crystalline domains are randomly oriented in the sample. When the atom is exposed to a monochromatic beam of x-rays, the x-ray photons collide with electrons and as a result some photons will be deflected away from their original direction. If

the wavelength of these scattered x-rays does not change, the process is called elastic scattering. In diffraction experiments, we measured the scattered x-rays as they carry the information about the electron distribution in the materials. Although the individual atoms scatter radiation in all directions, there are only a few directions in which the scattered waves interfere constructively and sharp interference maxima (peaks) with the same symmetry as in the distribution of atoms are observed in solids. The peaks in an XRD pattern are directly related to the atomic distances. Let us consider an incident x-ray beam interacting with the atoms arranged in a periodic manner [Figure 2.2]. The atoms can be viewed as forming different sets of lattice planes which are represented by the Miller indices (hkl). For a given set of (hkl) planes with an inter-plane distance of d_{hkl}, the condition for diffraction [4] is

$$2dsin\theta = n\lambda. \tag{2.1}$$

This is known as Bragg's law. Here θ is angle between incident beam and lattice plane, integer n is the order of diffraction, and λ is the wavelength of x-ray. The diffraction data can be collected either in transmission or in reflection mode. As the particles in the powder sample are randomly oriented, these two methods yield the same data.

Powder XRD patterns of the studied samples were taken by means of a RIGAKU diffractometer (TTRAX III) with a rotating anode, operating at 9 kW using Cu K_α radiation. Samples for powder XRD were prepared by grinding the crystals and pressed on a glass holder to achieve a smooth flat surface. The patterns were recorded in a range of 2θ between 10^0 and 90^0 at a step of 0.02^0. All the diffraction patterns were analyzed by a Rietveld method [43] using the FULLPROF program [44]. The crystal structure and lattice parameters of the samples were determined,

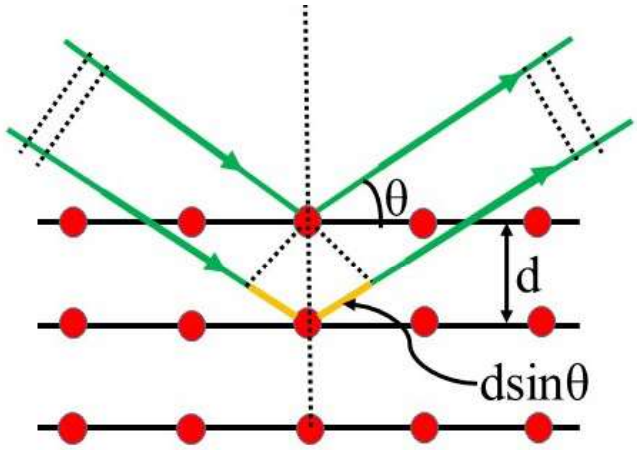

Figure 2.2: Schematic diagram of x-ray diffraction by crystallographic planes.

and the absence of any impurity phase was verified.

2.2.2 Transmission electron microscope (TEM)

In general, microscope is an instrument used for magnifying an object too small to see with the naked eye. The smallest distance between two points that we can resolve with our eyes is about 0.1-0.2 mm. This distance is the resolution or the resolving power of our eyes. So any instrument that can show us images revealing details finer than 0.1 mm could be considered as a microscope, and its highest useful magnification will be determined by its resolution. Visible-light microscope (VLM) is the most widely spread and familiar type of microscope where photon is used to magnify an object. The smallest distance (δ) that can be resolved by a VLM is determined by Rayleigh criterion, and is given approximately by $\delta = \frac{0.61\lambda}{\mu sin\beta}$. Here, λ is the wavelength of the radiation, μ is the refractive index of the viewing medium, and β is the semi-angle of collection of the magnifying lens [45]. The

term $\mu sin\beta$, which is known as numerical aperture, can be approximated to unity and as a consequence, the resolution is equal to about half the wavelength of light. For green light in the middle of the visible spectrum, λ is about 550 nm, and so the resolution of a good VLM is about 300 nm. Although 300 nm appears to be a small dimension to us, it corresponds to about 1000 atom diameters. So, many features that control the properties of materials are on a scale, well below the resolution of a VLM.

TEM works on the principle similar to that of an optical microscope with the key difference that it uses electrons and not photons as the source. The main motivation for developing a transmission electron microscope is that, since electrons are smaller than atoms, it should be possible to build a microscope, by which one can see the details below the atomic level. In TEM, the resolution (δ) is given by the expression, $\delta = \frac{1.22\lambda}{\beta}$ [45]. Louis de Broglie's famous equation shows that the wavelength of electrons is related to their energy, E, by the expression, $\lambda = \frac{1.22}{E^{1/2}}$. So, higher the energy, lower the de Broglie wavelength of electrons, and as a consequence, the resolution of a TEM will be higher. Using the above expression, one can work out that for a 100 keV electron, λ is $\sim$ 4 pm (0.004 nm), which is much smaller than the diameter of an atom. This resolution can now be used to probe the details in atomic and subatomic scale. During TEM analysis, a thin sample is bathed with a collimated beam of accelerating electrons, uniformly over the illuminated area. Electrons being charged in nature, can be easily deflected using an external electric or magnetic field and can be accelerated using external potential. A simplified diagram of a transmission electron microscope is given in Figure 2.3(a). As the electrons travel through the sample, they are either scattered

or are transmitted through the sample. The probability of scattering is described in terms of the interaction cross-section or the mean free path and can be elastic or inelastic. This results in nonuniform distribution of electrons in the beam that comes out of the sample, which contains all the structural information of the sample [45]. Figure 2.3(b) shows different types of scattered and transmitted electrons, and x-ray radiation, which are used to probe different microscopic features of a sample.

The scattered (diffracted) electrons deflected away from the optical axis of the

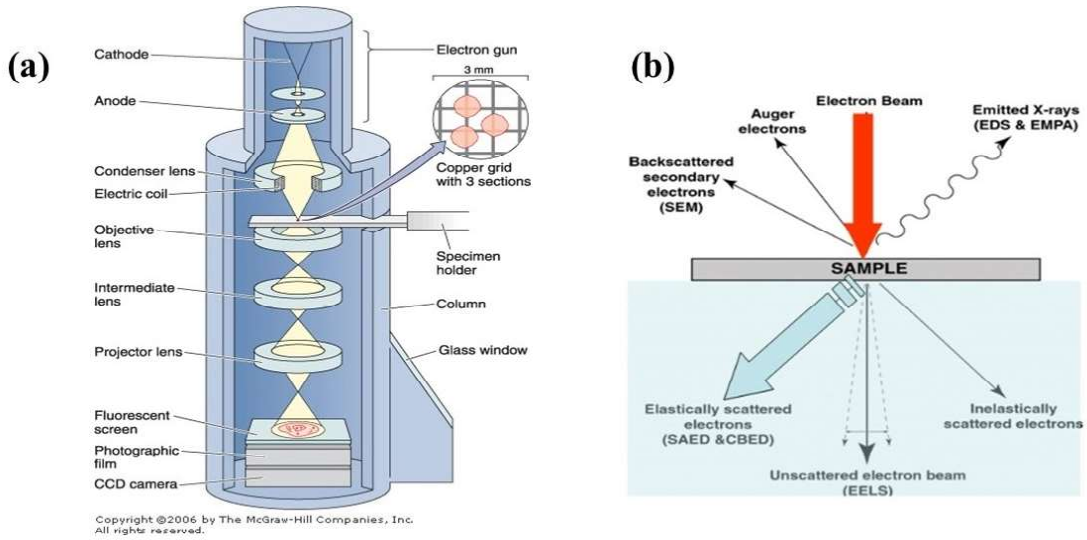

Figure 2.3: (a) Simplified diagram of a transmission electron microscope. (b)A schematic diagram showing different types scattered and transmitted electrons, and emitted x-ray, which are produced by the interaction of electron beam and sample.

microscope are blocked using an aperture and thus the transmitted electron beam generates a contrast on the fluorescent screen depending on its varying intensity. The intensity of the diffraction depends on the orientation of the planes of atom in the crystal relative to the electron beam. Angular distribution of electrons due to

diffraction can be viewed in the form of scattering patterns, usually called diffraction patterns, and spatial distribution of electrons can be observed as contrast in images of the sample. The transmitted electron beam strikes the fluorescent screen and generates an image with varying contrast. The darker areas with higher contrast are those from where fewer electrons have been transmitted due to high density or thickness of the sample while the areas of lower contrast show the areas in the sample, which have less density or thickness, and thus more number of transmitted electrons are present. HRTEM measurements of the crystals were done with a FEI TECNAI G^2 F30 S-TWIN microscope operating at 300 kV and equipped with a GATAN Orius SC1000B CCD camera.

2.3 Physical and magnetic properties measurements

2.3.1 Electrical resistivity

The dc/ac electrical resistivity of the samples was measured by standard four-probe technique [46, 47]. Four ohmic contacts were made on plate-like or niddle-like crystals, using thin gold wires ($\sim$ 50 μm diameter) and silver paint or silver epoxy paste. These four wires act as voltage and current terminals, in which current is allowed to flow between two outer probes and voltage is measured between two inner probes. The four contact regions are coated by silver paint and the contacts were made at room temperature. The dc resistivity was measured as a function of temperature from 300 K to 2 K, and as a function of applied magnetic field up to 9 tesla in a variable temperature insert (VTI) of a cryogen free measurement system (CFMS, Cryogenic Ltd.). The ac resistivity was measured for the same temperature and magnetic field range at 13.7 Hz in a 9 tesla physical property

measurement system (PPMS, Quantum Design). Typical values of current for the resistivity measurements were about 5 mA.

To measure the dc resistivity a constant dc current of appropriate level was sent through the sample from a Keithley 224 current source and the voltage across the sample's voltage leads was measured by using a Keithley 2182A nanovoltmeter with current flowing in the forward and reverse direction to eliminate the contributions of thermoelectric effect and offset voltage of the nanovoltmeter. The sample temperature was measured using a calibrated Cernox (ceramic-oxynitride) sensor and temperature was controlled using a Lake Shore temperature controller (Model 340). The signals from the voltage probes, Cernox temperature sensor, and magnet power supply of VTI are recorded by a Labview software program on the computer to get the temperature and magnetic field dependence of the resistance (R) of the samples.

The ac resistivity was measured using the ac transport measurement option of physical property measurement system. The ac resistivity was measured for the samples which are highly conducting as the quality of the data are better than that of dc resistivity. A constant sinusoidal current of appropriate amplitude and of frequency 13.7 Hz was allowed to flow through the current leads and the ac voltage across the sample's voltage leads was measured and amplified by a lock-in amplifier. The resistance of the samples was recorded as a function of temperature and magnetic field by PPMS Multiview software on the computer.

The resistivity (ρ) of the sample has been estimated from the formula:

$$\rho = R\frac{A}{l}, \tag{2.2}$$

where A is the cross sectional area and l is the separation between two voltage

leads. It should be mentioned that there is some degree of ambiguity as to the appropriate cross sectional area, as the value will depend on the precise path of the current through the sample. It has been assumed that the current flows uniformly throughout the width of the sample.

2.3.2 Seebeck coefficient

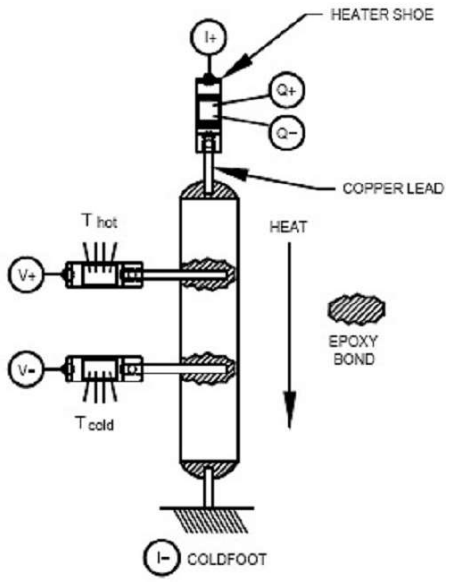

Figure 2.4: Schematic diagram of thermal and electrical connections to the sample with heater and sensors. T_{hot} and T_{cold} are the temperatures of two Cernox chip thermometers, V+ and V- are the two voltage leads, I+ and I- are the current leads and Q representing the heater terminal. Reproduced from Ref.[48].

The Seebeck coefficient and thermal conductivity measurements were carried out in the Physical Property Measurement System using its Thermal Transport Option (TTO) [48]. TTO uses a 2 kOhm metal chip resistor as a heater and Cernox thermometer for measuring temperatures of the hot and cold ends of the sample. These commercial Cernox thermometers are excellent for use in high magnetic

field. Typical errors in temperature [ΔT/T] due to magnetic field, are -0.15% at 4.2 K, 0.022% at 77 K, and very small at higher temperature and 8 T field. The high vacuum option of TTO reduces the heat leak due to thermal convection. The TTO option also estimates the radiation loss at different temperatures based on the sample dimensions and emissivity as inputs and takes this loss into account while estimating thermal conductivity. We employed standard four-probe mounting technique as shown in Figure 2.4. Four oxygen-free high-conducting gold coated Cu leads are glued to the sample with conducting silver epoxy for good thermal anchoring. The opposite ends of the leads are then attached to the heater and temperature sensors. Before measurements on the single crystal sample, TTO were calibrated using standard Ni 201 alloy for the experimental range of temperature from 350 to 1.9 K and magnetic field up to 9 T.

2.3.3 dc magnetization

To study the de Hass-van Alphen oscillation, the magnetic field dependence of dc magnetization was measured in Superconducting Quantum Interference Device (SQUID) magnetometers viz., MPMS 3 (SQUID VSM) equipped with 7 T superconducting magnet. This section describes the measurement of the dc magnetization by MPMS 3 SQUID VSM magnetometer which has the magnetization sensitivity of 5×10^{-8} emu and can operate in the temperature range 1.8 K to 400 K with a maximum temperature sweep rate of 50 K/min and fields up to $\pm$7 T with a maximum field sweep rate of 700 Oe/sec. Figure 2.5 illustrates a simplified model of the MPMS SQUID VSM detection system [49]. The superconducting detection coils are configured as a second-order gradiometer, with counter-wound

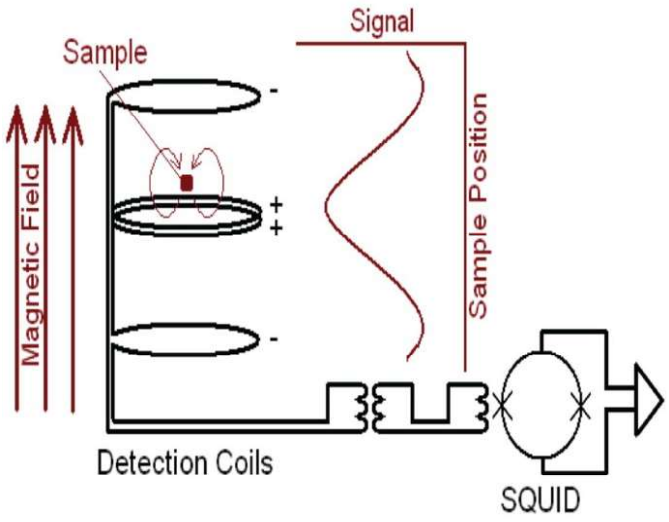

Figure 2.5: A simplified schematic diagram of SQUID VSM detection system. Figure reproduced from Ref.[49].

outer loops which make the set of coils non-responsive to uniform magnetic fields and linear magnetic field gradients. The detection coils only generate a current in response to local magnetic field disturbances due to the vibrating magnetic sample. If sample dimensions are much smaller than the dimensions of the detection coils, the current in the detection coils is a function of the sample position. The current in the detection coils is inductively coupled to the instrument's SQUID, which serves as an extremely sensitive current-to-voltage converter. The SQUID function is based on the two phenomena viz., flux quantization in a superconducting ring and Josephson effect. The Josephson effect refers to the phenomenon of current flow across two weakly coupled superconductors, separated by a very thin insulating barrier. The SQUID feedback nulls the current in the detection coils so no current actually flows in them, and the feedback current yields the actual SQUID voltage that gives the sample magnetization value. The SQUID voltage is amplified and digitized by the instrument electronics.

Using the VSM linear motor system, the sample can be vibrated at frequency ω about the very center of the detection coils, where the signal peaks as a function of sample position, z. This generates a SQUID signal, V, as a function of time, t:

$$V(t) = AB^2 \sin^2(\omega t), \tag{2.3}$$

because $V(z) = Az^2$ for small vibration amplitudes, and $z(t) = B\ \sin(\omega t)$. Here, A is a scaling factor relating to the magnetic moment of the sample. B is the amplitude of sample vibration. Since $\sin^2(\omega t) = \frac{1}{2}$(1- $\cos(2\omega t)$) (by identity), a lock-in amplifier is used to isolate and quantify the signal occurring at frequency 2ω, which should be caused exclusively by the sample if the vibration frequency is selected properly. Briefly, this is achieved by multiplying the measured signal with a phase-corrected reference signal at 2ω and then extracting the dc component of the result. This dc component is proportional to the 2ω component of the measured signal. This technique quickly and precisely isolates the sample signal from other noise sources, including drifting SQUID signal and mechanical noise sources synchronized to the sample vibration. The lock-in amplification of the SQUID signal is performed by digital electronics in the SQUID control module.

3

Probing the Fermi surface of three-dimensional Dirac semimetal Cd_3As_2 through the de Haas-van Alphen technique

3.1 Introduction

After the discovery of 3D Dirac semimetal phase in Cd_3As_2, angle-resolved photoemission spectroscopy (ARPES) measurements have shown that two almost identical ellipsoidal Fermi surfaces are located on the opposite sides of the Γ point along the k_z direction [50, 51]. As real material is subject to uncontrolled doping during sample preparation, the Fermi energy in bulk single crystals can be as high as few hundreds of meV. With the increasing value of Fermi energy, the size of the Fermi surfaces also increase. Earlier, it was believed that these two Fermi surfaces merge

into a single ellipsoidal contour around the Γ point beyond the Lifshitz transition, where the two Fermi surfaces started to overlap each other [52]. However, first-principles calculations suggest that this transition should occur very close to the Fermi energy ∼133 meV and a complex mixing of Fermi surfaces is expected to happen [53]. This could be observed in quantum oscillation measurements, which has been established to be a useful tool to probe the Fermi surface of a material accurately. But, the analysis of Shubnikov-de Haas (SdH) oscillations indicates the existence of one or two equivalent Fermi surface cross sections corresponding to the single frequency of oscillation, and the Fermi energy of the single crystal sample has been reported to have much larger value than 133 meV [53, 54, 55, 56]. Under such circumstances, probing the Fermi surface (FS) of Cd_3As_2 using the de Haas-van Alphen (dHvA) oscillation, which has been established to be a more accurate technique due to absence of local heating and quantum interference effects or noise from the electrical contacts, may provide some finer details of the FS. In this chapter, along with the SdH oscillation and high nonsaturating linear magnetoresistance (MR), we report the observation of two different Fermi surface cross sections from the dHvA effect, which can be associated to the complex mixing of two identical Fermi surfaces above the Lifshitz transition. Furthermore, the dHvA effect also confirms the nontrivial Berry's phase (signature of 3D Dirac fermion) in Cd_3As_2.

3.2 Sample preparation, characterization, and experimental details

Single crystals of Cd_3As_2 were synthesized using the chemical vapor transport technique. First, we prepared polycrystalline Cd_3As_2 samples by heating the stoichiometric mixture of high-purity (5N) Cd pieces and As powder at 500°C for 8 h and at 850°C for 24 h in a vacuum-sealed quartz tube 15 cm long and 16 mm in diameter. The product was then heated again at 550°C for another 48 h for homogenization. Finally, the quartz tube was placed in a gradient furnace and heated for 48 h. During heating, the end of the quartz tube which contains the compound was maintained at 690°C, while the other end was kept at 600°C. The furnace was then cooled slowly to room temperature. Several small-size shiny plate-like crystals formed at the cold end of the tube were mechanically extracted for transport and magnetic measurements. Image of a representative piece of Cd_3As_2 single crystal is shown in Figure 3.1(a). Phase purity and the structural analysis of the samples were done using the high-resolution powder x-ray diffraction (XRD) technique with Cu-K_α radiation. Figure 3.1(b) shows the x-ray diffraction pattern of powdered sample of Cd_3As_2 single crystals at room temperature. Within the resolution of XRD, we did not see any peaks due to the impurity phase. Using the Rietveld profile refinement program of diffraction patterns, we calculated the lattice parameters a=b=12.644 Å and c=25.447 Å with space-group symmetry I_{41}/acd. The resistivity measurements of Cd_3As_2 single crystals were done using the standard four-probe technique. Electrical contacts were made using conductive silver paste (DuPont) or silver epoxy paste (EPO-TEK). The electrical and thermal transport measurements were carried out in a 9-T physical property measurement system

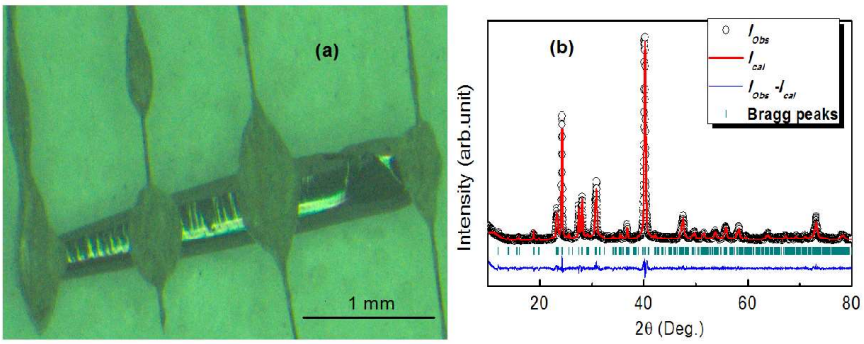

Figure 3.1: (a) Image of a representative piece of Cd_3As_2 single crystal with electrical contacts. (b) X-ray diffraction pattern of powdered single crystals of Cd_3As_2. Black, experimental data; red, the calculated pattern; blue, the difference between experimental and calculated intensities; green, the Bragg positions.

(Quantum Design). The magnetization was measured using a superconducting quantum interference device vibrating-sample magnetometer (Quantum Design).

3.3 Results and Discussions

Figure 3.2(a) shows the temperature dependence of the resistivity ρ_{xx} of a Cd_3As_2 single crystal. ρ_{xx} is metallic over the whole range of temperature. ρ_{xx} exhibits approximately $T^{1.3}$ dependence above 100 K and becomes almost T independent for T<20 K, which reveals a residual resistivity $\rho_{xx}(0) \sim 50$ $\mu\Omega$cm. Both the value and the nature of temperature dependence of resistivity are similar to those reported earlier [53, 54]. We have also measured the temperature dependence of resistivity for different other crystals of Cd_3As_2. For all the cases, we found almost similar T dependence of ρ_{xx} and comparable values of ρ_{xx}. This implies that the variation in the strength of disorder and doping from sample to sample is not significant in the present crystals. Figure 3.2(b) displays the field dependence of the magnetoresis-

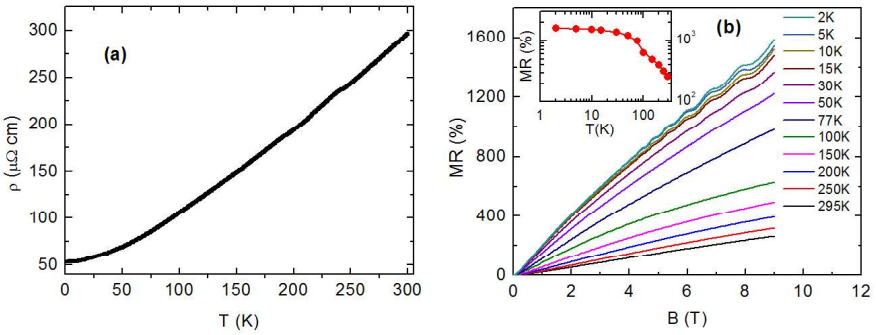

Figure 3.2: (a) Temperature dependence of the resistivity of Cd_3As_2 crystal. (b) Magnetic field dependence of magnetoresistance (MR) at various temperatures when the field was applied along the [100] direction. The inset shows the temperature dependence of MR at a field of 9 T.

tance at different temperatures. MR is defined as $[\rho_{xx}(B)$ - $\rho_{xx}(0)]/\rho_{xx}(0)$. Here, current and magnetic field are applied along the [012] and [100] directions of the crystal, respectively. We have followed the convention of Feng *et al.* for indexing the crystallographic directions [53]. Even at room temperature and 9 T magnetic field, MR shows no sign of saturation, and its value is as high as 263%. Except at low field, MR is approximately linear. Such a large linear MR at room temperature is quite unusual and needs further research to understand the microscopic origin. With decreasing temperature, MR increases rapidly, and reaches ∼1600% at 2 K and 9 T. In the inset of Figure 3.2(b), we have shown the temperature dependence of MR at 9 T in log-log scale. It is clear from the figure that, unlike conventional metal, MR is almost T-independent in the low-temperature region below 30 K. Similar behavior has also been observed in other crystals.

ΔR_{xx}, obtained after subtracting a smooth background from MR, is plotted in Figure 3.3(a) and Figure 3.3(b) as a function of $1/B$ for fields along $[02\bar{1}]$ and [100], respectively. The presence of SdH oscillations can be traced down to a field of ∼2 T and up to 50 K. With increasing temperature, the amplitude of oscilla-

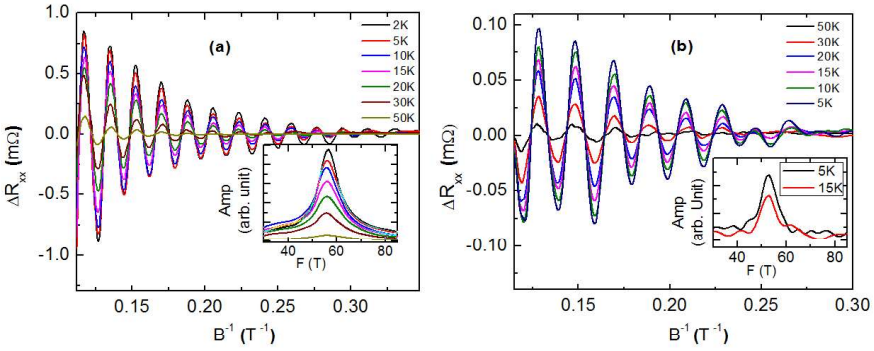

Figure 3.3: (a) The oscillatory component ΔR_{xx} of MR (after subtracting a smooth background) as a function of $1/B$ at various temperatures with magnetic field along the $[02\bar{1}]$ direction; the inset shows the oscillation frequency after fast Fourier transform. (b) ΔR_{xx} for magnetic field along the [100] direction; the inset shows the corresponding frequency.

tion decreases rapidly. The fast Fourier transform spectrum of ΔR_{xx} versus $1/B$ curve show a single oscillation frequency at around 56 T [inset of Figure 3.3(a)] and 53 T [inset of Figure 3.3(b)] for the field along $[02\bar{1}]$ and [100], respectively. According to the Onsager relation $F{=}(\phi_0/2\pi^2)A_F$, the cross-sectional areas of the Fermi surface normal to the field directions are $A_F{=}5.32{\times}10^{-3}$ and 5.04×10^{-3} Å^{-2}. Assuming a circular cross section, a small Fermi momentum $k_F \sim 0.04$ Å^{-1} is calculated. The presence of single frequency and the value of A_F are in good agreement with that obtained in earlier SdH oscillation experiments [54, 56].

The magnetization of Cd_3As_2 crystal has been measured at different temperatures with B parallel to the [100] direction, which displays a very clear dHvA effect [Figure 3.4(a)]. We have been able to observe the oscillations down to 1 T and up to 50 K. This indicates that the quantization of the electron orbit does not get blurred by collisions with phonon or any impurity due to the high mobility of the charge carriers. In Figure 3.4(b), the magnetic susceptibility $\Delta\chi$ $(= dM/dB)$ versus $1/B$ plot shows how the oscillation amplitude decreases with increasing temperature.

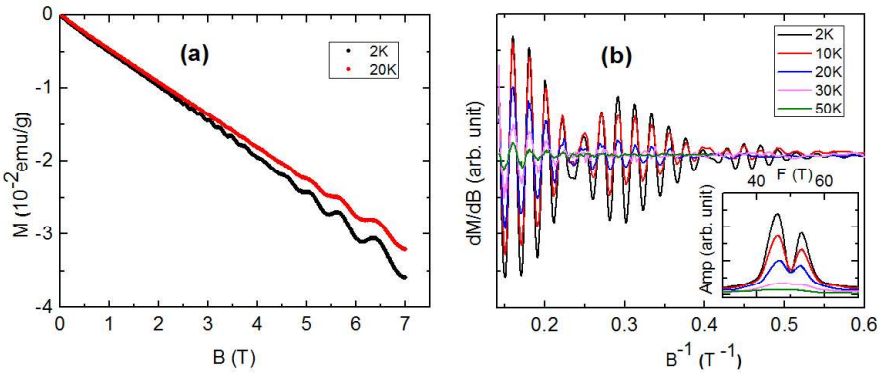

Figure 3.4: (a) Magnetic field (along the [100] direction) dependence of the diamagnetic moment at temperature of 2 and 20 K. (b) Oscillating part of the susceptibility $\Delta\chi = d(M)/dB$ versus $1/B$; de Haas-van Alphen (dHvA) effect. The inset shows the oscillation frequency after the fast Fourier transform is found from the dHvA effect.

The inset of Figure 3.4(b) shows the oscillation frequency obtained by the Fourier transformation of the dM/dB curve. Unlike magnetoresistance data, we observe two distinct oscillation frequencies: one at 46 T and the other at 53 T. This reveals two cross-sectional areas of the Fermi surface perpendicular to B, 4.39×10^{-3} and 5.04×10^{-3} Å^{-2} respectively.

To understand the phenomenon, we have performed magnetization measurements with the field along the $[02\bar{1}]$ direction as shown in Figure 3.5(a). But the dHvA oscillation along this direction gives only one frequency which is close to the frequency determined from the SdH oscillation along that direction. Although the dHvA oscillation along the $[02\bar{1}]$ direction establishes the equivalence between two ellipsoidal Fermi surfaces found in ARPES [51] or a single ellipsoidal contour after Lifshitz transition, the magnetization measurement along the [100] direction indicates two Fermi surface cross sections corresponding to two different frequencies. Also, we have carried out magnetization measurements by applying magnetic field

perpendicular to both [02$\bar{1}$] and [100], i.e., along the [012] direction. Similar to [02$\bar{1}$] direction, the dHvA oscillations for B |||[012] reveal a single frequency peak at 46.5 T, as shown in Figure 3.5(b). The above observations suggest that two equivalent cross sections from two ellipsoidal Fermi surfaces superpose with each other along certain directions, leading to two frequencies of oscillation in the dHvA effect. This has been schematically illustrated in Figure 3.5(c). It shows that the magnetic field along [02$\bar{1}$] and [012] directions generate pair of extremal cyclotron orbits with identical areas. Whereas, the two Fermi surface cross sections for B |||[100] overlap with each other, which can lead to two frequencies of oscillations due to complex mixing of cyclotron orbits. The presence of two frequency peaks along certain crystallographic directions has been confirmed through SdH oscillation study under high magnetic fields, where the authors have also argued that the Fermi surface of Cd_3As_2 consists of two nested ellipsoids beyond the Lifshitz saddle point [57]. As 3D Dirac semimetals have a well-defined surface state, another possible explanation for the occurrence of two frequencies may be the contribution from surface and bulk states. From theory, it has been clearly shown that the surface state contribution can play a considerable role only when the sample is few nm thin [55]. However, thickness of the present Cd_3As_2 single crystal is ~0.4 mm, which seems to be much larger than the critical thickness and eliminate the possibility of quantum oscillation from surface states.

The temperature and field dependence of SdH oscillations in a real material is well-described by the Lifshitz-Kosevich (LK) formula [58, 59]:

$$\Delta R_{xx} \propto \frac{\frac{2\pi^2 k_B T}{\hbar\omega_c}}{\sinh(\frac{2\pi^2 k_B T}{\hbar\omega_c})} \times exp(-\frac{2\pi^2 k_B T_D}{\hbar\omega_c}) \times cos2\pi(\frac{F}{B} + \frac{1}{2} - \beta + \delta), \qquad (3.1)$$

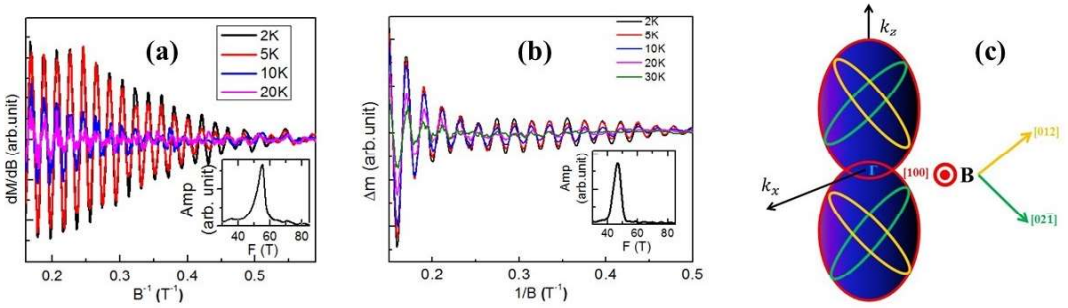

Figure 3.5: (a) Oscillating part of susceptibility $\Delta\chi = d(M)/dB$ vs $1/B$ (dHvA effect) for magnetic field along the [02$\bar{1}$] direction; the inset shows oscillation frequency at 55.20 T after the fast Fourier transformation. (b) Oscillating part of magnetization $\triangle m$ vs $1/B$ (dHvA effect) for magnetic field along the [012] direction; the inset shows the frequency of oscillation after fast Fourier transform found from dHvA effect. (c) Schematic diagram of the possible nested Fermi surface above the Lifshitz transition, and the Fermi surface cross-sections along different crystallographic directions.

where ΔR_{xx} and $\hbar\omega_c$ are the oscillating part of resistivity and energy gap between two successive Landau levels, respectively. In the above equation, the first and the second term are the thermal damping (R_T) and Dingle (R_D) factors of quantum oscillations, respectively. The cosine term at the end is the phase term of the oscillations, where $2\pi\beta$ and $2\pi\delta$ are the Berry's phase and an additional phase associated to dimensionality, respectively. Here, β can take values from 0 to 1/2 (0 for parabolic dispersion as in the case of conventional metals and 1/2 for the Dirac system), and δ can change from 0 for a quasi-two-dimensional cylindrical Fermi surface to $\pm 1/8$ for a corrugated 3D Fermi surface [54, 58]. Similar to SdH oscillations, the dHvA oscillations can also be described by the Lifshitz-Kosevich formula. Although, for a Dirac system, the linear spectrum implies zero rest mass of the charge carriers and gives the Landau energy level $E_n = v_F\sqrt{(2n\hbar eB)}$, the cyclotron mass of the carriers is not zero [60, 61]. So the above-mentioned LK for-

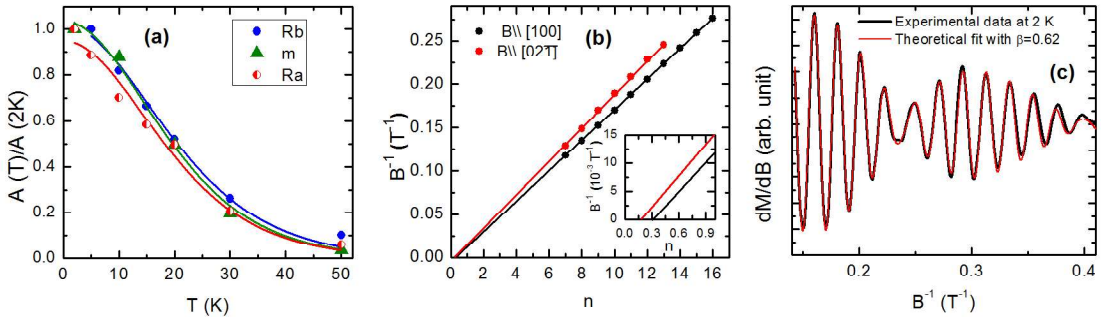

Figure 3.6: (a) Temperature dependence of the relative amplitude of quantum oscillation for the ninth Landau level, where *Ra* and *Rb* are the oscillation amplitudes in the SdH oscillation for $B\|[02\bar{1}]$ and $B\|[100]$, respectively, and m corresponds to the oscillation amplitudes in $\Delta\chi$ for $B\|[100]$. The solid line is a fit to the thermal damping term (R_T) of Lifshitz-Kosevich formula [Equation 3.1]. (b) Landau index n plotted against $1/B$ (Solid circles denote the peak positions) from the SdH oscillations. Solid lines are the linear fit to the experimental data points. From the linear extrapolation of the fitted lines, as shown in the inset, the obtained values of **x**-axis intercept are ~ 0.20 and ~ 0.32 for $B \parallel [100]$ and $B \parallel [02\bar{1}]$, respectively. (c) Theoretical fitting to the $\Delta\chi(1/B)$ for $B\|[100]$ by the two-band LK formula, at representative temperature 2 K.

mula with $\omega_c = eB/m_c^\star$ is a widely accepted expression for analyzing the quantum oscillation amplitude in Dirac-type electronic systems [60, 61]. Here, $m_c^\star$ is the effective cyclotron mass of the charge carrier and the Fermi velocity $v_F{=}\hbar k_F/m_c^\star$.

In Figure 3.6(a), we have plotted the normalized amplitude of oscillation with increasing temperature for given oscillation peaks, for both the SdH and dHvA oscillations. The decay of oscillation amplitudes with increasing temperature has been fitted with the thermal damping term, R_T, of Lifshitz-Kosevich formula. From the obtained values of fitting parameters for the SdH oscillations, we deduced $m^\star$ $\sim 0.045m_e$ for $B \|[100]$ and $\sim 0.05m_e$ for $B \|[02\bar{1}]$ configurations. The values of v_F for $B \|[100]$ and $B \|[02\bar{1}]$ are $\sim 1.03{\times}10^6$ m/s and $\sim 0.96{\times}10^6$ m/s, respectively. From the similar analysis of dHvA oscillations for $B \|[100]$, the values of v_F and $m_c^\star$ are determined to be $\sim 1.04\times 10^6$m/s and $\sim 0.044m_e$, respectively,

considering the frequency peak at 53 T. Thus, the calculated values of v_F and $m_c^\star$ from transport and magnetization data are close to each other. These values are also close to those reported by different groups [53, 54, 55, 56]. Now, using the Fermi momentum and Fermi velocity, we have deduced the Fermi energy (E_F), which is $\sim$ 270 meV. So, we are well-above the Lifshitz transition point, predicted in earlier works [52, 53]. By fitting the SdH oscillation amplitude with magnetic field to $\exp(-2\pi^2 k_B T_D/\hbar\omega_c)$, we have deduced the Dingle temperature T_D=16.8 K. To get a quantitative estimate about the mobility of the charge carriers in the system, we have calculated the quantum mobility (μ_q) $\sim$ 3.2 $\times 10^3$ cm^2 V^{-1} s^{-1} using the expression, $\mu_q = (e\hbar/2\pi k_B m^* T_D)$. The quantum mobility in a system is always lower than the classical Drude mobility (μ_c), as μ_q is sensitive to both large and small angle scattering, while μ_c is sensitive to only large angle scattering.

In Figure 3.6(b), we have plotted the index of the Landau levels with its position ($1/B$), which is known as Landau level index plot. The integer index n, corresponding to the peaks in SdH oscillations, are assigned in such a way that a linear extrapolation of the straight line yields an intercept closest to the zero. From the plot, we have found that the value of magnetic field at n=1 is $\sim$ 50 T, above which the system will be at the quantum limit (n=0). The deduced value of the critical field is very close to that observed in quantum limit magnetotransport experiments under high magnetic fields [57, 62]. The cosine term Equation 3.1, provides the Lifshitz-Onsager quantization rule, which states $A_F(\hbar/eB) = 2\pi(n + \frac{1}{2} - \beta + \delta)$, when n is assigned to the peak positions in the oscillation in resistivity [54, 58]. As the value of β is $\frac{1}{2}$ for Dirac type electronic system with an additional phase shift δ in three dimensions, the ideal value of **x**-axis intercept in the index plot is

$0\pm1/8$ [58]. From the linear extrapolation of the index plot in the SdH oscillation with B along [100]([02$\bar{1}$]) direction, the obtained value of intercept is ~ 0.20 (0.32), which reflects the Dirac semimetal state in Cd_3As_2. Since the intercept has been obtained by fitting a set of data points obtained for much higher values of n, we have estimated the errors in the values of intercepts. It has been found that, the difference in the values of intercept from linear fit to 50% of data points at lower n side, and from the linear fit to 50% of data points at high n side, is no more than 0.05. As there are two distinct frequency peaks in dHvA oscillations for B ||[100], the actual peak positions in $\Delta\chi$ may not be same as the peak positions in Figure 3.4(b), due to interference between two oscillations of different frequencies. To determine the Berry's phase from dHvA oscillations, we have fitted the $d(M)/dB$ vs $1/B$ plot for B ||[100] direction, with the superposition of two LK equations for the two frequencies 46 T and 53 T [Figure 3.6(c)]. In the expression, $\frac{dM}{dB} = \frac{A_1}{B^{3/2}} exp(-\frac{2\pi^2 k_B T_D}{\hbar\omega_c}) \times cos2\pi(\frac{F_1}{B}+\frac{1}{2}-\beta+\delta) + \frac{A_2}{B^{3/2}} exp(-\frac{2\pi^2 k_B T_D}{\hbar\omega_c}) \times cos2\pi(\frac{F_2}{B}+\frac{1}{2}-\beta+\delta)$, we have ignored the thermal damping term [59]. This is because it is a very slowly varying function of B, compared to the other terms. The theoretical fit provides the value of Berry's phase $[2\pi\beta] \sim 1.24\pi$. This value is within the range $2\pi[\frac{1}{2}\pm\frac{1}{8}]$ for 3D Dirac fermion, but far away from the value 0 for Schrodinger fermion. Due to presence of single frequency in dHvA oscillations in other experimental configurations, we have determined the Berry's phase from Landau level index plots, which is also found to be close to the above-mentioned value. Slightly higher value of the intercept in previous technique, from the prescribed range, may be due to poor resolution of SdH oscillations compared to the dHvA oscillations.

3.4 Conclusion

In conclusion, we have studied dHvA and SdH oscillations as two parallel methods to probe the Fermi surface of Cd_3As_2, and the values of the Fermi wave vector, Fermi velocity, and effective cyclotron mass of the charge carrier have been calculated from both the techniques. The dHvA effect reveals two distinct frequencies of oscillations 46 and 53 T along [100], and single frequency along $[02\bar{1}]$ and [012]. This observation confirms the existence of two Fermi surface cross sections along certain directions. Both the transport (SdH) and magnetic (dHvA) measurements reveal a nontrivial π Berry's phase, which is the signature of the existence of 3D Dirac semimetal phase in Cd_3As_2.

4

Tuning the scattering mechanism in three-dimensional Dirac semimetal Cd_3As_2

4.1 Introduction

After the discovery of Dirac fermionic excitations in Cd_3As_2, major attention has been focused on the electronic transport properties for understanding the nature and origin of ultrahigh magnetoresistance, mobility of charge carriers, and the Fermi surface (FS) geometry [53, 54, 56, 57, 62, 63, 64]. It has been predicted theoretically [27, 28] that the breaking of time reversal symmetry by external magnetic field rearranges the Fermi surface of Cd_3As_2. From the magnetoresistivity and Hall measurements, a strong field dependence of scattering time has been observed and this behavior has been ascribed to the field-induced changes in the Fermi surface [56]. In this context, we would like to focus on some im-

portant differences between the FS proposed from angle-resolved photoemission spectroscopy (ARPES) and quantum oscillation measurements. ARPES results show that Cd_3As_2 hosts two ellipsoidal FS with negligible anisotropy, i.e, two almost spherical FS [37, 51]. A 3D plot of spectra intensity clearly shows linear dispersion with little anisotropy along two perpendicular directions in [111] plane [37]. Whereas the Shubnikov-de Haas (SdH) [57, 62, 65] and de Haas-van Alphen (dHvA) [64] oscillations reveal anisotropic FS with different frequencies, Fermi velocities and carrier effective mass. Furthermore, no surface experiment has been able to detect the Lifshitz transition in Cd_3As_2 [37, 51]. On the other hand, the Lifshitz transition and, as a consequence, the FS nesting has been detected both from the SdH oscillation [57, 66] and dHvA effect [64] well below 300 meV, which is consistent with the theoretical predication. Band structure calculations show that this transition is expected to occur at around $\sim$133 meV [53]. As quantum oscillations are observed in presence of high magnetic field, the associated features from this kind of study may arise as a result of reconstruction of the FS by magnetic field. So, it is worthwhile to study how this change in the Fermi surface is reflected in the scattering of charge carriers and which relaxation process dominates the charge transport at high magnetic field. Doping also affects the Fermi surface by either reducing or enlarging its area. Thus, it is important to study the effect of doping and magnetic field simultaneously on the charge transport mechanism. The measurement of resistivity alone is not sufficient to understand the details of the scattering mechanism. Thermoelectric power (S) has been used as a powerful tool to probe the relaxation process in metals and semiconductors because it provides complementary information to resistivity due to its proportionality with the energy-derivative of the electrical conductivity. Indeed, the inverse square-root

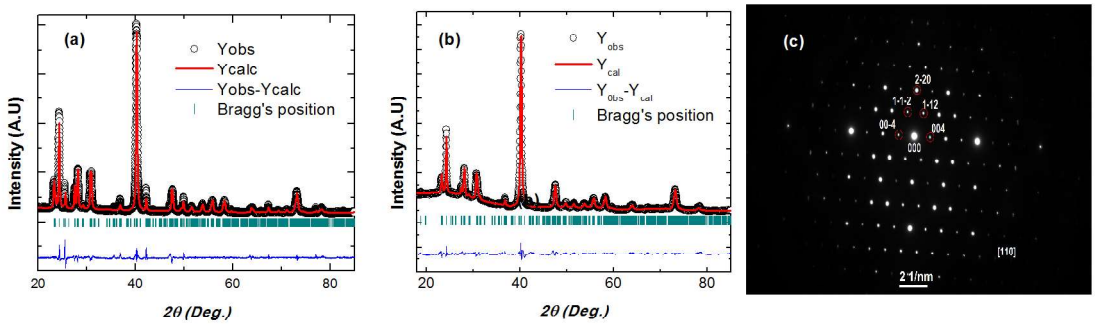

Figure 4.1: (a) X-ray diffraction pattern of powdered single crystals of $(Cd_{0.98}In_{0.02})_3As_2$. Black ($Y_{obs}$), experimental data; red (Y_{cal}), the calculated pattern; blue (Y_{obs}-Y_{cal}), the difference between experimental and calculated intensities; green, the Bragg positions. (b) X-ray diffraction pattern of powdered single crystals of $(Cd_{0.96}In_{0.04})_3As_2$. (c) Selective area electron diffraction (SAD) pattern obtained through HRTEM measurement for $(Cd_{0.98}In_{0.02})_3As_2$.

dependence of the thermoelectric power on carrier density clearly reflects the linear dispersion relation in graphene which is the fingerprint of massless Dirac fermions [67]. In this work, we present a thorough study on thermoelectric properties of Cd_3As_2 to probe the possible scattering mechanisms. We have shown that the relaxation process can be widely tuned upon carrier doping and by applying external magnetic field, which is a step forward towards understanding the material.

4.2 Sample preparation, characterization, and experimental details

Single crystals of Cd_3As_2 were synthesized by chemical vapor transport technique. The details of sample preparation and characterization have been described in previous chapter. As the ionic radii of cadmium and indium are close to each

other, we choose to dope In at Cd site in Cd_3As_2 to minimize the doping induced lattice disorder. Single crystals of $(Cd_{1-x}In_x)_3As_2$ with x=0.02 and 0.04 were prepared using the same technique as that for the undoped one. Phase purity and the structural analysis of the samples were done using the high-resolution powder x-ray diffraction (XRD) technique with Cu-K_α radiation. Figure 4.1(a) and Figure 4.1(b) show the room-temperature x-ray diffraction pattern for the powdered samples of single crystals with x=0.02 and 0.04, respectively. Within the resolution of XRD, we have not observed any peak due to the impurity phase as a result of In doping. Using the Rietveld profile refinement program for the diffraction patterns, we have calculated the lattice parameters a=b=12.643 Å and c=25.440 Å for x=0.02 while a=b=12.663 Å and c=25.466 Å for x=0.04 with space-group symmetry I_{41}/acd. These values of lattice parameters are very close to that for Cd_3As_2 [64]. Selected area electron diffraction for the doped single crystal has been done using the high resolution transmission electron microscopy. Figure 4.1(c) shows the SAD pattern for the x=0.02 crystal. Very clear periodic diffraction spots in the SAD pattern implies well-stacked crystal planes and absence of any crystal defects in the doped compound. The thermoelectric power (Seebeck coefficient) and magneto-transport measurements on undoped and doped Cd_3As_2 single crystals were done by four-probe technique using thermal and ac transport measurement options, respectively, in physical property measurement system (Quantum Design). The typical dimensions of the undoped, 2% In-doped and 4% In-doped samples, used in both the thermopower and transport measurements, are $\sim$3×2×0.55 mm^3, $\sim$3×1.5×0.6 mm^3 and $\sim$3.5×1.5×0.25 mm^3, respectively. All the measurements were carried out by applying magnetic field along [100] direction. Both the current and temperature gradient are along [012] direction; perpendicular to the applied

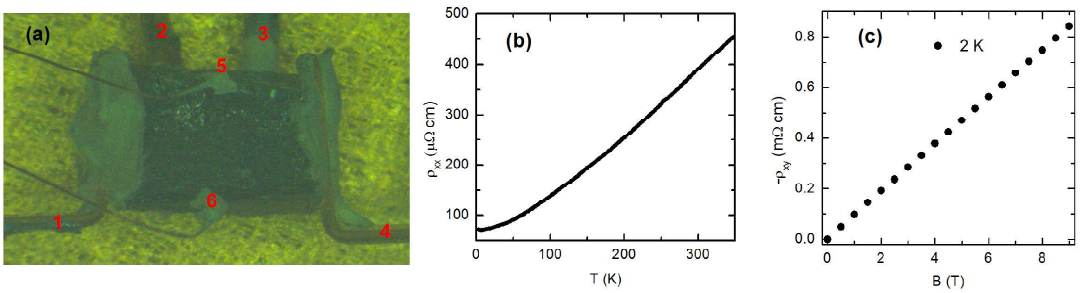

Figure 4.2: (a) A representative image of electrical and thermal contacts on a piece of Cd_3As_2 single crystal. 1, 2, 3, and 4 are the terminals for electrical resistivity and thermopower measurements. 5 and 6 are the voltage terminals in Hall resistivity measurements. (b) Temperature dependence of resistivity (ρ_{xx}) of Cd_3As_2 single crystal from 2 to 350 K. (c) The field dependence of the Hall resistance at 2 K.

magnetic field. Though several single crystals have been studied, we present the data for one single crystal as a representative for each composition. Qualitatively similar behavior has been observed for other crystals.

4.3 Results and Discussions

4.3.1 Resistivity and Hall resistance of Cd_3As_2 single crystal

Figure 4.2(a) shows the contact configuration on a piece of Cd_3As_2 single crystal for electronic transport and thermopower measurements. The temperature dependence of resistivity (ρ_{xx}) for a Cd_3As_2 single crystal is shown in Figure 4.2(b). Over the entire temperature range from 350 to 2 K, ρ_{xx} exhibits metallic behavior ($d\rho/dT>0$). The upward curvature of ρ_{xx} versus T curve suggests that ρ_{xx} exhibits superlinear temperature dependence. In Figure 4.2(c), the Hall resistivity (ρ_{xy}) is plotted as a function of magnetic field at 2 K. Figure shows that ρ_{xy} is negative and increases linearly with field. From the slope of the Hall resistivity, the den-

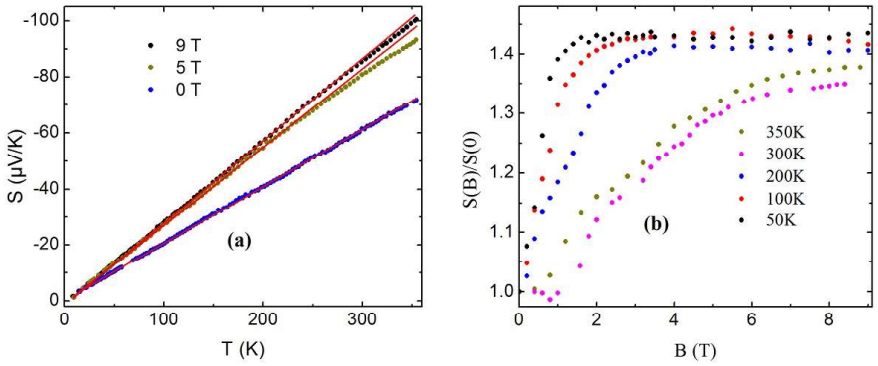

Figure 4.3: (a) Temperature dependence of the Seebeck coefficient (S) of Cd_3As_2 single crystal up to 350 K at 0, 5 and 9 T fields. Solid line shows the linear T dependence of S. (b) Magnetic field dependence of the normalized thermoelectric power at different temperatures between 50 and 350 K up to 9 T, where $S(0)$ is the zero-field Seebeck coefficient at the respective temperatures.

sity of charge carrier (n) is calculated to be $\sim 6.8\times10^{18}$ cm^{-3}. Using the value of resistivity, we have calculated carrier mobility (μ) at 2 K $\sim 1.3\times10^{4}$ cm^2 V^{-1} s^{-1}. These values of carrier density and mobility are close to the earlier reports [54, 56, 62, 63].

4.3.2 Temperature and magnetic field dependence of the Seebeck coefficient of Cd_3As_2

In Figure 4.3(a), the Seebeck coefficient for Cd_3As_2 is plotted as a function of T up to 350 K both in presence and absence of external magnetic field. The negative sign of S implies that the charge transport is dominated by electrons, which is consistent with the negative sign of the Hall coefficient. Remarkably, S shows a linear T dependence almost up to 350 K at zero and 9 T magnetic field, whereas at 5 T, it shows a weak sublinear behavior at high temperature. A qualitatively similar temperature dependence of S has been observed earlier in polycrystalline

sample over the temperature range 77-270 K in absence of external magnetic field [68]. It will be worthy to compare the temperature dependence of the Seebeck coefficient of Cd_3As_2 with that of graphene because of their striking similarities in electronic properties and band dispersion. The linear behavior of the Seebeck coefficient over a wide temperature range has also been reported for graphene [67, 69]. In graphene, however, both the type and density of charge carrier can be tuned by applying gate voltage. Figure 4.3(b) shows the magnetic field evolution of S at some representative temperatures. S increases monotonically with field and tends to saturate at high fields. At lower temperatures, below $T<$ 200 K, the relative enhancement of S from its zero-field value depends very weakly on field and almost insensitive to temperature above ∼2 T. This indicates that the $\frac{S(B)}{S(0)}$ as well as the slope of $S(T)$ curves in the low-temperature region converge faster with field to a definite value. At higher temperatures, the saturation behaviour of $\frac{S(B)}{S(0)}$ appears at higher field strengths. For example, at 350 K, about 30% increase in S is observed at 5 T and, above 8 T, S tends to saturate at ∼95 μV/K. The weak sublinear behaviour of $S(T)$ at 5 T in the high temperature region [Figure 4.3(a)] can be explained from such kind of field dependence of S.

In past, it was believed that Cd_3As_2 belongs to the same family as InSb. Korenblit and Sherstobitov developed a semiclassical theory for the transport phenomenon for InSb-type degenerate semiconductors, assuming that the change in energy of the electrons on scattering is less than $2k_BT$ [70]. The validity of the above approach has also been experimentally verified for Cd_3As_2 [71]. According to the semiclassical theory, the saturation value of S (S_∞) at high field, in terms of the energy (ε) dependence of the electron concentration (p) at the Fermi energy

(E_F), is given by [70, 71]

$$S_\infty = \frac{\pi^2 k_B}{3e}\frac{k_B T}{E_F}\frac{d\ln p}{d\ln \varepsilon}. \tag{4.1}$$

It was also assumed that $p \propto \varepsilon^s$, where s determines the nature of energy dispersion of the system. Thus, the above expression simplifies to, $S_\infty = \frac{\pi^2 k_B}{3e}\frac{k_B T}{E_F}s$. In three dimensions, s is 3/2 for a usual parabolic band and 3 for a linear band. For Cd_3As_2 crystal, we have deduced $E_F \sim 270$ meV from the magnetotransport and magnetization measurements [64]. This value of E_F is close to that determined by several other groups from magnetotransport studies [54, 56, 63, 72]. Now, using the experimental value of S_∞ at 350 K in the simplified expression of Equation 4.1, we find $s \sim 2.9$. The field dependence of S has also been analyzed for temperatures below 350 K. With decreasing T, S tends to saturate at a lower field. The value of S, however, turns out to be very close to 3 at all the temperatures. Thus, the field dependence of the Seebeck coefficient clearly demonstrates the linear dispersion of 3D Dirac fermion in Cd_3As_2. In graphene, by tuning the carrier density through gate voltage, an inverse square-root dependence of S on carrier density has been observed, which is a signature of the linear dispersion in this compound [67].

4.3.3 Analysis of the magnetic field evolution of the scattering time in Cd_3As_2

For $T << T_F$, where T_F is the Fermi temperature, the linear T dependence of S has been ascribed to the Mott formula,

$$S = \frac{\pi^2 k_B^2}{3e}\frac{T}{\sigma(\mu)}\frac{\partial\sigma(\varepsilon)}{\partial\varepsilon}|_{E_F}, \tag{4.2}$$

where $\sigma(\varepsilon)$ is the energy-dependent conductivity. $\sigma(\varepsilon)$ can be expressed in terms of Fermi velocity (v_F), density of states (D) and energy-dependent scattering time τ; $\sigma(\varepsilon) = e^2 v_F^2 D(\varepsilon)\tau(\varepsilon)/2$ [73]. For graphene, $D(\varepsilon)$=$g|\varepsilon|/2\pi\hbar^2 v_F^2$ where g is the total degeneracy. Assuming the energy-dependent scattering time $\tau \propto \varepsilon^m$, one gets $S = \frac{\pi^2 k_B}{3e}\frac{k_B T}{E_F}(m+1)$.

It has been shown that the Mott formula for graphene holds good up to temperature $T \sim 0.2T_F$ [67, 69]. As $D(\varepsilon) = \frac{\varepsilon^2}{2\pi^2\hbar^3 v_F^3}$ for a 3D Dirac system, considering Equation 4.2 and the energy-dependent scattering time $\tau \propto \varepsilon^m$, we get

$$S = \frac{\pi^2 k_B}{3e}\frac{k_B T}{E_F}(m+2). \tag{4.3}$$

We have analyzed the linear T dependence of S using Equation 4.3 and deduced $m$$\sim$0.15 at zero field, i.e, τ is very weakly energy dependent. Similarly, the values of m, determined from the linear region of $S(T)$ curves at 5 and 9 T, are found to be close to 1. The energy independence of τ at zero field is consistent with the random mass model of Dirac fermion, where a randomly fluctuating gap is introduced by randomly distributed scatterers (i.e. disorder) [74, 75]. Though the linear T dependence of S has been predicted for the charged impurity (m=2) and short-range disorder (m=-2) scattering, we observe a quite different energy dependence of τ for Cd_3As_2 [76]. However, in graphene, the dominant transport mechanism is the screened Coulomb scattering from charged impurities [77]. In Cd_3As_2, we observe that m increases with field and tends to saturate at m=1 at high fields.

The magnetic field dependence of m can be understood qualitatively from Fig-

ure 4.3(b). In the high-field region, where S shows a saturation-like behavior, the value of m, determined from Equation 4.3, is very close to 1. However, the field above which S starts to saturate is extremely sensitive to temperature. At low temperature, the saturation occurs at a relatively small applied field. For example, at 50 K, S increases very rapidly with the application of field and becomes almost independent of B above 2 T, i.e., m increases sharply from 0.15 at zero field to about 1 at 2 T. As $S(B)$ curve shifts progressively leftward with decreasing T, m is expected to increase very sharply and reach 1 at a much smaller field strength when the temperature is decreased further below 50 K. This implies that the relaxation process at high fields is dominated by the unscreened charged impurity [73]. The evolution of m with field and its saturation are possibly due to the reconstruction of FS by magnetic field. It may be mentioned that SdH and dHvA oscillation studies have probed the FS in the field and temperature region where the value of m is very close to 1. Further studies are necessary to resolve the difference in Fermi surface geometry, constructed from zero-field probe and quantum oscillation technique, as mentioned in the introduction of the present chapter and also to understand the role of magnetic field on charge scattering.

4.3.4 Tuning of charge carrier by In doping

From the above discussion on field and temperature dependence of thermoelectric power, it is clear that one can tune the Fermi surface by applying magnetic field. As a result, m increases from nearly zero to 1. As S depends inversely on the carrier density, one expects that S will decrease upon electron doping in Cd_3As_2. If the linear temperature dependence of S persists with doping, it may be possible to tune the FS to make m negative. With this idea in mind, we have doped a

very small amount of In (2%) at Cd site in Cd_3As_2. To determine the carrier density, the Hall measurement was done at different temperatures in the range 2-300 K, as shown in Figure 4.4(a). The density of electronic charge carrier is calculated to be $\sim 1.5\times10^{19}$ cm^{-3}, which is higher than the typical carrier density in Cd_3As_2. At zero field, the resistivity (ρ_{xx}) of $(Cd_{0.98}In_{0.02})_3As_2$ single crystal decreases monotonically with decreasing temperature down to 2 K as shown in Figure 4.4(b). The residual resistivity ratio [ρ_{xx}(300 K)/ρ_{xx}(2 K)] is about 7 at zero field. At 2 K, μ is calculated to be $\sim 6\times10^4$ cm^2 V^{-1} s^{-1}, which is comparable to that for the undoped crystal. Under application of magnetic field, resistivity shows a metal-semiconductor like crossover as in the case of parent compound [56]. With the increase in field strength, this anomaly enhances and shifts towards higher temperature. Except very few semimetals, like WTe_2, NbP, $Bi_{0.96}Sb_{0.04}$, etc. [78, 79, 80], conventional semimetals do not exhibit such behavior, which may be due to the opening of a gap at the Dirac point. Considering the thermally activated type carrier transport as in the case of semiconductors, $\rho_{xx}(T)=\rho_0 exp(E_g/\kappa_B T)$, a very small energy gap was obtained from the slope of ln(ρ_{xx}) vs T^{-1} plots, as shown in Figure 4.4(c). Inset shows the magnetic field variation of the induced energy gap. The gap increases rapidly with the increase in magnetic field.

4.3.5 Analysis of magnetoresistance and Shubnikov-de Haas oscillations in $(Cd_{0.98}In_{0.02})_3As_2$ crystal

The transverse magnetoresistance of $(Cd_{0.98}In_{0.02})_3As_2$ single crystal is measured in the temperature range from 2 to 300 K with magnetic field along [100] direction and current along [012] direction. The results are shown in Figure 4.5(a). Unlike Cd_3As_2, In-doped single crystal shows non-linear MR [54, 57, 62, 64]. At low tem-

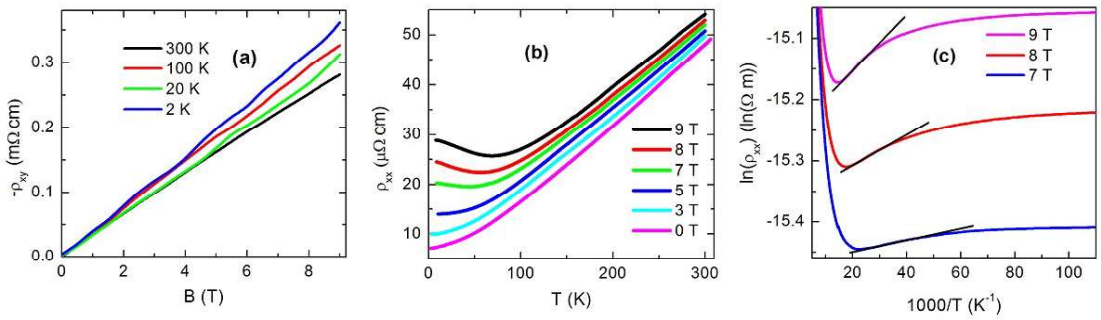

Figure 4.4: (a) Field dependence of the Hall resistance (R_{xy}) at some representative temperatures and (b) temperature dependence of resistivity (ρ_{xx}) for different applied fields for $(Cd_{0.98}In_{0.02})_3As_2$ single crystal. (c) $\ln(\rho_{xx})$ versus $1000T^{-1}$ plot for $(Cd_{0.98}In_{0.02})_3As_2$ crystal. Using the slope in linear region, the thermal activation energy gap induced by the magnetic field has been calculated. Inset shows the field variation of the energy gap above 7 T.

perature, MR is approximately linear only below a threshold value of magnetic field (except in a very narrow region around B=0), while it is quadratic at high field. The quadratic component of MR gradually suppresses with increasing temperature. The first-order derivative of MR [d(MR)/dB] at 50 K has been plotted in Figure 4.5(b) to show the exact magnetic field dependence. The low-field region, which broadens with increasing temperature, is also present in Cd_3As_2 [56]. d(MR)/dB is flat in the intermediate-field region and linear at high field, which correspond to linear and quadratic nature of MR, respectively. d(MR)/dB vs B in Figure 4.5(c) shows that the high-field quadratic region gradually shrinks and the linear region gradually expands with increasing temperature. At 2 K and 9 T, MR is about 280 % which suppresses to only ∼10% at 300 K.

In$(Cd_{0.98}In_{0.02})_3As_2$ crystal, the Shubnikov-de Haas oscillation has been observed up to 20 K. The oscillatory component of MR has been calculated by subtracting a smooth polynomial background from the total MR and is shown in Figure 4.6(a). The amplitude of oscillation reduces with increasing temperature and suppresses

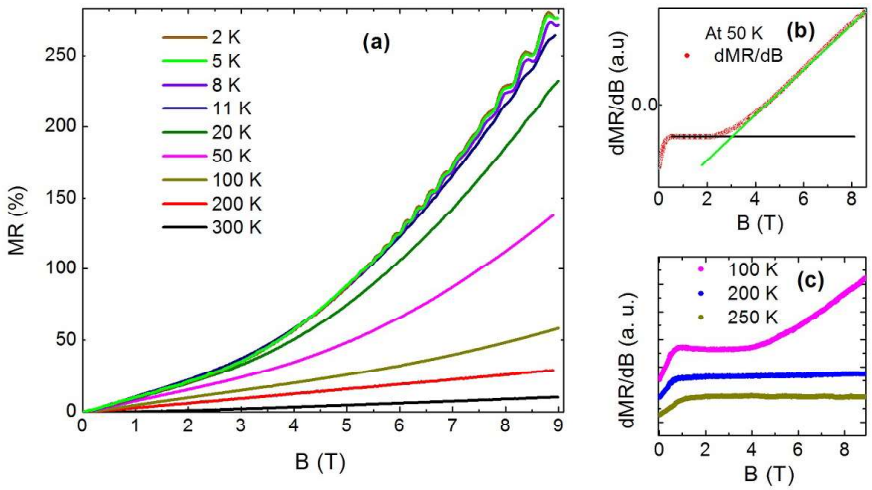

Figure 4.5: (a) Magnetoresistance of $(Cd_{0.98}In_{0.02})_3As_2$ single crystal at some selected temperatures between 2 to 300 K. (b) The first-order derivative of MR [d(MR)/dB] at 50 K. The black and green solid lines represents linear MR and quadratic MR region respectively. (c) d(MR)/dB at some representative temperatures above 50 K.

completely above 20 K. The fast Fourier transform of the oscillation, as shown in the inset of Figure 4.6(a), reveals two distinct frequencies (F) at around 159.3 and 184.6 T, which indicate the presence of two Fermi surface cross sections perpendicular to the applied field direction [100]. The presence of two frequencies in Cd_3As_2 has been ascribed to the nesting of two equivalent ellipsoidal Fermi surfaces beyond the Lifshitz transition [57, 64]. Employing the Onsager relation $F=(\phi_0/2\pi^2)A_F$, the Fermi surface cross sections (A_F) perpendicular to [100] direction are calculated to be 1.52 $\times$ 10^{-2} and 1.76 $\times$ 10^{-2} Å^{-2} respectively, which are at least 3 times higher than the undoped compound [54, 57, 62, 64]. Assuming circular cross sections, the Fermi wave vectors (k_F) are determined to be $\sim$0.07 Å^{-1} and $\sim$0.075 Å^{-1}, respectively.

The thermal damping of the amplitude of oscillation ΔR_T (FFT peak intensity)

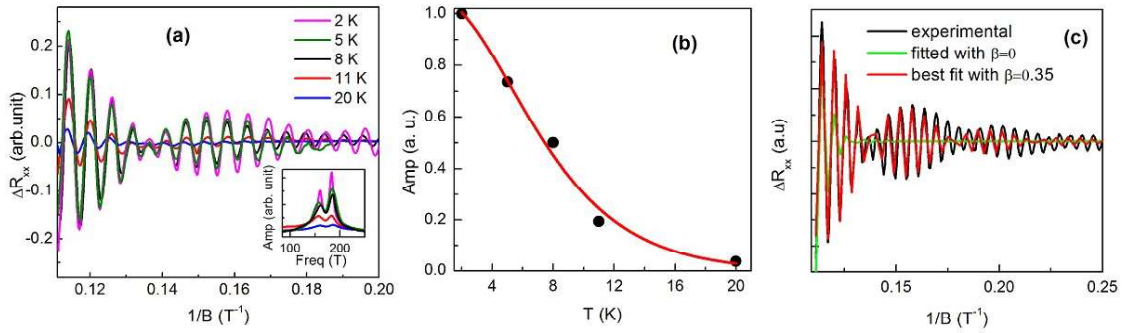

Figure 4.6: (a) The oscillatory component $\triangle R_{xx}$ of MR as a function of $1/B$ at various temperatures with magnetic field along the [100] direction; the inset shows the oscillation frequency after fast Fourier transform in $(Cd_{0.98}In_{0.02})_3As_2$. (b) Thermal damping of oscillation amplitude in $(Cd_{0.98}In_{0.02})_3As_2$ crystal. Solid points are the experimental data and the red line is the fit to the experimental data. (c) The oscillatory component $\triangle R_{xx}$ of MR at 2 K (after subtracting a smooth background). Black, experimental curve; green, fit with β=0; red, fit with non-zero value of β.

[Figure 4.6(b)] can be described by the temperature-dependent part of the Lifshitz-Kosevich formula, as discussed in earlier chapter:

$$\Delta R_T = a\frac{2\pi^2 k_B T/\hbar\omega_c}{\sinh(2\pi^2 k_B T/\hbar\omega_c)}, \tag{4.4}$$

where a is proportionality constant. The energy gap $\hbar\omega_c$ has been determined by fitting the thermal damping of FFT peak intensity at 184 T with Equation 4.4, as a representative. The effective cyclotron mass of the charge carrier ($m_e^\star$) and the Fermi velocity are obtained from the relations ω_c=$eB/m_e^\star$ and v_F=$\hbar k_F/m_e^\star$ respectively. $m_e^\star$ is calculated to be $\sim$0.13 m_e, which is almost three times heavier than that for the parent compound [64]. v_F is found to be $\sim$ 6.1$\times$ 10^5 m/s.

In Figure 4.6(c), the oscillatory component of MR is shown to be fitted by the

Lifshitz-Kosevich formula, ΔR_{xx}=$A\exp(-\frac{c}{B})\cos 2\pi(F/B+0.5+\beta)$, excluding the thermal damping term [Equation 4.4]. We have excluded the thermal damping term because it is a much slower varying function of B than the other two terms. Here, c=$2\pi^2 k_B T_D m_e^\star/\hbar e$ and $2\pi\beta$ is the Berry's phase, where β can take values from 0 to 1/2 (0 for the parabolic dispersion as in the case of conventional metals and 1/2 for the linear dispersion in 3D Dirac system). Taking into account the presence of two frequencies, we have used superposition of two oscillatory components correspond to F_1 = 159.3 and F_2 = 184.6 T to fit the experimental data. Initially, we have fixed β to 0 for parabolic band. But, as shown in Figure 4.6(c), the fitting to the experimental curve is much inferior. By tuning β from 0 to 1/2 in successive steps, the fitting to the experimental data improves progressively. Figure 4.6(c) shows fitting with β=0.35 in the theoretical expression. With further increase in β above 0.35, we observe that the fitting becomes inferior. β>0 demonstrates that the Fermi energy is in the linear dispersing region. This is fully consistent with the earlier STM [52] and ARPES [37] reports, which state that the linear dispersion in Cd_3As_2 persists up to as high as 500 meV from the Dirac point.

4.3.6 Temperature dependence of S in $(Cd_{0.98}In_{0.02})_3As_2$

Figure 4.7(a) shows the temperature dependence of the thermoelectric power of $(Cd_{0.98}In_{0.02})_3As_2$ crystal. Similar to undoped compound, S exhibits linear T dependence, whereas the value of S reduces significantly upon carrier doping. Using the experimental values of k_F and $m_e^\star$ in the Fermi energy expression for the relativistic excitation, E_F=$\hbar^2 k_F^2/m_e^\star$, we get $E_F\sim$ 302 meV. Now, using the slope of $S(T)$ in Equation 4.3, the scattering exponent m is calculated to be $\sim$-0.6 for the

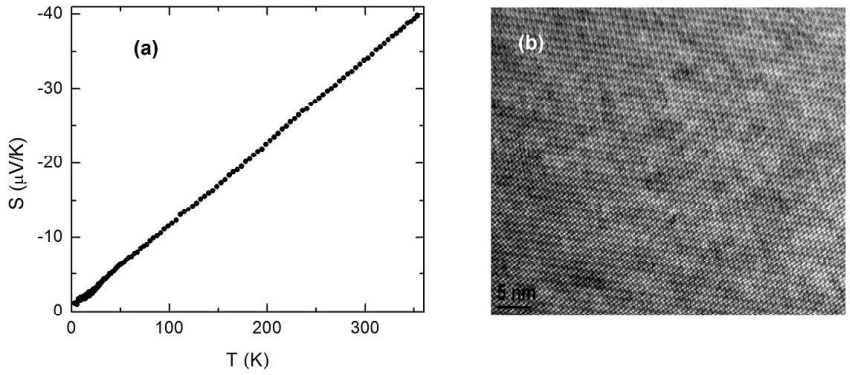

Figure 4.7: (a) Temperature dependence of the thermoelectric power (S) of $(Cd_{0.98}In_{0.02})_3As_2$ up to 350 K. (b) High resolution transmission electron microscopy (HRTEM) image of the crystal.

relaxation process in $(Cd_{0.98}In_{0.02})_3As_2$ crystal. For both acoustic phonon scattering and neutral white-noise short-range disorder, the value of m is known to be -1 [81]. However, the high resolution transmission electron microscopy image of the crystal does not show any signature of short-range disorder [Figure 4.7(b)]. Very clear selective area electron diffraction pattern obtained in HRTEM measurements also consistent with the absence of any kind of disorder [Figure 4.1(c)]. So, the value of scattering exponent can be attributed to the emergence of acoustic phonon scattering.

4.3.7 Magnetotransport and thermoelectric properties of $(Cd_{0.96}In_{0.04})_3As_2$ crystal

With the intension to tune the scattering exponent further, we have doped 4% In at the Cd site in Cd_3As_2. Figure 4.8(a) shows the temperature dependence of resistivity for $(Cd_{0.96}In_{0.04})_3As_2$ crystal. From the figure, it is clear that $\rho_{xx}(T)$, in absence of magnetic field, shows metallic behavior ($d\rho_{xx}/dT>0$) down to lowest

temperature similar to 2% In-doped crystal. However, the value of ρ_{xx} at a given temperature is larger than that for x=0.02 sample but smaller than x=0 sample. The value of residual resistivity ratio ($\sim$5) is smaller compared to that for both x=0 and x=0.02 samples. So, the electrical resistivity and residual resistivity ratio exhibit non-monotonic dependence on In content. We have also measured the Hall resistivity to determine the carrier concentration in this sample. The Hall resistivity has been plotted with B in Figure 4.8(b) at two representative temperatures, 2 and 300 K. Figure shows that ρ_{xy} is independent of temperature and ρ_{xy} vs B is linear up to 9 T. From the slope of ρ_{xy} vs B plot, the carrier density is calculated to be $\sim 2.4\times10^{19}$ cm^{-3}. The deduced value of n is larger than the carrier density for x=0 and 0.02, implying In doping continue to increase carrier concentration. However, the carrier mobility reduces to $\sim 1.1\times10^{4}$ cm^2 V^{-1} s^{-1}. From the above discussion, it is evident that disorder dominates the charge conduction mechanism in Cd_3As_2 above a certain In doping level, in spite of increase in carrier density.

In order to understand the effect of magnetic field on resistivity, we have also measured ρ_{xx} at different applied fields [Figure 4.8(a)]. Figure 4.8(a) shows that the resistivity enhances with the application of magnetic field as in the case of x=0 and 0.02 samples. Similar to x=0 and 0.02, ρ_{xx} for x=0.04 also shows the field-induced metal-semiconductor like crossover with decreasing temperature. However, this phenomenon is weaker than that observed in 0 and 0.02 samples. MR as a function of magnetic field has also been measured and plotted in Figure 4.9(a). However, for this sample, we have not observed any SdH oscillation up to 9 T magnetic field and temperature down to 2 K. We have already shown that the effective mass of the carrier increases significantly with the increase in carrier den-

sity resulting from In doping. Also, the conductivity for the 4% In-doped sample reduces due to the increase of disorder. The absence of quantum oscillation within the measured magnetic field range is possibly due to the increase in carrier effective mass and disorder with In doping. But, surprisingly, Figure 4.9(a) shows large and nonsaturating MR for $(Cd_{0.96}In_{0.04})_3As_2$ like the undoped sample. At 9 T, the MR is as high as $\sim$ 1650% at 2 K and $\sim$ 250% at room temperature. However, the nature of MR is weakly superlinear compared to weakly sublinear MR in undoped Cd_3As_2, which has been shown in Figure 3.2(b) of previous chapter. As pointed out by Parish and Littlewood [82] through statistical simulation, large spatial fluctuations in mobility due to presence of disorder, can lead to large linear magnetoresistance. This benefit of imperfection was first experimentally realized in doped sample of Ag_2Se and Ag_2Te by several groups [83, 84]. Recently, fluctuation in electron mobility due to collision with randomly distributed low-mobility islands (i.e., disorders), has been ascribed as a possible source of large and linear magnetoresistance in Cd_3As_2 [62]. It has also shown that the value of MR scales with the mobility of charge carrier. As shown in Table I, with further indium doping in Cd_3As_2 above 2%, the large linear MR is recovered and the mobility of charge carrier is reduced from what is observed in 2% In-doped sample. This disorder-induced MR in 4% In-doped sample is consistent with the above mentioned statistical model. Controlling MR by tuning disorder through doping may be a potential route for the fabrication of magnetic field sensors.

In Figure 4.9(b), the Seebeck coefficient for $(Cd_{0.96}In_{0.04})_3As_2$ is plotted as a function of temperature up to 300 K. Consistent with the increase in carrier density, the value of S reduces further. Similar to undoped and 2% In-doped sample, S vs T is linear throughout the temperature range, i.e., the Mott semiclassical

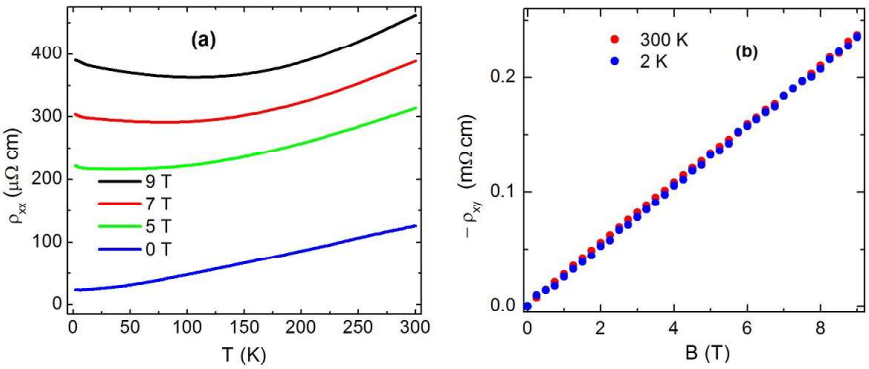

Figure 4.8: (a) Resistivity (ρ_{xx}) as a function of temperature for $(Cd_{0.96}In_{0.04})_3As_2$. (b) Field dependence of the Hall resistance (R_{xy}) at 2 and 300 K.

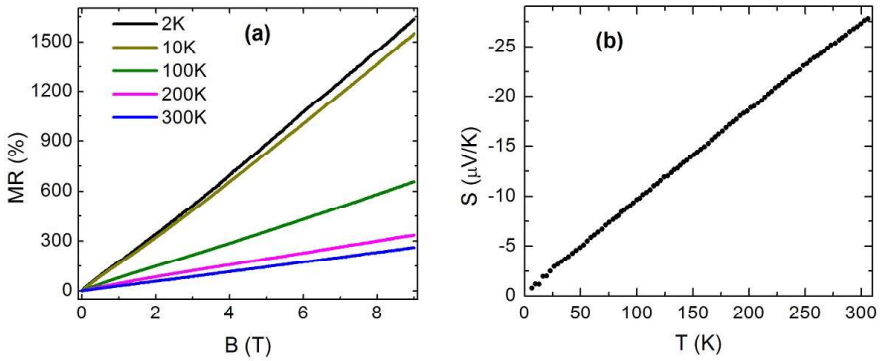

Figure 4.9: (a) Magnetoresistance of $(Cd_{0.96}In_{0.04})_3As_2$ at a few representative temperatures from 2 to 300 K. (b) Temperature dependence of the thermoelectric power (S) of $(Cd_{0.96}In_{0.04})_3As_2$ up to 300 K.

formula [Equation 4.2] is obeyed. However, due to the absence of quantum oscillations in the magnetoresistance data, it is not possible to comment whether 0.04 In-doped sample hosts Dirac semimetallic phase or not. Also, we cannot deduce m using Equation 4.3 due to the lack of knowledge on E_F.

Table 4.1: The values of Seebeck coefficient at 300 K (S_{300K}), resistivity at 2 K (ρ_{2K}), carrier density (n), carrier mobility (μ) and magnetoresistance at 2 K and 9 T for Cd_3As_2, 2% indium-doped [Cd_3As_2(02)] and 4% indium-doped [Cd_3As_2(04)] samples.

	S_{300K} μV/K	ρ_{2K} $\mu\Omega$-cm	n 10^{18}cm^{-3}	μ 10^4cm^2/Vs	MR %
Cd_3As_2	60	70	6.8	1.3	1600
Cd_3As_2(02)	34	7	15	6	280
Cd_3As_2(04)	27	23	24	1.1	1650

4.4 Conclusion

In conclusion, the Seebeck coefficient shows linear temperature dependence over a wide range, which is in agreement with the Mott's relation. The signature of three-dimensional linear dispersion in Cd_3As_2 has been clearly reflected from the magnetic field dependence of S. The relaxation process of charge carrier in Cd_3As_2 is found to be extremely sensitive to magnetic field and carrier doping. Analysis reveals that the scattering time evolves from being nearly energy independent to becoming linearly dependent on energy as the magnetic field increases. Fermi surface is strongly affected and the scattering time enters into the inverse energy-dependent regime with 2% indium doping at Cd ion site. Further doping (4%) increases disorder in the system and SdH oscillation is no more traceable down

to 2 K and up to 9 T applied magnetic field. Surprisingly, this higher doped sample shows large and linear magnetoresistance like the undoped compound. The observed behaviour of MR is consistent with the statistical model, which states that large spatial fluctuation in carrier mobility due to presence of disorder, can generate large linear MR. This disorder controlled MR in Cd_3As_2 may have the potential benefit in magnetic sensors, magnetic switches, memory devices, etc.

5

Coexistence of topological Dirac fermions on the surface and three-dimensional Dirac cone state in the bulk of $ZrTe_5$ single crystal

5.1 Introduction

The low-dimensional pentatellurides, $ZrTe_5$ and $HfTe_5$, synthesized in 1973 [85], exhibit a peak in the resistivity (ρ) as a function of temperature [86]. This anomaly in the resistivity has been observed at $T_P \sim 145$ K for $ZrTe_5$ and $T_P \sim 80$ K for $HfTe_5$, however, the exact temperature varies from sample to sample [87]. It was shown that the anomalous peak in resistivity shifts to lower temperature with reduced level of impurity in the sample [87]. Recent works on $ZrTe_5$ reported T_P as low as ~60 K, which has been ascribed to very low defect and impurity con-

centration in the samples [41, 88]. Most of the earlier works have been directed towards understanding the origin of this peak. The charge carrier switches from holes at $T>\mathrm{T}_P$ to electrons for $T<\mathrm{T}_P$, which is reflected in the sign change of thermoelectric power [89] and Hall coefficient [90]. Initially, it was believed that this resistive anomaly arises due to charge-density wave transition, similar to that occurs in $NbSe_3$ [91]. But the absence of lattice modulation, etc., eliminate the idea of charge density wave formation in $ZrTe_5$ [92]. Subsequently, the concept of polaronic conduction [93], semimetal-semiconductor phase transition [94] and so on, have emerged until a recent theoretical work suggests that the monolayer of $ZrTe_5$ and $HfTe_5$ is the most promising candidate for the quantum spin Hall due to the large bulk gap [40]. Suddenly, a material known for its large thermoelectric power [89], resistivity anomaly [85] and large positive magnetoresistance [95], has been brought to our attention to study the topological properties of relativistic Dirac fermion in condensed matter physics [41, 88, 96, 97, 98, 99, 100, 101, 102, 103].

In recent times, it has been established from angle resolved photoemission spectroscopy (ARPES) measurement that the temperature dependence of the electronic band structure across the Fermi energy is responsible for the anomalous peak in resistivity [96]. However, $ZrTe_5$ is not free from debate, facing a bigger question. Theoretical calculation shows that electronic property of bulk $ZrTe_5$ is very sensitive to the lattice parameters. Depending on the values of lattice parameters it can be either a weak or a strong three-dimensional topological insulator [40]. On the other hand, ARPES [41, 96], infrared spectroscopy [88, 97] and magneto transport [41] studies show three-dimensional linear dispersion with a small semiconducting gap between the valence and conduction band, i.e., 3D Dirac fermionic excitation

with a small mass gap. Do theory and experiment contradict each other or the topological Dirac fermions on the surface and three-dimensional Dirac cone state in the bulk can coexist simultaneously in $ZrTe_5$? We have addressed the ambiguity in the present chapter .

5.2 Sample preparation, characterization, and experimental details

High quality single crystals of $ZrTe_5$ were grown by iodine vapor transport method similar to that reported earlier [104]. A stoichiometric mixture of Zr (Alfa Aesar 99.9%) and Te (Alfa Aesar 99.99%) was sealed in a 15 cm long quartz tube with iodine ($\sim$ 5 mg/cc) and placed in a box furnace. It was then heated for seven days at 520°C and cooled to room temperature at 10°C/h. Next, the tube was shifted to a two-zone gradient furnace. One end of the tube containing the product was placed at 540°C while the other end of the tube was placed at the cooler zone of the furnace at 450 °C to provide a temperature gradient for four days. After slowly cooling ($\sim$30°C/h) it to room temperature, single crystals with needlelike morphology were obtained at the cooler end. Typical size and morphology of few representative single crystals are shown in Figure 5.1(a).

Phase purity and the structural analysis of the samples were done by high resolution powder x-ray diffraction (XRD) technique (Rigaku, TTRAX II) using Cu-K_α radiation [Figure 5.1(b)]. Within the resolution of XRD, we have not seen any peak due to the impurity phase. The calculated value of the lattice parameters are a=3.96 Å, b=14.50 Å and c=13.78 Å with space group symmetry $Cmcm$, sim-

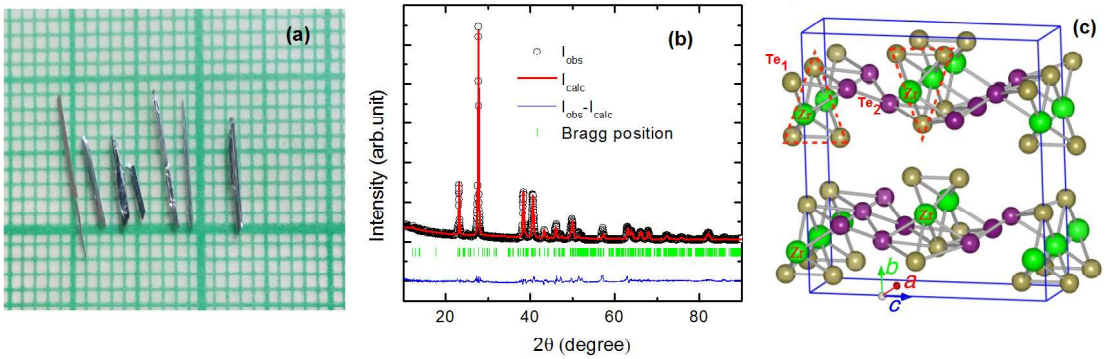

Figure 5.1: (a) Typical size and morphology of few representative single crystals of $ZrTe_5$. (b) X-ray diffraction pattern of powdered single crystals of $ZrTe_5$. Black open circle, experimental data; red, the calculated pattern; blue, the difference between experimental and calculated intensities; green, the Bragg positions. (c) Atomic structure of $ZrTe_5$. Reproduced from Ref. [40].

ilar to the earlier reports [105, 106, 107]. As shown in Figure 5.1(c), the structure of the pentatellurides consists of trigonal prismatic chains of $ZrTe_3$ along **a** axis connected via parallel zigzag chains of Te atoms along the **c** axis, which together form 2D planes weakly bonded via van der Waals force along the **b** axis [40]. Figure 5.2(a) shows the crystallographic directions of a typical $ZrTe_5$ single crystal and electrical contacts for resistivity measurements.

The resistivity measurements were done by standard four-probe technique. Electrical contacts were made using conductive silver paste. The electrical transport measurements were carried out in 9 T physical property measurement system (Quantum Design) and cryogen free measurement system (Cryogenic Limited). Magnetization was measured using a Superconducting Quantum Interference Device−Vibrating Sample Magnetometer (SQUID-VSM) (Quantum Design). Before the magnetization measurements, the system was standardized using single crystal of diamagnetic bismuth (Alfa Aesar 99.99%) and paramagnetic palladium [Appendix A].

5.3 Results

5.3.1 Temperature dependence of resistivity both in presence and absence of external magnetic field

Resistivity and transverse magnetoresistance measurements are done by applying current along the **a** axis and magnetic field perpendicular to the **ac** plane, i.e., along **b** axis. Figure 5.2(b) shows the temperature dependence of resistivity of $ZrTe_5$ single crystal both in presence and absence of magnetic field. The zero-field ρ exhibits metallic behavior ($d\rho/dT>0$) down to 25 K. Below 25 K, ρ shows a weak upturn, i.e., a crossover from metallic to semiconducting like behavior. However, several earlier reports show that a broad peak appears in the temperature dependence of ρ, which is known as the resistivity anomaly of $ZrTe_5$ [41, 85, 86, 87, 88]. We have already mentioned in the introduction that the temperature at which ρ shows peak varies widely; from 60 K to 170 K. It was believed in the past that the position of the peak depends on the strength of impurity and defect in the sample [87]. However, in the light of new observations, chemical doping can also play a crucial role in determining the peak position [96, 103]. It has been argued that the binding energy shift of the valence and conduction bands as a function of temperature is responsible for the peak at T_P [96, 103]. With increasing temperature from 2 K, the sign of the charge carrier changes from negative (electron) to positive (hole) and the peak in $\rho(T)$ appears when the chemical potential crosses the gap ($\sim$50$\pm$10 meV) from conduction band to valence band. The absence of resistivity peak down to 2 K in the present sample could be attributed to hole doping, unlike electron doping in all the previously reported

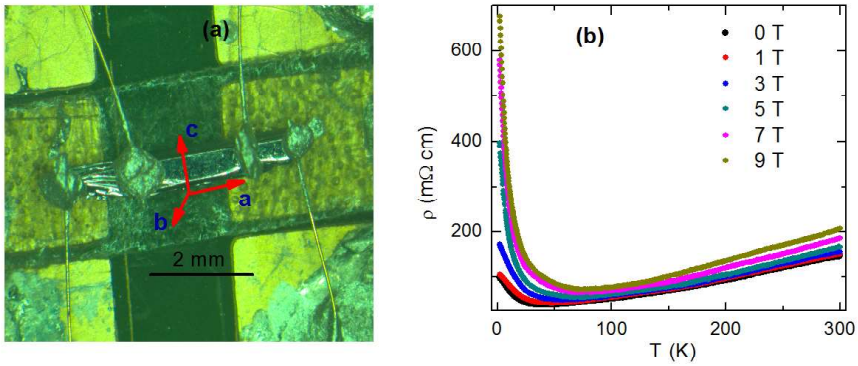

Figure 5.2: (a) Different crystallographic directions and electrical contacts in a representative piece of $ZrTe_5$ single crystals. (b) Temperature dependence of resistivity (ρ) both in presence and absence of external magnetic field.

samples [41, 85, 86, 87, 88, 96]. A very recent experimental research has observed similar temperature dependence of resistivity, and established this behaviour as a characteristic of hole doped $ZrTe_5$ [108]. Under application of magnetic field, ρ increases sharply at low temperature and the metal-semiconductor crossover shifts to higher temperature, which are consistent with the earlier reports [41, 107]. But, no re-entrant metallic state has been observed up to 9 T.

5.3.2 Hall resistivity and transverse magnetoresistance

To further ensure the absence of resistivity anomaly, which has been ascribed to the switching of p-type semimetal to n-type semimetal state, we have done Hall measurements down to 2 K. Figure 5.3(a) shows that the Hall resistivity (ρ_{xy}) remains positive over the entire temperature range 2-300 K. The absence of sign change in ρ_{xy} is consistent with the observed T dependence of ρ. One can see that ρ_{xy} is linear over the entire field range except at low temperature, where an upward curvature appears at high fields due to the Shubnikov-de Haas oscillations. A systematic increase of the slope of the Hall resistivity with decreasing temperature

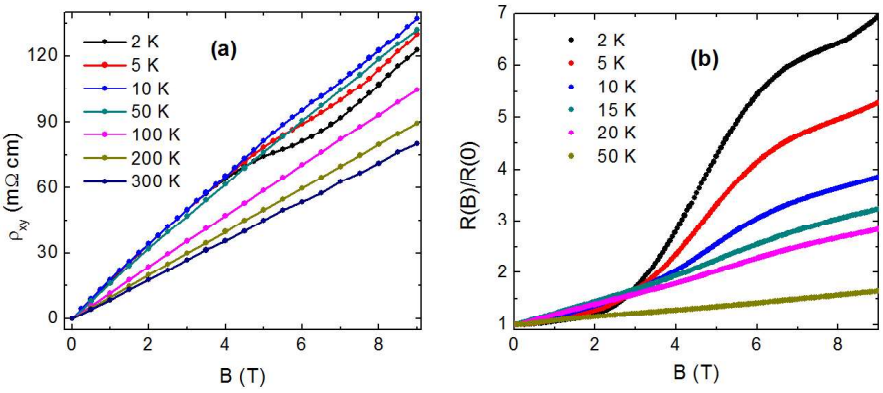

Figure 5.3: (a) Hall resistivity (ρ_{xy}) of $ZrTe_5$ single crystal at several representative temperatures over the range 2-300 K. (b) Transverse magnetoresistance ($I \perp \vec{B}$) normalized to the zero field value upto 9 T.

is consistent with the temperature evolution of electronic band structure in $ZrTe_5$ [96, 103]. From the slope of $\rho_{xy}(H)$, the bulk carrier density (n) is calculated to be $\sim 4\times10^{16}$cm^{-3} and $\sim 7\times10^{16}$cm^{-3} at 2 and 300 K, respectively. We would like mention that the carrier density in the present crystal is almost one order of magnitude smaller than the earlier reported ones [100, 109]. Figure 5.3(b) shows the normalized magnetoresistance (MR) up to 9 T magnetic field. MR is large, positive and shows no sign of saturation in the measured temperature and field range. The observed behavior of MR is similar to the earlier reports [95, 98, 99]. At low temperature, MR is dominated by a very low frequency ($\sim$3 T) Shubnikov-de Haas oscillation, which implies the presence of a tiny Fermi pocket, consistent with the low carrier density determined from the Hall measurements. Employing the Onsager relation $F=(\phi_0/2\pi^2)A_F$, we have calculated the cross-sectional area (A_F) of the Fermi surface normal to the field $\sim 6.2\times10^{-5}$ Å^{-2}. At high temperature, where the quantum oscillation suppresses, MR becomes linear.

5.3.3 Longitudinal magnetoresistance and Chiral anomaly

As proposed by Hermann Weyl in 1929, the four-component massless Dirac equation in three spatial dimensions can be separated into two two-component equations, $\imath\frac{\partial\Psi}{\partial t}=\pm c\vec{\sigma}.\vec{p}\Psi$, where $\vec{\sigma}$ and $\vec{p}$ are the Pauli matrices and momentum respectively. The above equation describes particles with a definite chirality $\vec{\sigma}.\hat{p}$, known as Weyl fermions. Also, according to the classical equation of motion the number of fermions with plus or minus chirality is conserved separately. The relativistic theory of charged chiral fermions in three spatial dimensions holds the so-called chiral anomaly– non-conservation of chiral charge induced by external gauge fields with non-trivial topology, known as Adler-Bell-Jackiw anomaly [110, 111]. Nielsen and Ninomiya provided a physical picture of the chiral anomaly in the context of condensed matter physics [112]. Considering a band structure in three dimensions which supports two Weyl nodes with opposite chirality separated in momentum space and applying a magnetic field along the line joining the Weyl nodes, they predicted an enhanced magneto-conductance due to the charge pumping from one node to another in presence of an electric field $\vec{E}$ parallel to $\vec{B}$.

In 3D Dirac semimetals, a four-component massless Dirac fermion is nothing but the two copies of distinct Weyl fermions. The application of magnetic field splits the four-fold degenerate Dirac node into two Weyl nodes of opposite chirality, along the direction of magnetic field [113, 114]. Initially, the plus and minus chirality fermions in the different Weyl nodes have same chemical potential $\mu^+ = \mu^-$. Whereas, $\vec{E}$ parallel to $\vec{B}$ creates an imbalance ($\mu^+\neq\mu^-$) between the two Weyl nodes with opposite chirality, which induces a charge pumping from one Weyl node to another. The net current generation due to the chiral imbalance is $\mathrm{j}_c = \frac{e^2B}{4\pi^2\hbar^2c}(\mu^+\text{-}\mu^-)$ [41, 114]. Again, $(\mu^+\text{-}\mu^-)$ is proportional to $\vec{E}.\vec{B}$. As a result,

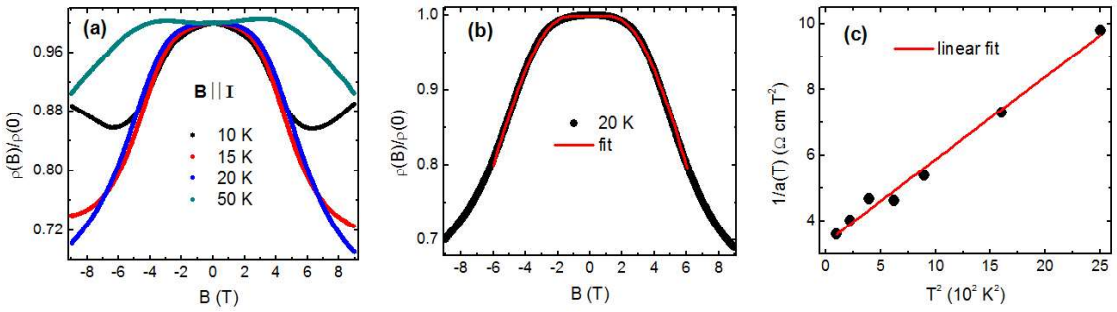

Figure 5.4: (a) Magnetoresistance measured at temperatures from 10 to 50 K, when applied current and magnetic field are parallel to each other, (b) Magnetoresistance at 20 K, fitted with the theoretical expression, $\rho_c = \frac{1}{[\sigma_0 + a(T).B^2] + \frac{1}{\rho_0 + A.B^2}}$, and (c) Temperature dependence of $1/a$, where a is in the units of S cm^{-1} T^{-2}.

the enhanced magneto-conductance is expected to show quadratic B dependence in the form, $\sigma_c = \sigma_0 + a(T).B^2$, where σ_0 is the zero-field conductivity. The field independent constant, $a(T)$ has the inverse T^2 dependence,

$$a(T) = \frac{e^2}{\pi\hbar}\frac{3}{8}\frac{e^2}{\hbar c}\frac{\nu^2}{\pi^3}\frac{\tau_\upsilon}{T^2 + \frac{\mu^2}{\pi^2}}, \tag{5.1}$$

where ν, τ_υ and μ are the Fermi velocity, chirality changing scattering time and chemical potential, respectively [41]. But, in addition to the negative quadratic MR associated to chiral anomaly, a small positive MR component associated to different physical phenomena may contribute to transport [115, 116, 117]. Conventional nonlinear band contribution around the Fermi level, which has the field dependence, $\sigma_N = \frac{1}{\rho_0 + A.B^2}$, is common [115, 116, 117]. As a result, the longitudinal magneto-conductance can be fitted with the theoretical expression, $\sigma = \sigma_c + \sigma_N = [\sigma_0 + a(T).B^2] + \frac{1}{\rho_0 + A.B^2}$.

To probe the chiral anomaly, we have measured longitudinal magnetoresistance

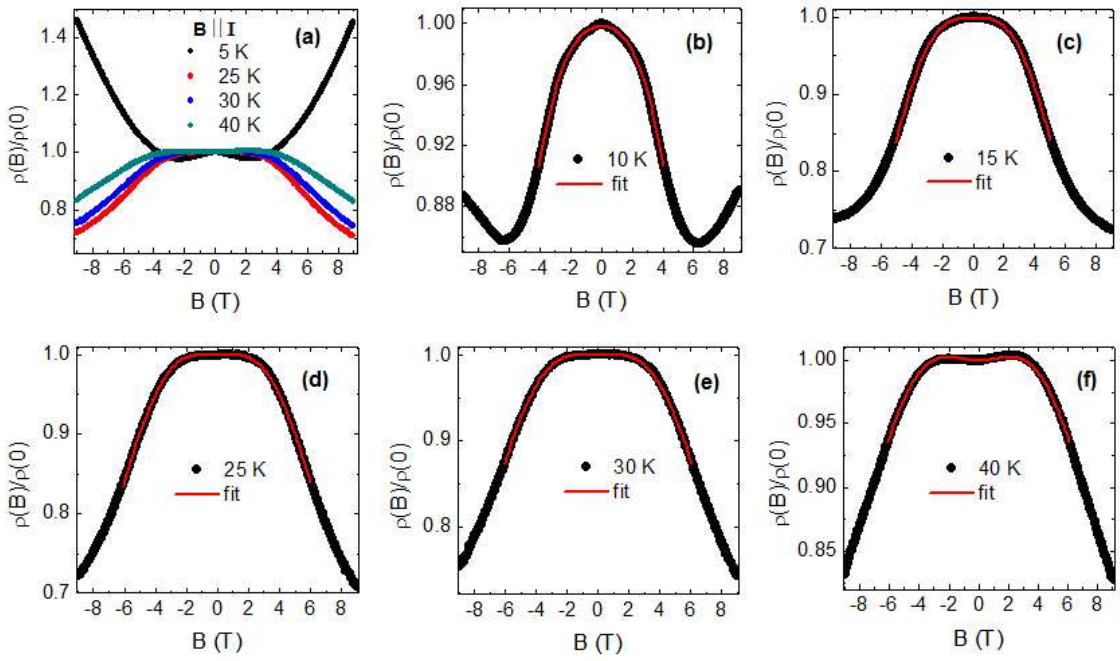

Figure 5.5: (a) Longitudinal magnetoresistance measured at temperatures 5 K, 25 K, 30 K and 40 K, when applied current and magnetic field are parallel to each other. (b), (c), (d), (e) and (f) are the fit to the experimental data with the theoretical expression, $\rho_c = \frac{1}{[\sigma_0 + a(T).B^2] + \frac{1}{\rho_0 + A.B^2}}$, at several representative temperatures.

(LMR) by applying both the current and magnetic field along the **a** axis. As shown in Figure 5.4(a), the resistance at 10 K gradually decreases with increasing field until an upturn occurs at high field. A small positive transverse MR component due to unavoidable misalignment in parallel configuration is responsible for this high field upturn. As the positive MR component rapidly suppresses with increasing temperature, the longitudinal negative MR becomes more clearly visible at higher temperatures. LMR at several other temperatures from 5 to 40 K, has been shown in Figure 5.5(a). Due to large positive transverse MR component at low temperatures from small misalignment in $I \parallel B$ configuration, the field dependence of LMR at 5 K shows weak negative MR in a narrow field range. With the increase in temperature above 40 K, however, the negative MR itself becomes very weak. The negative LMR was reproduced by several independent measurements and also verified in different crystals. Chiral anomaly induced negative LMR has also been observed in earlier magneto-transport studies in $ZrTe_5$ [41, 117]. The nature and strength of negative LMR in the present sample are comparable to that reported earlier [41, 117]. LMR has been fitted with the inverse of the above mentioned theoretical expression for the longitudinal magneto-conductance and shown at a temperature 20 K in Figure 5.4(b). A good fitting between the theoretical expression and experimental data is reflected in the above mentioned figure. By fitting LMR at different temperatures in the range 10-50 K [Figure 5.5(b)-(f)], we have calculated the values of the parameter a. As the negative LMR is much weaker compared to large transverse MR component, we have not considered the LMR vs B plot at 5 K for fitting. Observed values of $a(T)$ at 10 to 50 K indicate that the strength of induced chiral current for the present sample is comparable with the earlier report on $ZrTe_5$ [41]. In Figure 5.4(c), we have plotted a^{-1} vs T^2. One can

see from the figure that a^{-1} is almost linear in T^2, as predicted theoretically. Thus, the negative longitudinal MR in $\vec{E}||\vec{B}$ configuration implies four-component massless Dirac fermionic excitation in the bulk state of $ZrTe_5$ single crystal [41, 117]. It may be noted that the negative MR due to induced chiral anomaly is a well established phenomenon in three-dimensional Dirac semimetals, which has also been observed in Cd_3As_2 [114] and Na_3Bi [118]. Presence of a small gap between the upper and lower Dirac cone in bulk may reduce the magnitude of the chiral current, but cannot destroy it fully [41].

5.3.4 Signature of topological surface state from magnetization measurements

The low-energy physics of the surface state for a three-dimensional topological insulator can be described by the Dirac type effective Hamiltonian, $H_{sur}(k_x,k_y)=\hbar v_F(\sigma^x k_y - \sigma^y k_x)$, where v_F is the Fermi velocity [119, 120]. Thus, for a fixed translational momentum $\vec{k}$, the "spin", denoted by the Pauli matrix $\vec{\sigma}$, has a fixed direction for the eigenstate of the Hamiltonian. This is the most important property of the nontrivial topological surface state in 3D topological insulators, known as "spin-momentum locking". As the "spin" is always perpendicular to the momentum, one can introduce a helicity operator for the spin texture on circular constant energy contour of the Dirac cones [120], $\hat{h}=(1/k)\hat{z}.(\vec{k}\times\vec{\sigma})$. This leads to left-handed spin texture for the upper Dirac cone and right-handed spin texture for the lower Dirac cone in the momentum space. Whereas at the Dirac point, as long as the Dirac spectrum is not gapped, the electron spin should be free to align along the applied magnetic field due to the singularity in spin orientation [121]. This predicts a low-field paramagnetic peak in the susceptibility curve $\chi(H)$.

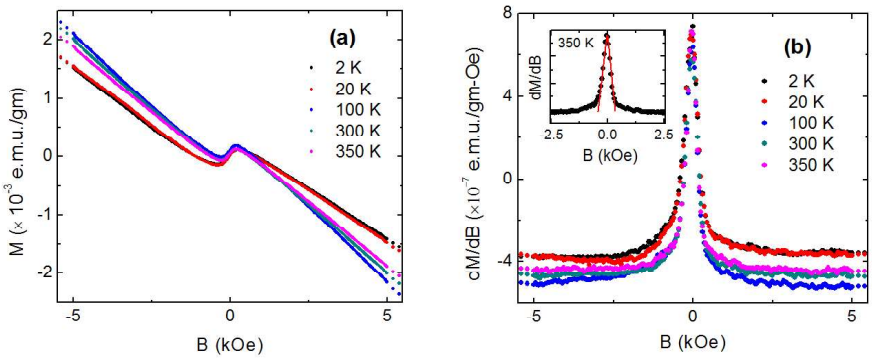

Figure 5.6: (a) Magnetization of $ZrTe_5$ single crystal, measured at several representative temperatures from 2 to 350 K. (b) Differential susceptibility ($\chi = \frac{dM}{dB}$) obtained after taking derivative of the magnetization with respect to external magnetic field. Inset shows the linear B dependence of χ, as B tending towards zero on both side of the zero field cusp at representative temperature 350 K.

Figure 5.6(a) shows the magnetization of single crystal of $ZrTe_5$ with magnetic field along the **a** axis. Over the whole range of temperature from 2 to 350 K, $ZrTe_5$ shows diamagnetic signal except a paramagnetic upturn in the low-field region. It might be worthy to mention that single crystals of standard diamagnetic bismuth and three-dimensional Dirac semimetal Cd_3As_2 do not show this type of behaviour [Appendix A]. On the other hand, similar paramagnetic response has been observed in single crystals of well established three-dimensional topological insulator $Bi_{1.5}Sb_{0.5}Te_{1.7}Se_{1.3}$ [Appendix A]. Figure 5.6(b) shows that a cusp-like paramagnetic susceptibility sharply rises above the diamagnetic floor in a narrow field range of ∼2 kOe around zero field. The height of the peak from the diamagnetic floor and its sharpness are insensitive to temperature. This singular response of susceptibility shows no sign of thermal rounding up to as high as 350 K (∼32 meV), which is almost one-half of the bulk band gap [41, 103]. Similar robust and singular paramagnetic response have been reported for the family of three-dimensional topological insulators which is the fingerprint of the helical spin

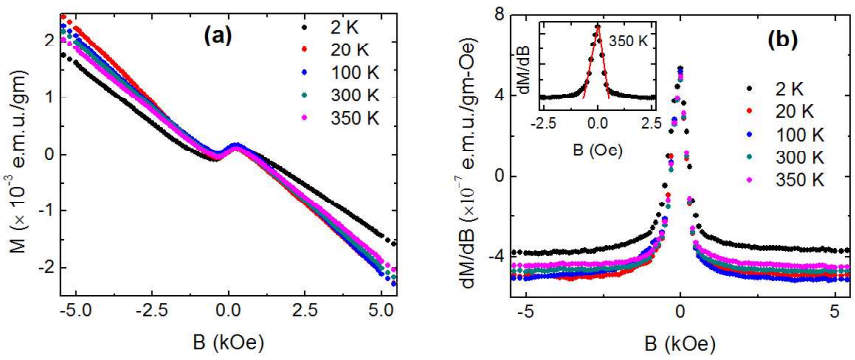

Figure 5.7: (Color online) (a) Magnetization of $ZrTe_5$ single crystal, which was kept for three weeks in desiccator from the first measurements [Figure 5.6]. (b) Differential susceptibility ($\chi = \frac{dM}{dB}$) obtained after taking derivative of the magnetization with respect to external magnetic field. Inset shows the linear B dependence of χ as B tending towards zero on both sides of the zero field cusp at representative temperature 350 K.

texture of the topological Dirac fermions on the surface [121, 122]. Setting both the chemical potential μ and temperature to zero, one can show that, at low field, this paramagnetic Dirac susceptibility decays linearly from its zero-field value [121] as, $\chi_D(B) \cong \frac{\mu_0}{4\pi^2}[\frac{(g\mu_B)^2}{\hbar v_F}\Lambda - \frac{2(g\mu_B)^3}{\hbar^2 v_F^2}|B| + \ldots]$. Where g is the Landé g-factor and Λ is the effective size of the momentum space contributing to the singular part of the free energy. It has been argued [121] that the maximum of the susceptibility, i.e., the peak height at zero field over the diamagnetic floor, depends on Λ, and thus controlled by the bulk bands. Whereas the nature of the singularity (i.e. cuspiness and linear-in-field decay of susceptibility at low fields, almost absence of thermal smearing, etc.,) is universal to the entire family of 3D topological insulators. Inset of Figure 5.6(b) shows the linear fit to the experimental data on the both sides of the zero-field cusp. The linear-in-field decay of the paramagnetic response, even at the highest measuring temperature 350 K, is evident from the figure.

Often, surface states show ageing effect, which has been attributed to surface re-

construction and the formation of two-dimensional electron gas due to the bending of the bulk band at the surface [121, 123, 124]. To see whether such behaviour is visible in the present material, magnetization measurements have been done on the same pieces of single crystals after three weeks of the first measurement. The observed field dependence of magnetization and susceptibility are shown in Figure 5.7(a) and Figure 5.7(b). Although the nature of the peak and its robustness against temperature remain unaffected, the reduction in peak height over time may be attributed to the expected ageing effect, similar to that observed in Bi_2Se_3, Sb_2Te_3 and Bi_2Te_3 [121]. It has been pointed out that the spin/orbit texture may also exist in the bulk state of the material with strong spin-orbit coupling, such as in BiTeI [125] and WTe_2 [126]. Keeping this information in mind, one may think the possibility of the singular paramagnetic response from the bulk of $ZrTe_5$. But, as reported by the earlier ARPES measurements [41, 96, 103], the bulk state of $ZrTe_5$ holds a band gap ($\sim$50$\pm$10 meV) between the upper and lower Dirac cone, which disobeys the primary condition for the singularity in electron spin orientation from the spin/orbit texture. Secondly, the negative longitudinal magnetoresistance due to chiral charge imbalance under non-trivial gauge field and ARPES results, established the presence of four-component massless Dirac fermion in the bulk 3D Dirac cone state of $ZrTe_5$. As far as we know, a four-component 3D Dirac fermion originating from the spin-degenerate band, cannot have any spin-orbit texture. The age dependent reduction of the peak height, whereas the diamagnetic back ground is unaffected, also confirms the surface origin of this singular paramagnetic response.

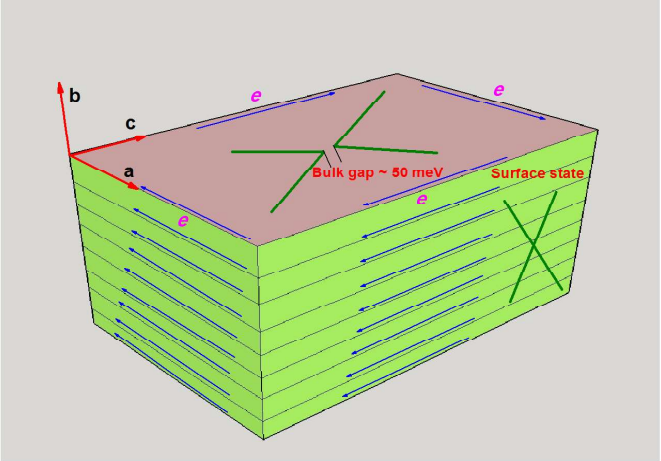

Figure 5.8: A schematic diagram, representing the minimum nontrivial topological nature of the electronic band structure of $ZrTe_5$ single crystal. $ZrTe_5$ monolayers, which lie in the **ac**-plane, stack together along the **b**-axis by weak van der Waals attraction. Independent conducting edge state of monolayers, as shown by the blue arrows in the figure, forms a topological surface state in bulk sample, known as weak three-dimensional topological insulating state.

5.4 Discussion

We have detected a robust zero-field paramagnetic peak in the susceptibility of $ZrTe_5$ due to the helical spin texture associated with the Dirac fermions of the surface state of the three-dimensional topological insulator. Also, the negative longitudinal magnetoresistance implies induced chiral anomaly in $ZrTe_5$, which is the signature of the three-dimensional Dirac fermion in the bulk. This allows one to conclude that $ZrTe_5$ is a novel quantum phase of matter, which hosts both topological Dirac fermions on the surface and three-dimensional Dirac cone state with a mass gap between valence and conduction bands in the bulk. As mentioned earlier, $ZrTe_5$ can be either a weak or a strong three-dimensional topological insulator depending on the values of the lattice parameters [40]. The simplest kind of topo-

logical insulator in three-dimension can be understood by stacking the layers of the 2D quantum spin Hall insulator with weak van der Waals bonding between them [127], similar to the stacking of monolayers of $ZrTe_5$ along **b** axis. A schematic diagram has been shown in Figure 5.8, representing the possible minimum nontrivial electronic state in $ZrTe_5$ single crystal. Blue arrows represent the conducting edge state of a monolayer, which together form a topological surface state in the bulk sample. On the other hand, the bulk band with semiconducting gap is linear enough to show the signature of massless Dirac fermionic excitation in electronic transport.

In condensed matter electronic system, the topological classes are defined on the basis of the elementary concept, which states that the Hamiltonian cannot be smoothly deformed from one class of materials to another without closing the gap in electronic band structure. As a result, at the interface of the two materials with different topological band gap, there should be a conducting surface state [127, 128]. Unless there is a bulk gap, there should be no well-defined topological surface state. So, either band crossing in the bulk, i.e., 3D Dirac node or the 2D Dirac cone surface state can survive. In all 3D topological insulators reported so far, the semiconducting bulk band is highly non-linear and the gap is significantly large ($\sim$300 meV) compared to $ZrTe_5$ [121, 129, 130]. That is why the coexistence of 2D Dirac cone surface state and 3D Dirac fermions in the bulk is difficult. To the best of our knowledge, $ZrTe_5$ is the only 3D topological insulator in the history of material science, which has Dirac fermionic excitation in the bulk. Following the present work, the above-mentioned conclusion has been supported by Manzoni *et al.* through ARPES experiments [131].

5.5 Conclusion

Although, the long-standing debate on the resistivity anomaly in $ZrTe_5$ somewhat comes to an end, the exact topological nature of the electronic band structure remains elusive till today. Theoretical calculations predicted that bulk $ZrTe_5$ to be either a weak or a strong three-dimensional (3D) topological insulator. However, the angle resolved photoemission spectroscopy and transport measurements clearly demonstrate 3D Dirac cone state with a small mass gap between the valence band and conduction band in the bulk. From the magnetization and magneto-transport measurements on $ZrTe_5$ single crystal, we have detected both the signature of helical spin texture from topological surface state and chiral anomaly associated with the 3D Dirac cone state in the bulk. This implies that $ZrTe_5$ hosts a novel electronic phase of material, having massless Dirac fermionic excitation in its bulk gap state, unlike earlier reported 3D topological insulators. Apart from the band topology, it is also apparent from the resistivity and Hall measurements that the anomalous peak in the resistivity can be shifted to a much lower temperature ($T<2$ K) by controlling doping.

6

Anisotropic transverse magnetoresistance and Fermi surface in $TaSb_2$

6.1 Introduction

Without taking into account the role of spin-orbit coupling, $TaSb_2$ has been proposed to be a topological semimetal. Upon inclusion of spin-orbit coupling, however, gap opens-up at each band crossing point [132, 133, 134, 135]. This leads to the possibility of suppressed linear electronic dispersion in $TaSb_2$. On the other hand, the transport experiments have established the 3D Dirac fermionic excitation through the observation of negative longitudinal magnetoresistance (LMR) and detection of non-trivial π Berry's phase in Landau level index plot [132, 135]. So, every further investigation is complementary to the previous results on the electronic band topology of $TaSb_2$. Apart from this unconventional nature of electronic band structure, large magnetoresistance and the presence of two or three Fermi pockets depending on the position of the Fermi level, have been reported in

earlier works by analyzing the Shubnikov-de Haas (SdH) oscillation for magnetic field along one of the crystallographic axes [132, 134, 135]. Due to the lower symmetry (monoclinic) of crystal structure of $TaSb_2$, one expects a strong anisotropy in Fermi surface of this system. However, the crystallographic direction dependence of magnetotransport properties and the anisotropy of the Fermi surfaces have not been probed so far. This is important not only for understanding different electronic properties controlled by the Fermi surface but also helpful for the application point of view. In the present work, we have observed large anisotropy in magnetoresistance when the angle between magnetic field and crystallographic axes is varied in transverse experimental configuration (i.e., field is perpendicular to the current direction). In this set up, the field direction is kept fixed and the sample is rotated with respect to the field direction. Besides this, employing magnetization measurements along three mutually perpendicular directions on the same single crystal and by analysing the de Haas-van Alphen oscillation, we report the anisotropic nature of the Fermi pockets.

6.2 Sample preparation, characterization, and experimental details

6.2.1 Sample preparation

Single crystals of $TaSb_2$ were grown using iodine vapor transport technique in two steps. At first, polycrystalline sample is prepared by heating the stoichiometric mixture of high-purity Ta powder and Sb pieces at 650°C for 8 h and at 750°C for 48 h in a vacuum-sealed quartz tube. Next, the polycrystalline sample along with

the required amount of iodine were sealed under vacuum in another quartz tube. Finally, the quartz tube was placed in a gradient furnace and heated for 7 days. During heating, the end of the quartz tube containing the sample was maintained at 1000°C, while the other end was kept at 900°C. The furnace was then cooled slowly to room temperature. Several small, shiny and niddle-like crystals formed at the cold end of the tube were mechanically extracted for transport and magnetic measurements.

6.2.2 Characterization

Phase purity and the structural analysis of the samples were done by using both the high resolution transmission electron microscopy (HRTEM) and the powder x-ray diffraction (XRD) technique. The HRTEM image of a representative piece of sample, which has been taken from a single crystal of $TaSb_2$ is shown in Figure 6.1(a). Very clear periodic lattice structure implies that there is no secondary phase or atom clustering or disorder in the present sample. The Fourier-filtered image of the selected region in the inset, shows inter-planar spacings (d-spacing) of 2.88 Å and 2.32 Å. These measured d-spacings are close to the (111), and (003) inter-planar spacings of $TaSb_2$ (JCPDS # 65-7656). Figure 6.1(b) and Figure 6.1(c) show the selected area electron diffraction (SAD) pattern recorded along [100] and [110] zone axis, respectively. The periodic pattern of the spots in SAD implies high-quality single crystalline nature of the grown samples. The diffraction pattern was indexed using the lattice parameters of monoclinic $TaSb_2$. The energy-dispersive x-ray (EDX) spectrum, as shown in Figure 6.1(d), confirms the presence of the elements in desired stoichiometry. Please note that the carbon and copper peaks in spectrum appear from the carbon coated copper grid on which the sample

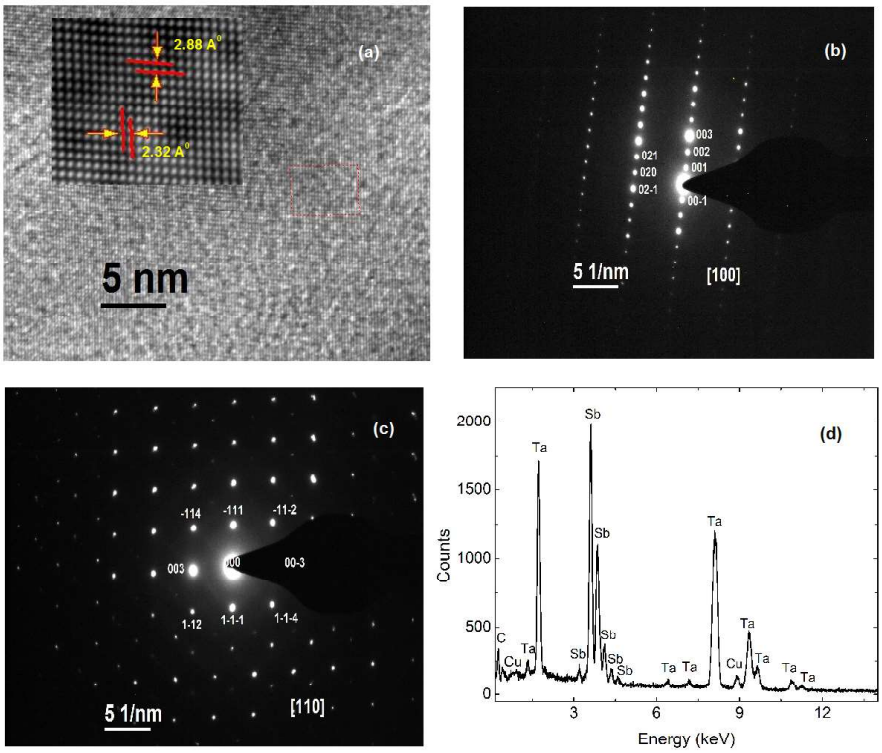

Figure 6.1: (a) High resolution TEM image, taken on a representative piece of $TaSb_2$ single crystal. Inset shows the Fourier-filtered image of the red dotted region. (b) and (c) are the selected area electron diffraction (SAD) patterns taken along [100] and [110] zone axis, respectively. (d) The energy-dispersive X-ray (EDX) spectroscopy data.

was mounted for TEM analysis. Figure 6.2(a) shows the high-resolution x-ray diffraction pattern of the powdered sample of $TaSb_2$ crystals at room temperature. Within the resolution of XRD, we did not see any peak due to the impurity phase. Using the Rietveld profile refinement, we have calculated the lattice parameters a=10.221, b=3.645 and c=8.291 Å, and β=120.40° with space-group symmetry $C_{12/m1}$. A sketch map of the crystal structure of $TaSb_2$ has been shown in Figure 6.2(b).

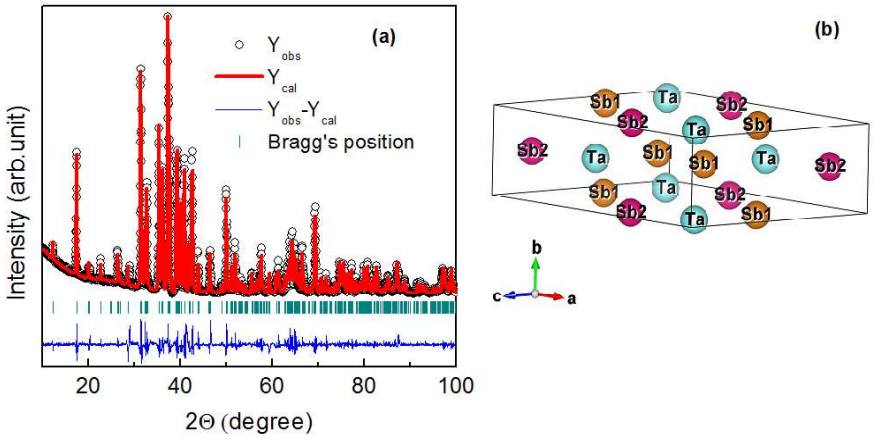

Figure 6.2: (a) X-ray diffraction pattern of powdered single crystals of $TaSb_2$. Black open circles are experimental data (Y_{obs}), red line is the calculated pattern (Y_{cal}), blue line is the difference between experimental and calculated intensities (Y_{obs}-Y_{cal}), and green lines show the Bragg positions. (b) Schematic diagram for the crystal structure of $TaSb_2$.

6.2.3 Experimental details

The transport measurements on $TaSb_2$ single crystals were done with the help of standard four-probe technique in a 9 T physical property measurement system (Quantum Design). The electrical contacts were made using silver epoxy [Epotec, USA] and thin gold wire. The magnetization was measured in a 7 T MPMS3 (Quantum Design).

6.3 Results

6.3.1 Temperature dependence of resistivity

Figure 6.3(a) shows a representative single crystal of $TaSb_2$ with four electrical contacts. The typical length of the single crystals is ∼2 mm. This type of material,

known as transition metal dipnictide MPn_2 [M = V, Nb, Ta, Cr, Mo, and W, Pn = P, As, and Sb], grows preferentially along **b**-axis. As a consequence, the longer direction of the crystal is the **b**-axis [136, 137]. The crystallographic **a**-axis is perpendicular to **b**-axis, and both the axes lie on the largest flat plane of the crystal. Because of the monoclinic structure of the material, crystallographic **c**-axis is not perpendicular to **ab** plane. For convenience, we have considered three mutually perpendicular directions on the crystal as reference. Two of them are the crystallographic **a**- and **b**-axis, and the third one is perpendicular to **ab** plane, i.e., (001) direction. The zero-field resistivity (ρ_{xx}) is metallic over the whole temperature range, as shown in Figure 6.3(b). ρ_{xx} shows strong T dependence. Small value of ρ_{xx} at 2 K ($\sim$ 0.75 $\mu\Omega$ cm) and the large residual resistivity ratio, ρ_{xx}(300 K)/ρ_{xx}(2 K)$\sim$ 130, indicate good quality of the single crystals. With the application of magnetic field, the low-temperature resistivity drastically enhances. As a result, a metal- to semiconductor-like crossover behavior starts to appear with decreasing temperature. With the increase in field strength, the semiconducting-like behavior becomes more and more prominent, and the metal- to semiconductor-like crossover temperature (T_m) shifts towards higher temperature side, as evident from the inset of Figure 6.3(b). Unlike T_m, the temperature (T_i) at which $d\rho_{xx}/dT$ exhibits a minimum is almost independent of the strength of the magnetic field and remains fixed at $\sim$ 20 K. Slightly below T_i, the saturation-like behavior in $\rho_{xx}(T)$ starts to appear. The magnetic field induced metal-semiconductor crossover and the low-temperature resistivity plateau are the common phenomena in topological semimetals [78, 79, 80, 132, 134, 138, 139]. Different explanations such as magnetic field induced gap opening at the Dirac node [79, 139] and Kohler's scaling of magnetoresistance [140] have been proposed as possible origin.

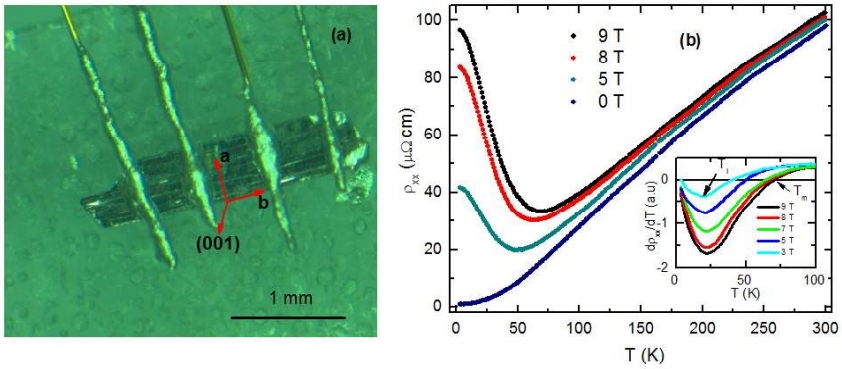

Figure 6.3: (a) Typical morphology and different crystallographic directions of a representative single crystal of $TaSb_2$, and (b) Temperature dependence of resistivity (ρ_{xx}) both in presence and absence of external magnetic field. Current (I) is applied along **b**-axis and magnetic field (B) is perpendicular to the **ab** plane. Inset shows the first order derivative of ρ_{xx} with respect to T. Metal- to semiconductor-like crossover temperature is named as T_m, and T_i is the temperature for the inflection point of $\rho_{xx}(T)$.

6.3.2 Angular dependence of magnetoresistance

Several topological semimetals like $NbSb_2$, ZrSiS and $TaAs_2$ show highly crystallographic direction dependent magnetoresistance, which arises due to the anisotropy in their Fermi surface [136, 137, 141, 142, 143, 144, 145]. Figure 6.4(a) shows the transverse magnetoresistance ($B \perp I$) for the $TaSb_2$ single crystal at 2 K with the rotation of sample about **b**-axis. When the field is along the (001) direction, the MR, which is defined as $[\rho_{xx}(B)\text{-}\rho_{xx}(0)]/\rho_{xx}(0)$, is $\sim 1.3\times10^4\%$ at 9 T and $\sim 4\times10^3\%$ at 5 T. As the sample is rotated from $B\|(001)$ to $B\|\mathbf{a}$, the value of MR is observed to increase and becomes maximum ($\sim 2\times10^4\%$ at 9 T) at around $\theta = 75°$. MR is minimum $\sim 9500\%$ at around 165°. The polar plot in Figure 6.4(a) shows a two-fold rotational symmetry, which is consistent with the monoclinic crystal structure of the present sample. The tilted pattern of MR(θ) with respect to the

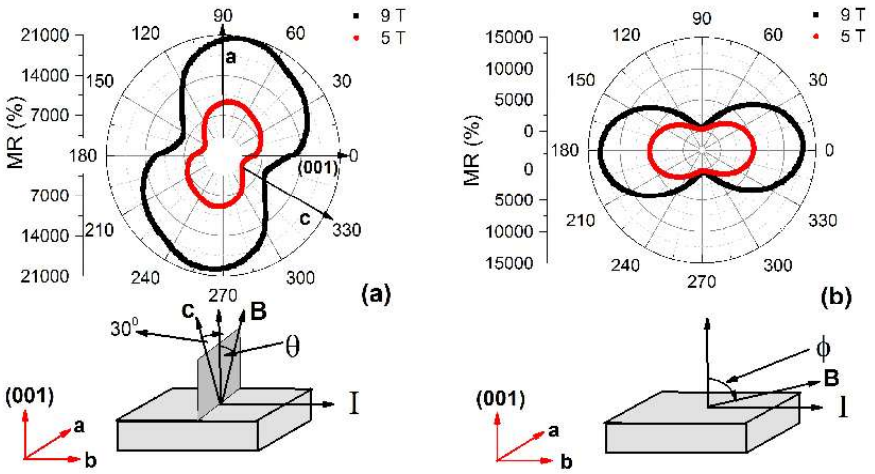

Figure 6.4: (a) Anisotropic magnetoresistance of a representative $TaSb_2$ single crystal at 2 K when the sample is rotated form $B \parallel (001)$ to $B \parallel$**a**-axis configuration, making an angle θ between B and (001) direction. (b) Magnetoresistance of the same piece of single crystal at 2 K when the angle (90° - ϕ) between I and B has been changed at two representative field strengths 5 and 9 T.

crystallographic axis may be due to the complex geometry of the Fermi surfaces and their relative contribution to transport [137, 146].

Figure 6.4(b) shows the typical behavior of MR at 2 K when the angle (90°-ϕ) between I and B has been varied continuously. As expected, due to the orbital origin of MR, the maximum and minimum in MR appear at $\phi = 0°$ and $\phi = 90°$, respectively. This also confirms that there is no intrinsic misalignment between I and B in our crystal. Within the resolution of the angular variation of horizontal sample rotator, we have not observed any detectable negative MR under $B \| I$ configuration, i.e., in longitudinal set up. To further verify, we have also measured the field dependence of MR at small angle interval ($\sim 1°$) around $\phi = 90°$. The field dependence of MR at $\phi = 90°$ configuration has been shown and discussed in

the next section. We have repeated the same experiment on other single crystals but failed to detect any negative MR for ϕ close to 90°. This implies that the negative longitudinal MR (NLMR) is either absent or weak in competition with unavoidable misalignment induced positive MR in the present compound. In this context, it is worthy to mention that the NLMR has been reported in isostructural compounds $TaAs_2$ and $NbAs_2$ by Li *et al.* [135]. But, the subsequent work has established that the NLMR in $TaAs_2$ and $NbAs_2$ is due to the inhomogeneous current distribution inside the sample, i.e., due to the current jetting effect [137]. The NLMR disappears when the electrical contacts are made correctly [137].

6.3.3 Field dependence of MR

We have measured the field dependence of magnetoresistance in longitudinal configuration to confirm the absence of negative LMR. Over the entire window from zero to 9 T, the LMR is positive and increases with increasing field, as shown in Figure 6.5(a) at some representative temperatures from 2 to 100 K. Considering magnetoresistance $\sim$ 13000-20000 % in transverse experimental configuration, one can find that the misalignment angle between current and magnetic field is very small $\sim 0.5°$ in longitudinal configuration. This unavoidable misalignment induced small positive LMR is very hard to eliminate in an experiment, and frequently found in literature [137]. Additionally, the asymmetry between the negative and positive field sections of MR is less than 3% of the total MR in longitudinal configuration. This also implies that the Hall contribution to our resistivity data is very small and contacts are good in quality.

Figure 6.5(b) shows the field dependence of MR for $B\|(001)$ and $I\|\mathbf{b}$ configuration. The large non-saturating MR up to 9 T suppresses with increasing temper-

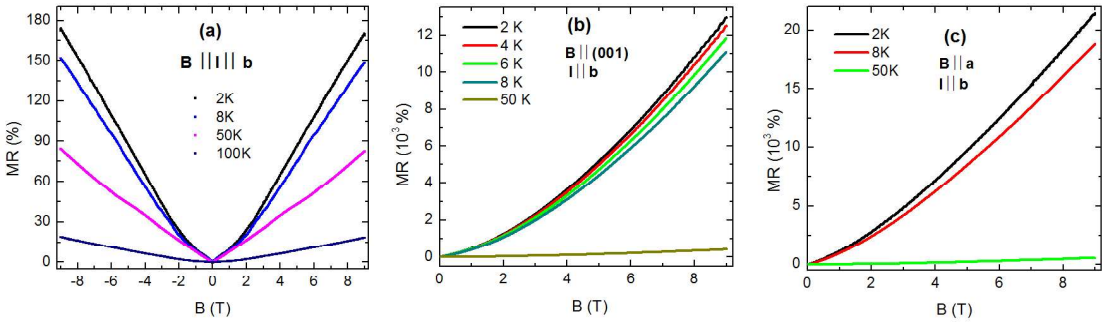

Figure 6.5: Magnetoresistance as a function of magnetic field at some representative temperatures for (a) $B \parallel I \parallel \mathbf{b}$ configuration, (b) $B \parallel (001)$ and $I \parallel \mathbf{b}$ configuration, and (c) for $B \parallel \mathbf{a}$ and $I \parallel \mathbf{b}$ configuration.

ature. Over the entire field range, MR shows approximately $\sim B^{1.5}$ dependence. Below 5 K, a high frequency Shubnikov-de Haas effect has been observed in the high-field region. Due to very small amplitude of the oscillation, it is difficult to extract the oscillatory part from the large background, using polynomial fit. The amplitude of oscillation also suppresses very rapidly with increasing temperature. So, we have employed the de Haas-van Alphen oscillation in magnetization measurements to probe the Fermi surface. Figure 6.5(c) shows MR *vs* B for $B \parallel \mathbf{a}$ and $I \parallel \mathbf{b}$ configuration. The value of MR is larger in this direction as evident from Figure 6.4(a), and suppresses rapidly with increasing temperature.

6.3.4 Hall measurements and multi-band analysis

We have also measured the field dependence of Hall resistivity (ρ_{yx}), and this has been shown in Figure 6.6(a). Over the whole temperature and field range ρ_{yx} is negative and exhibits weak superlinear B dependence. This indicates the presence of more than one types of charge carriers and electron dominated transport in $TaSb_2$. As three Fermi pockets have been detected in the present de Haas-van Alphen

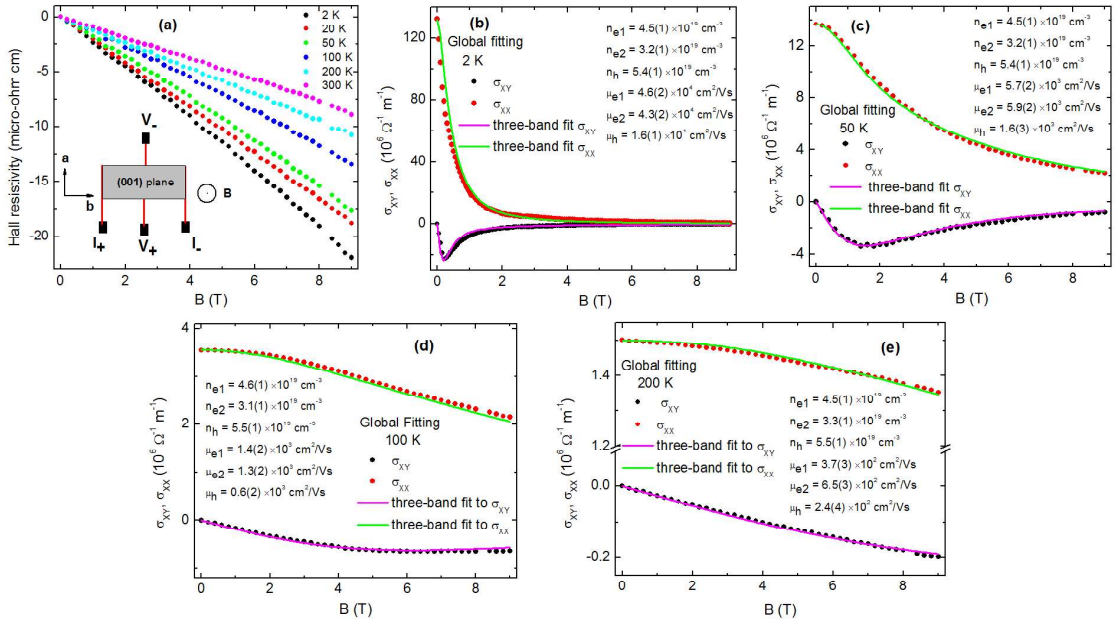

Figure 6.6: (a) The field dependence of Hall resistivity (ρ_{yx}) and its evolution with temperature. The Hall measurement has been performed in $B\|(001)$ and $I\|\mathbf{b}$ configuration. Inset shows the schematic of the Hall measurement setup. (b), (c), (d), and (e) show the simultaneous (i.e., global) three-band analysis of electrical conductivity (σ_{xx}) and Hall conductivity (σ_{xy}) data at 2 K, 50 K, 100 K, and 200 K, respectively. The black dots represent the field dependence of Hall conductivity (σ_{xy}) and the red dots represent the field dependence of electrical conductivity (σ_{xx}). The green and magenta curves are the three-band fit to the experimental data with the expression, $\sigma_{xx}=\sum_{i=1}^{3}\frac{en_i\mu_i}{1+\mu_i^2B^2}$ and $\sigma_{xy}=\sum_{i=1}^{3}S_i\frac{en_i\mu_i^2B}{1+\mu_i^2B^2}$, respectively. The density and mobility for each types of charge carrier have been mentioned in the inset.

oscillation, which will be discussed in the following sections, we have performed three-band analysis of the electrical conductivity (σ_{xx}) and Hall conductivity (σ_{xy}) to determine μ and carrier density (n) of the individual Fermi pockets. At first, the $\sigma_{xx}(B)=\frac{\rho_{xx}}{\rho_{xx}^2+\rho_{yx}^2}$ and $\sigma_{xy}(B)=\frac{\rho_{yx}}{\rho_{xx}^2+\rho_{yx}^2}$ have been determined, using the experimental $\rho_{yx}(B)$ and $\rho_{xx}(B)$ [56]. The field dependence of σ_{xy} in a system of N carrier species is given by the expression, $\sigma_{xy}(B)=\sum_{i=1}^{N} S_i\frac{en_i\mu_i^2B}{1+\mu_i^2B^2}$, where S_i is +1 for holes and -1 for electrons [147]. The analogous expression for electrical conductivity is $\sigma_{xx}(B)=\sum_{i=1}^{N}\frac{en_i\mu_i}{1+\mu_i^2B^2}$. Figures 6.6(b)-(e) represent the simultaneous three-band fit to the electrical conductivity (σ_{xx}) and Hall conductivity (σ_{xy}) data at representative temperatures 2 K, 50 K, 100 K, and 200 K. This type of fitting, which is also known as global fitting, includes parameter sharing between the two expressions to obtain the best fit solutions. Analysis reveals two electron-type Fermi pockets with carrier density $n_{e1} \sim 4.5(1)$ and $n_{e2} \sim 3.2(1)$ $\times 10^{19}$ cm^{-3}, and one hole-type Fermi pocket with $n_h \sim 5.4(1)\times 10^{19}$ cm^{-3}. It has been found that the mobility of hole-type carrier ($\sim 1.6\times 10^4$ cm^2/Vs at 2 K) is much smaller compared to the electrons from the smaller Fermi pockets. The mobility of electrons from the Fermi pockets of intermediate and smallest volume are $\sim 4.6(2)$ and $4.3(2)\times 10^4$ cm^2/Vs, respectively, at 2 K. This coexistence of electron- and hole-type charge carriers supports the earlier experimental and theoretical works on $TaSb_2$ [133, 134, 135]. The ratio $\frac{n_e}{n_h} \sim 1$ also supports the electron-hole compensation mechanism as a possible origin for large and non-saturating magnetoresistance in this family of materials (MPn_2) [132, 137, 148, 149].

6.3.5 Probing the Fermi surface through de Haas-van Alphen oscillation

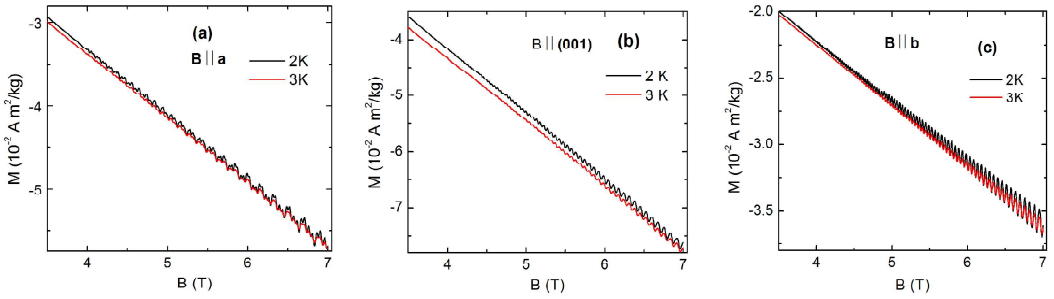

Figure 6.7: Field dependence of magnetization (M) for (a) B $\|$**a**, (b) B $\|$(001), and (c) B $\|$**b** configurations.

To probe the Fermi surface of $TaSb_2$, we measured the field dependence of magnetization (M) of the representative piece of single crystal, and observed prominent de Haas-van Alphen oscillations within 7 T magnetic fields (Figure 6.7). Taking the first order derivative of M with respect to B, the oscillating component of the susceptibility has been obtained and shown in the Figure 6.8(a) for $B\|$**a** configuration. From the figure, it is evident that the oscillation amplitude rapidly suppresses with increasing temperature and above 6 K, the amplitude is too small to detect within the experimental field range. The fast Fourier transform (FFT) spectrum in Figure 6.8(b) shows three distinct oscillation frequencies (F) at 156, 327 and 598 T. Oscillations in the field range 4 to 7 T has been used in FFT for all experimental configurations. Below 4 T, the dHvA oscillation amplitude is too weak to analyze accurately. The obtained values of frequency imply that there are three Fermi pockets in the present sample, similar to that observed in earlier SdH oscillation measurement, where the frequency peaks have been reported at 55, 234

and 487 T [134]. On the other hand, Li *et al.* have observed only two frequency peaks at 220 and 465 T in their SdH oscillation study [132]. Although there are considerable differences between the experimental findings, all of these appear to be allowed for $TaSb_2$ crystals. This is due to the fact that $TaSb_2$ hosts multiple electronic bands close to the Fermi level and it is not a perfectly compensated semimetal [133]. The elaborated discussion is given in the following paragraph.

MPn_2 class of materials show non-saturating magnetoresistance, which can be ascribed to near compensation of electrons and holes. However, in some compounds including $TaSb_2$, the electron and hole density have not been always found to be very close or completely equal to each other in spite of the fact that all the samples show non-saturating MR [132, 144, 150]. Although, the magnetotransport experiment on $TaSb_2$ by Wang *et al.* [134] shows the near perfect compensation of electrons and holes, Li *et al.* [132] have observed electron dominated transport. Besides the experimental observations, the band structure and density functional theory calculation also show that the ratio of electron to hole density of states at the Fermi level is 1.25:1 for $TaSb_2$, and it is not a completely compensated semimetal [133]. This experimental and reported theoretical findings suggest that there is a redundancy in the prefect carrier compensation in $TaSb_2$, which does not affect the non-saturation field dependence of MR. If we consider a small deviation in the value of $\frac{n_e}{n_h}$ from 1, it can include or exclude the contribution of small Fermi pocket or change the volume of Fermi pockets significantly, depending on the position of Fermi level from sample to sample due to uncontrolled doping.

Employing the Onsager relation $F=(\phi_0/2\pi^2)A_F$, the cross-sectional areas of

the Fermi surfaces normal to the field direction ($B\|\mathbf{a}$) have been calculated and listed in TABLE I. A significant difference in A_F of the Fermi pockets has been observed along this direction. The damping of the oscillation amplitude (FFT peak intensity) with temperature can be described by the thermal damping term of the Lifshitz-Kosevich formula, as discussed in chapter 3 and chapter 4:

$$\Delta R_T = a\frac{2\pi^2 k_B T/\hbar\omega_c}{\sinh(2\pi^2 k_B T/\hbar\omega_c)}. \tag{6.1}$$

Figure 6.8(c) shows the fitting of the FFT peak intensity as a function of temperature with equation (1). Using the extracted value of ω_c from the fitting, the effective cyclotron mass of the charge carrier (m_{eff}) and the Fermi velocity (v_F) are obtained from the relations ω_c=eB/m_{eff} and v_F=$\hbar k_F/m_{eff}$, respectively. The calculated parameters are shown in TABLE I. The effective mass of the charge carrier for all the three Fermi pockets are smaller than the rest mass of free electron and similar to that reported in earlier SdH oscillation study [134]. Considering spherical approximation with frequency 598 T along all the momentum directions, the over-estimated value of carrier density for the largest Fermi pocket has been found to be $\sim 8 \times 10^{19}$ cm^{-3}, using the expression, $\Delta\left(\frac{1}{B}\right) = \frac{2e}{\hbar}\left(\frac{g_s g_v}{6\pi^2 n_{3D}}\right)^{2/3}$ [59]. Here, $\Delta\left(\frac{1}{B}\right)$, g_s, and g_v are the period of the oscillation, spin degeneracy, and valley degeneracy of the Fermi pockets, respectively. This value of carrier density from the quantum oscillation study is comparable with the value obtained from three-band analysis. The above comparison for a representative Fermi pocket supports the reliability of the values of parameters, determined by the three-band fitting.

The results of magnetization measurement and the details of dHvA oscillation

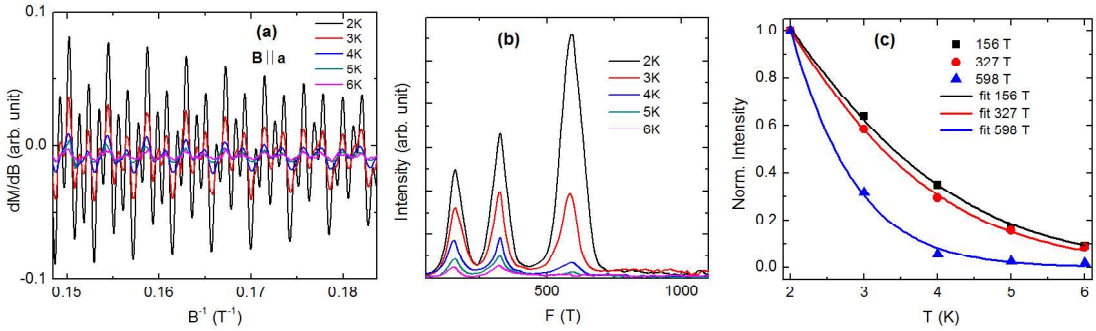

Figure 6.8: (a) Oscillating part of dc susceptibility ($\Delta\chi$), which has been obtained by taking the first order derivative of magnetization (M), as a function of $1/B$ for $B\|\mathbf{a}$-axis configuration. (b) The oscillation frequencies after the fast Fourier transformation (FFT). Oscillations in the field range 4 to 7 T has been used for FFT. (c) Thermal damping of the normalized FFT peak intensity. The solid line is a fit to the Lifshitz-Kosevich formula [equation (1)].

Table 6.1: Parameters associated to the Fermi surface of $TaSb_2$, when the field is applied along the **a**-axis. A_F is the Fermi surface cross-section. m_{eff} is the effective mass of the charge carrier and v_F is the Fermi velocity.

Frequency T	A_F 10^{-3}Å^{-2}	m_{eff} m_0	v_F 10^5m/s
156(2)	14.8	0.32(1)	2.5
327(2)	31.1	0.35(1)	3.3
598(3)	56.8	0.59(1)	2.6

Table 6.2: Parameters associated to the Fermi surface of $TaSb_2$, when the field is applied perpendicular to ab plane i.e., along the (001) direction.

Frequency T	A_F 10^{-3}Å^{-2}	m_{eff} m_0	v_F 10^5m/s
370(2)	35.2	0.32(1)	3.9
421(4)	40.1	0.37(1)	3.5
452(3)	43.0	0.41(1)	3.4

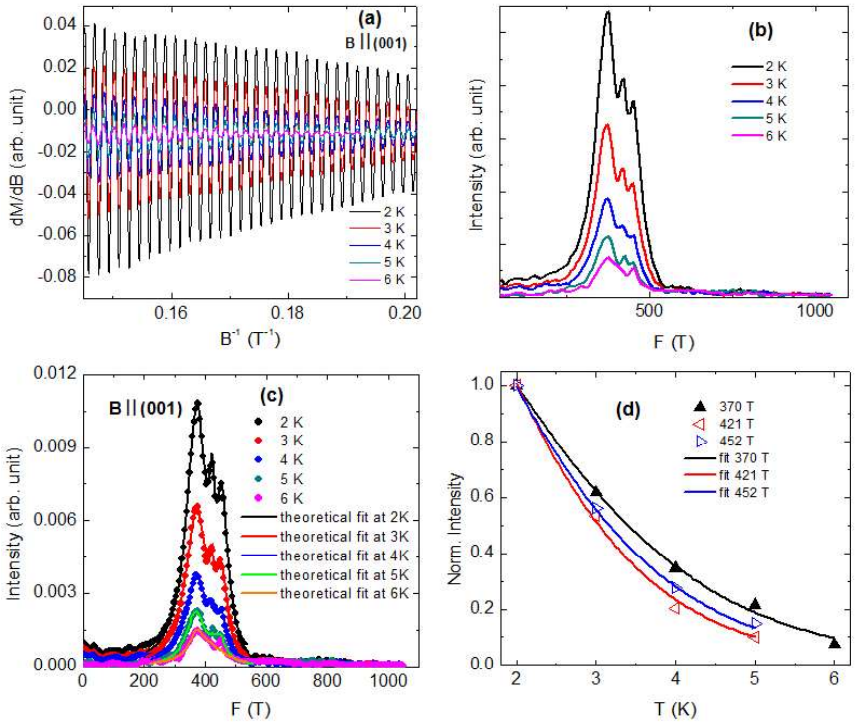

Figure 6.9: a) $\Delta\chi$ versus $1/B$ for $B\|(001)$ configuration. (b) The oscillation frequencies after the fast Fourier transformation. Oscillations in the field range 4 to 7 T has been used for FFT. (c) Theoretical fitting of the frequency distribution plot for $B\|(001)$ configuration has been shown at different temperatures. The solid circles are the experimental data and the continuous lines are the theoretical fit with the expression, $y=\frac{a}{1+b(x-f_1)^2}+\frac{c}{1+d(x-f_2)^2}+\frac{e}{1+f(x-f_3)^2}$. (d) Temperature dependence of the normalized FFT peak intensity. The solid line is a fit to the Lifshitz-Kosevich formula [equation (1)].

analysis for the field along (001) direction of the same piece of $TaSb_2$ single crystal, have been demonstrated in Figures 6.9(a)-(d). Employing the fast Fourier transformation of the oscillations in Figure 6.9(a), three closely spaced frequency peaks 370, 421 and 452 T have been obtained [Figure 6.9(b)]. As these frequency peaks are not well resolved, there will be significant modification in the peak intensities due to overlap of three frequency distribution curves. So, it will not be wise to calculate m_{eff}, using these intensities of the peaks. To deal with the situation, we have performed extensive theoretical fitting to the intensity vs frequency curves. The frequency distribution of quantum oscillation has been found to be Lorentzian in nature [59]. So, the superposition of three Lorentzian distribution functions, y=$\frac{a}{1+b(x-f_1)^2}+\frac{c}{1+d(x-f_2)^2}+\frac{e}{1+f(x-f_3)^2}$, where a, b, c, d ,e, f, f_1, f_2 and f_3 are the parameters, has been used to fit the experimental data [59]. Good quality of the theoretical fit to the frequency distribution plot is evident from Figure 6.9(c) at the representative temperatures.

The parameters a, c and e, which are nothing but the actual intensity of the frequency peaks, have been determined. The obtained positions of the peaks (f_1, f_2 and f_3), from the fitting, have been found to be within $\pm$5 T of the apparent peak positions in Figure 6.9(b) and listed in TABLE II. The calculated values of A_F reveal nearly equal cross-sectional area of Fermi pockets, unlike to that observed in $B\|\mathbf{a}$. If we compare the values of A_F, the smallest one is $\sim$ 140% and the medium one is $\sim$ 30% higher in B $\|$(001) than the corresponding smallest and medium ones in B $\|\mathbf{a}$, respectively. Whereas, the largest cross-sectional area in B $\|$(001) configuration is 25% smaller compared to its counterpart in B $\|\mathbf{a}$. The intensity of the FFT peaks, deduced from the fittings, have been plotted as

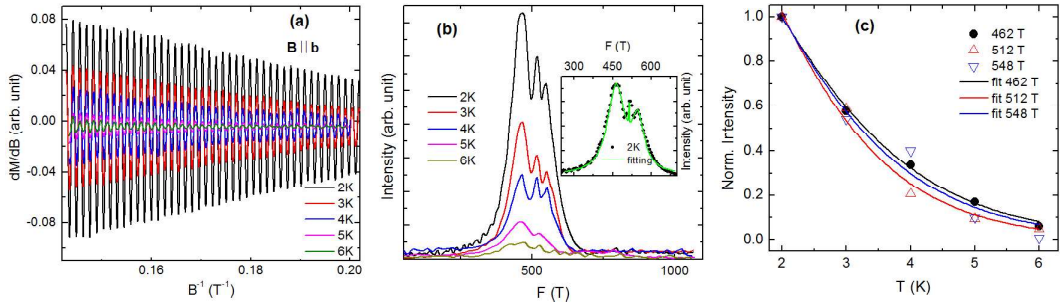

Figure 6.10: (a) $\Delta\chi$ versus $1/B$ for $B\|\mathbf{b}$-axis configuration. (b) The oscillation frequencies after the fast Fourier transformation. Oscillations in the field range 4 to 7 T has been used for FFT. A specimen of the theoretical fitting to the frequency distribution plots has been shown in the inset at 2 K. (c) Thermal damping of the normalized FFT peak intensity. The solid line is a fit to the Lifshitz-Kosevich formula [equation (1)].

a function of temperature in Figure 6.9(d). Employing the thermal damping term of the Lifshitz-Kosevich formula, we have calculated m_{eff} and v_F for all the Fermi pockets and listed in TABLE II. The values of m_{eff} in B ||(001) for the two lighter Fermi pockets are nearly equal to that observed in B ||**a**, and the massive one (also the largest one) is only 30% less in the previous configuration compared to later. Similar magnetic measurements and dHvA oscillation analysis have been done for the field along **b** crystallographic direction and shown in Figures 6.10(a)-(c). Three Fermi pockets of equivalent cross-sectional area have also been found in this configuration. The values of A_F, m_{eff} and v_F for all the frequencies are presented in TABLE III. The values of m_{eff} are close to each other and comparable to that observed in $B\|(001)$. Theoretical fit to the thermal damping of FFT peak intensity has been found to have maximum deviation for 548 T frequency. Even in this case, the standard deviation in the calculated value of m_{eff} is $\sim \pm 0.02 m_0$.

Table 6.3: Parameters associated to the Fermi surface of $TaSb_2$, when the field is applied along the **b**-axis direction.

Frequency T	A_F 10^{-3}Å^{-2}	m_{eff} m_0	v_F 10^5m/s
462(3)	44.0	0.34(1)	4.0
512(5)	48.6	0.39(1)	3.7
548(4)	52.1	0.35(2)	4.2

6.4 Discussions

Transverse magnetoresistance of orbital origin has been shown to scale with the mobility of charge carriers in the plane perpendicular to the applied B [146, 151]. For an example, the typical field dependence of electrical conductivity is given by $\sigma(B) \sim \frac{ne\mu}{1+\mu^2B^2}$ [146, 150, 152]. As mobility is a tensor quantity in presence of B, the anisotropic behavior of magnetoresistance can be explained by taking into account the anisotropy in the mobility tensor [151]. The following discussion on angular dependence of MR in terms of anisotropy in Fermi surfaces is based on the assumption 'each pocket provides only one dHvA frequency and the dHvA frequencies do not interchange among the three pockets when the field direction is changed'. The mobility of charge carrier in a material is determined by the ratio of the scattering time (τ) to the m_{eff}, $\mu \sim \frac{\tau}{m_{eff}}$. From the analysis of dHvA oscillation, we have seen that two Fermi pockets of small and intermediate volume have much larger cross-section for B along (001) direction, i.e., perpendicular to ab plane, compared to the **a**-axis. This implies smaller phase space for the scattering of charge carrier from the two Fermi pockets in the plane perpendicular to **a**-axis under application of B, and as a result, the value of τ is larger [151]. Whereas, m_{eff} of charge carriers in these pockets for the above two directions are almost

equal. So, the anisotropy in the scattering time of charge carrier from these two Fermi pockets will govern the anisotropy in their respective mobility tensor. As a consequence, μ of the charge carriers in the plane perpendicular to **a** appears to be higher for these conduction channels. On the other hand, A_F and m_{eff} of largest Fermi pocket have been found to be 25% and 30% smaller, respectively, for B along (001) direction compared to the **a**-axis. So, it appears that the larger Fermi pocket has higher mobility for B along (001) direction compared to the **a**, unlike to that observed in two smaller Fermi pockets. However, the three-band fitting of electrical conductivity and Hall conductivity reveals that μ for the hole-type carriers from the largest Fermi pocket is itself very small; close to one-third of the electron-type charge carriers from the smaller Fermi pockets, and the carrier density of hole pocket is not significantly higher than the individual electron pockets. This suggests that we can ignore the contribution of the largest Fermi pocket in qualitative explanation of anisotropic transverse magnetoresistance, which will be governed by the two electron pockets of small and intermediate volume. As a consequence, the value of magnetoresistance is expected to enhance with the rotation of sample from $B \parallel (001)$ to $B \parallel \mathbf{a}$ configuration.

It is evident from the above discussion that details knowledge on the three-dimensional geometry of the Fermi surface is crucial to explain the direction dependence of electronic properties. Fermi surface anisotropy also determines the effect of uniaxial external perturbation such as, pressure and strain, on electronic properties of a material. In addition, to understand the complex angular variation of different physical properties in a metal such as, specific heat, resistivity, and Pauli paramagnetic susceptibility, information on the anisotropy of electron/hole

effective mass is important. The crystallographic direction dependent MR, observed in present research, can have significant impact in technological application and device fabrication. For example, it can be used in magnetic switches, angular position sensors, etc. We strongly believe that the present result on the Fermi surface anisotropy and magnetotransport properties of $TaSb_2$ will motivate the material science community for similar or more extensive research on other members of MPn_2 family. The three-dimensional geometry of the Fermi surfaces can be constructed by observing the continuous evolution of the frequency peak associated to a particular Fermi pocket, through extensive magnetization measurements at a small angle interval between the crystallographic directions and B. However, such type of facility is beyond our reach at this moment.

6.5 Conclusion

In conclusion, we have observed a large anisotropy in transverse magnetoresistance of $TaSb_2$ single crystal, by varying the angle between magnetic field and crystallographic axes. The large nonsaturating magnetoresistance has the maximum value $\sim 2\times10^4\%$ and the minimum value $\sim 9.5\times10^3\%$ at 2 K and 9 T, with the rotation of sample about **b**-axis, keeping the field direction fixed. Employing the magnetization measurement and analyzing the prominent de Haas-van Alphen oscillation, we observe three Fermi pockets. Applying field along three mutually perpendicular directions of the crystal, the cross-sectional area of the Fermi pockets has been observed to vary. Three-band fitting of electrical and Hall conductivity reveals two high mobility electron-type Fermi pockets with smaller carrier density, and a larger hole pocket with much lower carrier mobility. However, no large difference has been found between the density of electrons and holes. The coexistence

of electrons and holes of comparable density supports the electron-hole compensation mechanism as a possible origin for large and non-saturating magnetoresistance in MPn_2 family of materials. Combining the present results of three-band analysis and quantum oscillation study, the crystallographic direction dependence of transverse magnetoresistance in $TaSb_2$ has been qualitatively explained.

7

Summary and future directions

7.1 Summary

The present thesis addresses some unique magnetotransport properties, nature and geometry of Fermi surfaces, non-trivial transport or magnetic responses from novel electronic states, and scattering mechanism of charge carriers in some 3D Dirac semimetals. We have grown high quality single crystal of the compound through chemical vapor transport technique, and performed extensive electronic transport, quantum oscillations, magnetic, and thermopower measurements. Cd_3As_2, $ZrTe_5$, and $TaSb_2$ are the candidate materials, which have been chosen for the present thesis.

We have probed the Fermi surface of Cd_3As_2 through de Haas-van Alphen oscillation technique. The results are presented and discussed in chapter 3. The values of the Fermi wave vector, Fermi velocity, and effective cyclotron mass of the charge carrier have been calculated and compared to that obtained in Shubnikov-

de Haas oscillation studies. Our dHvA experiment reveals two distinct frequencies of oscillations 46 and 53 T along [100], unlike the single frequency along [02$\bar{1}$] and [012]. This suggests that two equivalent cross sections from the two ellipsoidal Fermi surfaces superpose with each other along certain directions. Both the SdH and dHvA oscillation measurements support a nontrivial π Berry's phase, which is the signature of 3D Dirac semimetal phase in Cd_3As_2.

From the magnetoresistivity and Hall measurements, a strong field dependence of scattering time has been observed in Cd_3As_2 and this behavior has been ascribed to the field-induced changes in the FS. As thermoelectric power (S) is a powerful tool to probe the relaxation process in metals and semiconductors and provides complementary information to resistivity, we use S as a probe to study the scattering of charge carrier in Cd_3As_2, under application of magnetic field and with carrier doping. In chapter 4, the saturation value of Seebeck coefficient at high field clearly demonstrates the linear energy dispersion in bulk electronic state. A wide tunability of the charge scattering mechanism has been realized by varying the strength of the magnetic field and carrier density via In doping. With the increase in magnetic field, the scattering time crosses over from being nearly energy independent to a regime of linear dependence. On the other hand, the scattering time enters into the inverse energy-dependent regime and the Fermi surface strongly modifies with 2% In doping at Cd site. With further increase in In content from 2 to 4%, we did not observe SdH oscillation up to 9 T field possibly due to the presence of strong disorder. However, the magnetoresistance is found to be quite large as in the case of undoped sample and unlike to that observed in 2% In doped sample.

Theoretical calculations predicted that bulk $ZrTe_5$ to be either a weak or a strong three-dimensional (3D) topological insulator. However, the angle resolved photoemission spectroscopy and transport measurements clearly demonstrate 3D Dirac cone state with a small mass gap between the valence band and conduction band in the bulk. Chapter 5 describes the results of our magneto-transport and magnetization measurements on $ZrTe_5$ single crystal to address the ambiguity. We have detected a robust zero-field paramagnetic peak in susceptibility due to the helical spin texture associated with the Dirac fermions of the surface state of 3D TI. On the other hand, resistivity measurement under current parallel to magnetic field configuration shows negative magnetoresistance. This implies induced chiral anomaly in $ZrTe_5$, which is the signature of the three-dimensional Dirac fermion in the bulk. Combining both the results, we conclude that $ZrTe_5$ is a novel quantum phase of matter, which hosts both topological Dirac fermions on the surface and three-dimensional Dirac cone state with a mass gap between valence and conduction bands in the bulk. Apart from the band topology, it is also apparent from the resistivity and Hall measurements that the anomalous peak in the resistivity can be shifted to a much lower temperature (T<2 K) by doping.

Chapter 6 is devoted to our magnetotransport and quantum oscillation experiments on the single crystal of $TaSb_2$. By employing a sample rotator, we have revealed highly anisotropic transverse magnetoresistance by rotating the magnetic field along different crystallographic directions. To probe the anisotropy in the Fermi surface, we have performed magnetization measurements and detected strong de Haas-van Alphen (dHvA) oscillations for the magnetic field applied along

a and **b** axes as well as perpendicular to **ab** plane of the crystals. Three Fermi pockets have been identified by analyzing the dHvA oscillations. With the application of magnetic field along different crystallographic directions, the cross-sectional areas of the Fermi pockets have been found significantly different, i.e., the Fermi pockets are highly anisotropic in nature. Three-band fitting of Hall conductivity and electrical conductivity reveals two high mobility electron pockets and one low mobility hole pocket. The angular variation of transverse magnetoresistance has been qualitatively explained using the results of dHvA oscillations and Hall measurements.

7.2 Future directions

The discovery of topological semimetals has emerged as a subject of enormous interest in recent time. These materials having Dirac/Weyl type quasi-particle excitations show different exotic properties of both fundamental and technological interest, some of which have been presented in the thesis. The focus of the current research is to observe new quantum phenomena or to explore new quantum phases of materials, and to understand its microscopic origin for benefit to fundamental research and technological applications. There are some effective paths such as, tuning bulk to surface channel contribution to transport, applying high magnetic field and pressure, and search for new materials beyond the existing electronic/topological classification paradigm, by which the above-mentioned goal can be achieved.

7.2.1 Thickness-dependent magneto-transport in thin films of Dirac/Weyl semimetals

As mentioned in the introduction of this thesis, a 3D Dirac/Weyl semimetal has Fermi arc surface state, electronically decoupled from the bulk. This spin-polarized Fermi-arc surface state can have immense technological impact in spintronic applications. It has been predicted to be a dissipationless channel for charge conduction, useful in fabrication of low-power electronics. However, due to uncontrolled doping during sample preparation, single crystals of these materials, grown so far for transport measurements, have Fermi level much above the bulk Dirac/Weyl nodes, within the range of linear band dispersion. As a consequence, there is huge bulk density of states contribution to transport from 3D Fermi surface, compared to spin-polarized Fermi-arc surface state. The bulk dominated transport phenomena in single crystals of topological semimetals hide the unique electronic response from the surface state. The electronic phenomena associated to the surface state can only be realized in the thin films, where the bulk state contribution to transport will be very low. The magnetotransport measurements on the thin films of different thicknesses can be a useful tool to tune the relative contribution between the surface and bulk state. In addition, gate voltage dependent transport phenomena can also be studied in the thin films. Although, we have a pool of topological semimetals such as, Cd_3As_2, WHM (W = Zr, Hf, La; H = Si, Ge, Sn, Sb; M = O, S, Se, Te), XYBi (X = Ba, Eu, Y = Cu, Ag, Au), Co_2TiX (X = Si, Ge, Sn), RAlX (R = rare-earth, X = Si, Ge), $YbMnBi_2$, LaAlGe, $PtSe_2$, $PtSn_4$, $PtTe_2$, TaAs, TaP, NbAs, NbP, $ZrTe_5$, Hf_2Te_2P, Zr_2Te_2P, $CaMnBi_2$, $SrMnBi_2$, $BaMnBi_2$, $BaZnBi_2$, WP_2, $MoTe_2$, $PdTaSe_2$ and so on, the electronic transport in thin films

have been reported in a very few compounds [153, 154, 155]. So, thickness dependent magneto-transport study on this class of compounds, can be an interesting topic of research in future.

7.2.2 Study of quantum phenomena under extreme conditions (high magnetic field and pressure)

External pressure and magnetic field have been regarded as clean parameters for tuning electronic band structure and electron-electron correlation in a material. High pressure and large magnetic field have been found to create exotic phases in these quantum materials, for example, superconductivity under pressure in Cd_3As_2 and $ZrTe_5$ [156, 157], breakdown of cyclotron orbits in ZrSiS at high magnetic fields [158], magnetic field induced topological phase transition in $ZrTe_5$ [159], quantum limit transport under extreme external field strength , etc. However, the experiments under extreme conditions have been reported in a very few materials. In addition, different new quantum states, other than the above mentioned phases can be observed under extreme conditions, and the new electronic phases can have immense impact in fundamental research and possibly useful in technological applications. In this context, investigating quantum phenomena of topological semimetals under high magnetic field and pressure, is an emerging area of research.

7.2.3 Probing electronic transport and Fermi surface of novel materials beyond Dirac/Weyl semimetals

In high-energy physics, the relativistic fermions are protected by Poincare symmetry, while in condensed matter, they respect one of the 230 space group symmetries.

The variation of crystal symmetry from one material to another escalates the potential to explore free fermionic excitations such as Dirac, Weyl, Majorana and beyond. Very recently, Bradlyn *et al.* have predicted the existence of exotic fermions near the Fermi level in several materials, governed by their respective space group symmetry [160]. Unlike two- and four-fold degeneracy in 3D Weyl/Dirac semimetals, these systems exhibit three-, six- , and eight-fold degenerate band crossing at high symmetry points in the Brillouin zone. For example, three-component fermion has recently been observed in molybdenum phosphide [161] and tungsten carbide [162]. Bradlyn *et al.* [160] have suggested several materials, and some of them have reported to exist in single crystal form. So, similar research, as presented in this thesis, can be very useful to understand unique electronic transport and Fermi surface topology of these materials.

8

Appendix

8.1 Appendix A

8.1.1 Magnetization measurements of standard diamagnetic and paramagnetic compounds

We have done magnetization measurements on standard bismuth and palladium samples in SQUID-VSM [MPMS 3, Quantum Design] prior to $ZrTe_5$ single crystal. Figure A8.1(a) shows that linear diamagnetic moment of bismuth at 2, 10 and 100 K passes through the origin. This is more clear from Figure A8.1(b), which shows magnetic field dependence of differential susceptibility ($\chi=\frac{dM}{dB}$). With quantum oscillation at high fields, absence of any paramagnetic peak around zero field implies that the singular paramagnetic susceptibility in $ZrTe_5$ single crystal is not due to any spurious response in our system.

Figure A8.2(a) shows the expected magnetic behaviour of paramagnetic palladium sample, provided by the Quantum Design. Figure A8.2(b) shows the low-field sus-

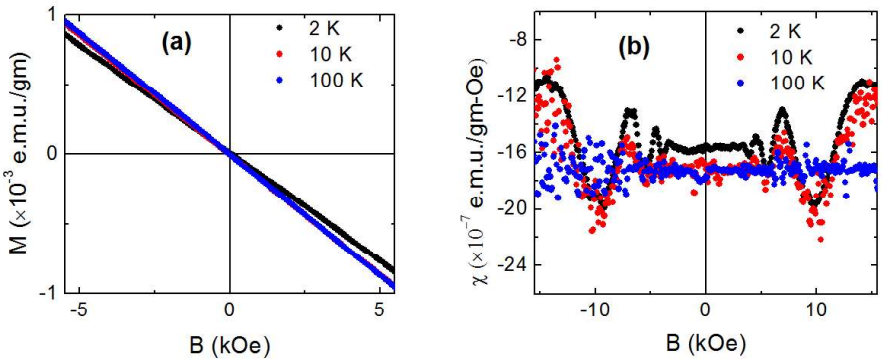

Figure A 8.1: (a) Magnetization measured in SQUID-VSM (Quantum Design) at several representative temperatures for standard diamagnetic bismuth sample. (b) Differential susceptibility ($\chi = \frac{dM}{dB}$) obtained after taking numerical derivative of the magnetization with respect to external magnetic field.

ceptibility of palladium at 2 K and room temperature. The nonlinear behaviour of χ at low field and a broad zero field peak at 2 K are completely suppressed at room temperature. This is entirely different from the singular, robust and linear low-field paramagnetic response from the topological surface state in $ZrTe_5$. For the sake of fundamental interest, we have also measured the magnetization of a single crystal of 3D Dirac semimetal Cd_3As_2, as shown in Figure A8.2(c). This shows perfect diamagnetic behaviour with no paramagnetic sign at low field.

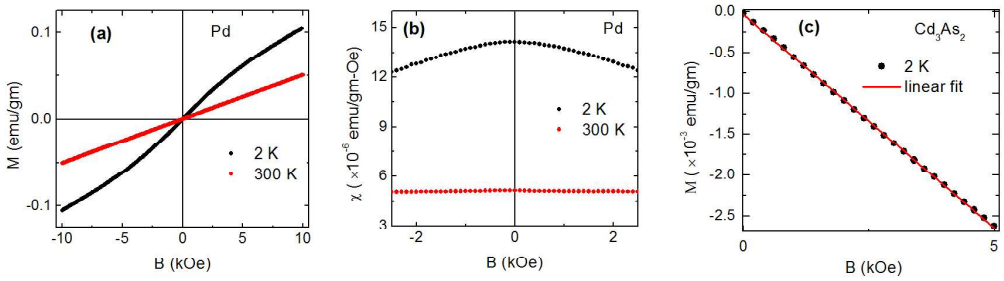

Figure A 8.2: (a) Magnetization of standard paramagnetic palladium sample at 2 and 300 K, (b) $\frac{dM}{dB}$, and (c) Magnetization of single crystal of 3D Dirac semimetal Cd_3As_2. Solid line implies linear fit to the experimental data.

8.1.2 Magnetization measurements of a representative 3D topological insulator

Magnetization measurements have been performed on single crystal of well established three-dimensional topological insulator $Bi_{1.5}Sb_{0.5}Te_{1.7}Se_{1.3}$ using the same experimental setup. We have observed singular robust paramagnetic susceptibility peak like to that observed in $ZrTe_5$ and shown in Figure A8.3(a) and Figure A8.3(b) at representative temperatures 5 K and 280 K.

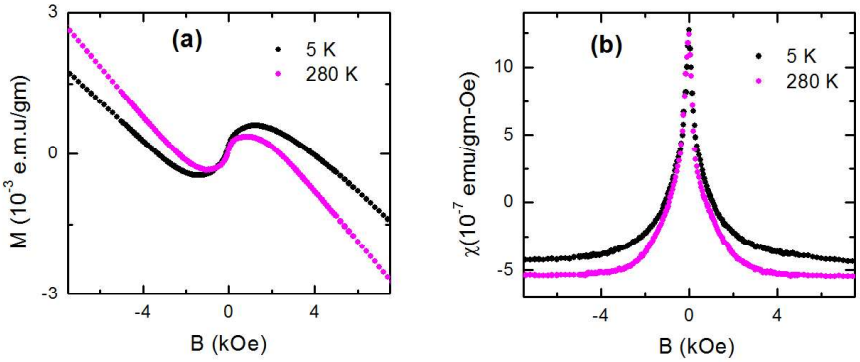

Figure A 8.3: (a) Magnetization (M) vs B of freshly cleaved single crystal of $Bi_{1.5}Sb_{0.5}Te_{1.7}Se_{1.3}$ at temperatures 5 K and 280 K, (b) Susceptibility ($\chi = \frac{dM}{dB}$).

Bibliography

[1] A. Maurya, *Engineering Physics*, Peoples University, Bhopal.

[2] M. Z. Hasan and C. L. Kane, Rev. Mod. Phys. **82**, 3045-3067 (2010).

[3] X.-L. Qi and S.-C. Zhang, Rev. Mod. Phys. **83**, 1057 (2011).

[4] K. V. Klitzing, Phil. Trans. R. Soc. A **363**, 2203-2219 (2005).

[5] M. Nakahara, *Geometry, Topology and Physics*, Institute of Physics Publishing, Bristol and Philadelphia, 2003.

[6] D. J. Thouless, M. Kohmoto, M. P. Nightingale, and M. den Nijs, Phys. Rev. Lett. **49**, 405 (1982).

[7] M. König, S. Wiedmann, C. Brüne, A. Roth, H. Buhmann, L. Molenkamp, X.-L. Qi, and S.-C. Zhang, Science **318**, 766 (2007).

[8] S. Murakami, New Journal of Physics **9**, 356 (2007).

[9] C. L. Kane and E. J. Mele, Phys. Rev. Lett. 95, 226801 (2005).

[10] C. L. Kane and E. J. Mele, Phys. Rev. Lett. 95, 146802 (2005).

[11] L. Fu and C. L. Kane, Phys. Rev. B 74, 195312 (2006).

[12] L. Fu, C. L. Kane, and E. J. Mele, Phys. Rev. Lett. **98**, 106803 (2007).

[13] J. E. Moore and L. Balents, Phys. Rev. B **75**, 121306(R) (2007).

[14] Z. Ringel, Y. E. Kraus, and A. Stern, Phys. Rev. B 86, 045102 (2012).

[15] C. Liu, Y. Lee, T. Kondo, E. D. Mun, M. Caudle, B. N. Harmon, S. L. Bud'ko, P. C. Canfield, and A. Kaminski, Phys. Rev. B **83**, 205133 (2011).

[16] L. Fu and C. L. Kane, Phys. Rev. B **76**, 045302 (2007).

[17] D. Hsieh, D. Qian, L. Wray, Y. Xia, Y. S. Hor, R. J. Cava, and M. Z. Hasan, Nature **452**, 970 (2008).

[18] H. Zhang, C.-X. Liu, X.-L. Qi, X. Dai, Z. Fang, and S.-C. Zhang, Nat. Phys. **5**, 438 (2009).

[19] Y. Xia, D. Qian, D. Hsieh, L. Wray, A. Pal, H. Lin, A. Bansil, D. Grauer, Y. S. Hor, R. J. Cava, and M. Z. Hasan, Nat. Phys. **5**, 398 (2009).

[20] Y. L. Chen, J. G. Analytis, J.-H. Chu, Z. K. Liu, S.-K. Mo, X. L. Qi, H. J. Zhang, D. H. Lu, X. Dai, Z. Fang, S. C. Zhang, I. R. Fisher, Z. Hussain, and Z.-X. Shen, Science **325**, 178 (2009).

[21] D. Hsieh, Y. Xia, D. Qian, L. Wray, F. Meier, J. H. Dil, J. Osterwalder, L. Patthey, A. V. Fedorov, H. Lin, A. Bansil, D. Grauer, Y. S. Hor, R. J. Cava, and M. Z. Hasan, Phys. Rev. Lett. 103, 146401 (2009).

[22] Y. Jiang, Y. Wang, M. Chen, Z. Li, C. Song, K. He, L. Wang, X. Chen, X. Ma, and Q.-K. Xue, Phys. Rev. Lett. 108, 016401 (2012).

[23] M. O. Goerbig and G. Montambaux, arXiv:1410.4098 (2014).

[24] J. C. Y. Teo, L. Fu, and C. L. Kane, Phys. Rev. B **78**, 045426 (2008).

[25] S.-Y. Xu, Y. Xia, L. A. Wray, S. Jia, F. Meier, J. H. Dil, J. Osterwalder, B. Slomski, A. Bansil, H. Lin, R. J. Cava, and M. Z. Hasan, Science **332**, 560 (2011).

[26] S. M. Young, S. Zaheer, J. C. Y. Teo, C. L. Kane, E. J. Mele, and A. M. Rappe, Phys. Rev. Lett. **108**, 140405 (2012).

[27] Z. Wang, Y. Sun, X.-Q. Chen, C. Franchini, G. Xu, H. Weng, X. Dai, and Z. Fang, Phys. Rev. B **85**, 195320 (2012).

[28] Z. Wang, H. Weng, Q. Wu, X. Dai, and Z. Fang, Phys. Rev. B **88**, 125427 (2013).

[29] B. Q. Lv, S. Muff, T. Qian, Z. D. Song, S. M. Nie, N. Xu, P. Richard, C. E. Matt, N. C. Plumb, L. X. Zhao, G. F. Chen, Z. Fang, X. Dai, J. H. Dil, J. Mesot, M. Shi, H. M. Weng, and H. Ding, Phys. Rev. Lett. **115**, 217601 (2015).

[30] H. Z. Weyl, Phys. **56**, 330-352 (1929).

[31] X. Wan, A. M. Turner, A. Vishwanath, and S. Y. Savrasov, Phys. Rev. B **83**, 205101 (2011).

[32] H. Weng, C. Fang, Z. Fang, B. A. Bernevig, and X. Dai, Phys. Rev. X **5**, 011029 (2015).

[33] S.-M. Huang, S.-Y. Xu, I. Belopolski, C.-C. Lee, G. Chang, B. Wang, N. Alidoust, G. Bian, M. Neupane, C. Zhang, S. Jia, A. Bansil, H. Lin, and M. Z. Hasan, Nat. Commun. **6**, 7373 (2015).

[34] S.-Y. Xu, I. Belopolski, N. Alidoust, M. Neupane, G. Bian, C. Zhang, R. Sankar, G. Chang, Z. Yuan, C.-C. Lee, S.-M. Huang, H. Zheng, J. Ma, D. S. Sanchez, B. Wang, A. Bansil, F. Chou, P. P. Shibayev, H. Lin, S. Jia, and M. Z Hasan, Science **349**, 613-617 (2015).

[35] B. Q. Lv, H. M. Weng, B. B. Fu, X. P. Wang, H. Miao, J. Ma, P. Richard, X. C. Huang, L. X. Zhao, G. F. Chen, Z. Fang, X. Dai, T. Qian, and H. Ding, Phys. Rev. X **5**, 031013 (2015).

[36] Z. K. Liu, B. Zhou, Y. Zhang, Z. J. Wang, H. M. Weng, D. Prabhakaran, S.-K. Mo, Z. X. Shen, Z. Fang, X. Dai, Z. Hussain, and Y. L. Chen, Science **343**, 864-867 (2014).

[37] Z. K. Liu, J. Jiang, B. Zhou, Z. J. Wang, Y. Zhang, H. M. Weng, D. Prabhakaran, S-K. Mo, H. Peng, P. Dudin, T. Kim, M. Hoesch, Z. Fang, X. Dai, Z. X. Shen, D. L. Feng, Z. Hussain, and Y. L. Chen, Nat. Mater. **13**, 677-681 (2014).

[38] H. Yi, Z. Wang, C. Chen, Y. Shi, Y. Feng, A. Liang, Z. Xie, S. He, J. He, Y. Peng, X. Liu, Y. Liu, L. Zhao, G. Liu, X. Dong, J. Zhang, M. Nakatake, M. Arita, K. Shimada, H. Namatame, M. Taniguchi, Z. Xu, C. Chen, X. Dai, Z. Fang, and X. J. Zhou, Sci. Rep. **4**, 6106 (2014).

[39] S.-Y. Xu, C. Liu, S. K. Kushwaha, R. Sankar, J. W. Krizan, I. Belopolski, M. Neupane, G. Bian, N. Alidoust, T.-R. Chang, H.-T. Jeng, C.-Y. Huang, W.-F. Tsai, H. Lin, P. P. Shibayev, F.-C. Chou, R. J. Cava, and M. Z. Hasan, Science **347**, 294-298 (2015).

[40] H. Weng, X. Dai, and Z. Fang, Phys. Rev. X **4**, 011002 (2014).

[41] Q. Li, D. E. Kharzeev, C. Zhang, Y. Huang, I. PletikosiÄĞ, A. V. Fedorov, R. D. Zhong, J. A. Schneeloch, G. D. Gu, and T. Valla, Chiral magnetic effect in $ZrTe_5$, Nat. Phys. **12**, 550 (2016).

[42] L. M. Schoop, M. N. Ali, C. Straer, A. Topp, A. Varykhalov, D. Marchenko, V. Duppel, S. S. P. Parkin, B. V. Lotsch, and C. R. Ast, Nat. Commun. **7**, 11696 (2016).

[43] R. J. Hill, *The Rietveld Method*, Oxford Univ. press, Oxford, 1995.

[44] J. Rodriguez-Carvajal, *An Introduction to the Program FullProf 2000*, Laboratoire Leon Brillouin, CEA-CNRS, Saclay, 2001.

[45] D. B. Williams and C. Barry Carter, *Transmission Electron Microscopy: A textbook for Material Science*, Springer, New York, 2009.

[46] L. J. V. Pauw, Philips Res. Repts. **13**, 1 (1958).

[47] J. H. Scofield, Rev. Sci. Instrum. **58**, 985 (1987).

[48] Quantum Design, *Physical Properties Measurement Systems, thermal transport Option user's Manual*, Part Number 1684-100B, USA, 2002.

[49] Quantum Design, *Magnetic Property Measurement System: SQUID VSM User's Manual*, 2009.

[50] M. Neupane, S.-Y. Xu, R. Sankar, N. Alidoust, G. Bian, C. Liu, I. Belopolski, T.-R. Chang, H.-T. Jeng, H. Lin, A. Bansil, F. Chou, and M. Z. Hasan, Nat. Commun. **5**, 3786 (2014).

[51] S. Borisenko, Q. Gibson, D. Evtushinsky, V. Zabolotnyy, B. Büchner, and R. J. Cava, Phys. Rev. Lett. **113**, 027603 (2014).

[52] S. Jeon, B. B. Zhou, A. Gyenis, B. E. Feldman, I. Kimchi, A. C. Potter, Q. D. Gibson, R. J. Cava, A. Vishwanath, and A. Yazdani, Nat. Mater. **13**, 851 (2014).

[53] J. Feng, Y. Pang, D. Wu, Z. Wang, H. Weng, J. Li, X. Dai, Z. Fang, Y. Shi, and L. Luyar, Phys. Rev. B **92**, 081306 (2015).

[54] L. P. He, X. C. Hong, J. K. Dong, J. Pan, Z. Zhang, J. Zhang, and S. Y. Li, Phys. Rev. Lett. **113**, 246402 (2014).

[55] A. C. Potter, I. Kimchi, and A. Vishwanath, Nat. Commun. **5**, 5161 (2014).

[56] T. Liang, Q. Gibson, M. N. Ali, M. Liu, R. J. Cava, N. P. Ong, Nat. Mater. **14**, 280 (2015)

[57] Y. Zhao, H. Liu, C. Zhang, H. Wang, J. Wang, Z. Lin, Y. Xing, H. Lu, J. Liu, Y. Wang, S. Jia, X. C. Xie, and J. Wang, Phys. Rev. X **5**, 031037 (2015).

[58] H. Murakawa, M. S. Bahramy, M. Tokunaga, Y. Kohama, C. Bell, Y. Kaneko, N. Nagaosa, H. Y. Hwang, and Y. Tokura, Science **342**, 1490 (2013).

[59] D. Shoenberg, *Magnetic oscillations in metals*. Cambridge University Press, 1984.

[60] K. S. Novoselov, A. K. Geim, S. V. Morozov, D. Jiang, M. I. Katsnelson, I. V. Grigorieva, S. V. Dubonos, and A. A. Firsov, Nature (London) **438**, 197 (2005).

[61] D.-X. Qu, Y. S. Hor, J. Xiong, R. J. Cava, and N. P. Ong, Science **329**, 821 (2010).

[62] A. Narayanan, M. D. Watson, S. F. Blake, Y. L. Chen, D. Prabhakaran, B. Yan, N. Bruyant, L. Drigo, I. I. Mazin, C. Felser, T. Kong, P. C. Canfield, A. I. Cold, Phys. Rev. Lett. **114**, 117201 (2015).

[63] J. Cao, S. Liang, C. Zhang, Y. Liu, J. Huang, Z. Jin, Z. Chen, Z. Wang, Q. Wang, J. Zhao, S. Li, X. Dai, J. Zou, Z. Xia, L. Li, and F. Xiu, Nat. Commun. **6**, 7779 (2015).

[64] A. Pariari, P. Dutta, and P. Mandal, Phys. Rev. B **91**, 155139 (2015).

[65] I. Rosenman, J. Phys. Chem. Solids **30**, 1385 (1969).

[66] E. Zhang, Y. Liu, W. Wang, C. Zhang, P. Zhou, Z.-G. Chen, J. Zou and F. Xiu, ACS Nano **9**, 8843 (2015).

[67] P. Wei, W. Bao, Y. Pu, C. N. Lau, and J. Shi, Phys. Rev. Lett. **102**, 166808 (2009).

[68] K. Masumoto and S. Isomura, Energy Conversion **10**(3), 129, (1970).

[69] Y. M. Zuev, W. Chang, and P. Kim, Phys. Rev. Lett. **102**, 096807 (2009).

[70] L. L. Korenblit and V. E. Sherstobitov, Sov. Phys. Semicond. **2**, 573 (1968).

[71] D. Armitage and H. J. Goldsmid, J . Phys. C **2**, 2389 (1969).

[72] Z. -G. Chen, C. Zhang, Y. Zou, E. Zhang, L. Yang, M. Hong, F. Xiu, and J. Zou, Nano Lett. **15**, 5830 (2015).

[73] E. H. Hwang, E. Rossi, and S. Das Sarma, Phys. Rev. B **80**, 235415 (2009).

[74] K. Ziegler, Phys. Rev. Lett. **97**, 266802 (2006).

[75] E. Pallecchi, A. C. Betz, J. Chaste, G. Fève, B. Huard, T. Kontos, J.-M. Berroir, and B. Plaçais, Phys. Rev. B **83**, 125408 (2011).

[76] R. Lundgren, P. Laurell, and G. A. Fiete, Phys. Rev. B **90**, 165115 (2014).

[77] Y.-W. Tan, Y. Zhang, K. Bolotin, Y. Zhao, S. Adam, E. H. Hwang, S. Das Sarma, H. L. Stormer, and P. Kim, Phys. Rev. Lett. **99**, 246803 (2007).

[78] M. N. Ali, J. Xiong, S. Flynn, J. Tao, Q. D. Gibson, L. M. Schoop, T. Liang, N. Haldolaarachchige, M. Hirschberger, N. P. Ong, and R. J. Cava, Nature **514**, 205 (2014).

[79] C. Shekhar, A. K. Nayak, Y. Sun, M. Schmidt, M. Nicklas, I. Leermakers, U. Zeitler, Y. Skourski, J. Wosnitza, Z. Liu, Y. Chen, W. Schnelle, H. Borrmann, Y. Grin, C. Felser, and B. Yan, Nat. Phys. **11**, 645 (2015).

[80] Z. J. Yue, X. L. Wang, and S. S. Yan, Appl. Phys. Lett. **107**, 112101 (2015).

[81] E. H. Hwang and S. Das Sarma, Phys. Rev. B **77**, 115449 (2008).

[82] M. M. Parish and P. B. Littlewood, Nature (London) **426**, 162 (2003).

[83] A. Husmann, J. B. Betts, G. S. Boebinger, A. Migliori, T. F. Rosenbaum, and M.-L. Saboungi, Nature (London) **417**, 421 (2002).

[84] J. Hu, T. F. Rosenbaum, and J. B. Betts, Phys. Rev. Lett. **95**, 186603 (2005).

[85] S. Furuseth, L. Brattas, and A. Kjekshus, Acta Chem. Scand. **27**, 2367-2374 (1973).

[86] E. F. Skelton et al., Solid State Commun. **42**, 1-3 (1982).

[87] S. Okada, T. Sambongi, and M. Ido, J. Phys. Soc. Jpn. **49**, 839-840 (1980).

[88] R. Y. Chen *et al.*, Phys. Rev. B **92**, 075107 (2015).

[89] T. E. Jones, W. W. Fuller, T. J. Wieting, and F. Levy, Solid State Commun. **42**, 793-798 (1982).

[90] M. Izumi, K. Uchinokura, E. Matsuura, and S. Harada, Solid State Commun. **42**, 773-778 (1982).

[91] N. P. Ong, and P. Monceau, Phys. Rev. B **16**, 3443 (1977).

[92] S. Okada *et al.*, J. Phys. Soc. Jpn. **51**, 460-467 (1982).

[93] M. Rubinstein, Phys. Rev. B **60**, 1627 (1999).

[94] D. N. McIlroy *et al.*, J. Phys.: Condens. Matter **16**, L359-L365 (2004).

[95] T. M. Tritt *et al.*, Phys. Rev. B **60**, 7816 (1999).

[96] G. Manzoni *et al.*, Phys. Rev. Lett. **115**, 207402 (2015).

[97] R. Y. Chen *et al.*, Phys. Rev. Lett. **115**, 176404 (2015).

[98] Y. Zhou *et al.*, Proc. Natl. Acad. Sci. USA **113**(11), 2904-2909 (2016).

[99] X. Yuan *et al.*, NPG Asia Materials **8**, e325 (2016).

[100] J. Niu *et al.*, Phys. Rev. B **95**, 035420 (2017).

[101] R. Wu *et al.*, Phys. Rev. X **6**, 021017 (2016).

[102] W. Yu *et al.*, Sci. Rep. **6**, 35357 (2016).

[103] Y. Zhang *et al.*, Nat. Commun. **8**, 15512 (2017).

[104] F. J. DiSalvo, R. M. Fleming, and J. V. Waszczak, Phys. Rev. B **24**, 2935 (1981).

[105] H. Fjellvg and A. Kjekshus, Solid State Commun. **60**, 91-93 (1986).

[106] S. Okada, T. Sambongi, and M. Ido, J. Phys. Soc. Jpn. **49**, 839 (1980).

[107] R. T. Littleton IV *et al.*, Phys. Rev. B **64**, 121104(R) (2001).

[108] T. Liang *et al.*, Nat. Phys. **14**, 451-455 (2018).

[109] M. Izumi *et al.*, J. Phys. C: Solid State Phys. **20**, 3691 (1987).

[110] S. L. Adler, Phys. Rev. **177**, 2426 (1969).

[111] J. S. Bell and R. Jackiw, Il Nuovo Cimento A **60**, 47-61 (1969).

[112] H. B. Nielsen and M. Ninomiya, Phys. Lett. B **130**, 389-396 (1983).

[113] E. V. Gorbar, V. A. Miransky, and I. A. Shovkovy, Phys. Rev. B **88**, 165105 (2013).

[114] C. Z. Li *et al.*, Nat. Commun. **6**, 10137 (2015).

[115] H. -J. Kim *et al.*, Phys. Rev. Lett. **111**, 246603 (2013).

[116] X. Huang *et al.*, Phys. Rev. X **5**, 031023 (2015).

[117] G. Zheng *et al.*, Phys. Rev. B **93**, 115414 (2016).

[118] J. Xiong *et al.*, Science **350**, 413 (2015).

[119] D. Hsieh *et al.*, Nature **460**, 1101 (2009).

[120] H. Zhang, C. -X. Liu, and S. -C. Zhang, Phys. Rev. Lett. **111**, 066801 (2013).

[121] L. Zhao *et al.*, Nat. Mater. **13**, 580 (2014).

[122] S. G. Buga *et al.*, Chem. Phys. Lett. **631-632**, 97 (2015).

[123] X. He *et al.*, Phys.Rev.Lett. **110**, 156101(2013).

[124] M. S. Bahramy *et al.*, Nat. Commun. **3**,1159(2012).

[125] H. Murakawa *et al.*, Science **342**, 1490 (2013).

[126] J. Jiang *et al.*, Phys. Rev. Lett. **115**, 166601 (2015).

[127] M. Z. Hasan and C. L. Kane, Rev. Mod. Phys. **82**, 3045 (2010).

[128] A. Kitaev, AIP Conf. Proc. **1134**, 22 (2009).

[129] B. Yan, M. Jansen, and C. A Felser, Nat. Phys. **9**, 709-711 (2013).

[130] B. Yan and S.-C. Zhang, Rep. Prog. Phys. **75**, 096501 (2012).

[131] G. Manzoni *et al.*, Phys. Rev. Lett. **117**, 237601 (2016).

[132] Y. Li *et al.*, Phys. Rev. B **94**, 121115(R) (2016).

[133] C. Xu, J. Chen, G. X. Zhi, Y. Li, J. Dai, and C. Cao, Phys. Rev. B **93**, 195106 (2016).

[134] Z. Wang *et al.*, Preprint at https://arxiv.org/abs/1603.01717 (2016).

[135] Y. Li *et al.*, Preprint at https://arxiv.org/abs/1603.04056 (2016).

[136] K. Wang, D. Graf, L. Li, L. Wang, and C. Petrovic, Sci. Rep. **4**, 7328 (2014).

[137] Z. Yuan, H. Lu, Y. Liu, J. Wang,and S. Jia, Phys. Rev. B **93**, 184405 (2016).

[138] Y. Zhao *et al.*, Phys. Rev. B **92**, 041104(R) (2015).

[139] F. F. Tafti, Q. D. Gibson, S. K. Kushwaha, N. Haldolaarachchige, and R. J. Cava, Nat. Phys. **12**, 272-277 (2016).

[140] Y. L. Wang *et al.*, Phys. Rev. B **92**, 180402(R) (2015).

[141] M. N. Ali *et al.*, Sci. Adv. **2**, e1601742 (2016).

[142] R. Singha, A. Pariari, B. Satpati, and P. Mandal, Proc. Natl. Acad. Sci. **114**, 2468-2473 (2017).

[143] J. Hu *et al.*, Phys. Rev. Lett. **117**, 016602 (2016).

[144] Y. Luo *et al.*, Sci. Rep. **6**, 27294 (2016).

[145] R. Singha, A. Pariari, B. Satpati, and P. Mandal, Phys. Rev. B **96**, 245138 (2017).

[146] A. Collaudin, B. Fauqué, Y. Fuseya, W. Kang, and K. Behnia, Phys. Rev. X **5**, 021022 (2015).

[147] Y. Gui *et al.*, J. Appl. Phys. **84**, 4327 (1998).

[148] B. Shen, X. Deng, G. Kotliar, and N. Ni, Phys. Rev. B **93**, 195119 (2016).

[149] Y. -Y. Wang, Q. -H. Yu, P. -J. Guo, K. Liu, and T. -L. Xia, Phys. Rev. B **94**, 041103(R) (2016).

[150] R. Singha, A. Pariari, G. K. Gupta, T. Das, and P. Mandal, Phys. Rev. B **97**, 155120 (2018).

[151] Z. Zhu, A. Collaudin, B. FauquÃľ, W. Kang, and K. Behnia, Nat. Phys. **8**, 89-94 (2012).

[152] C. Jacoboni, *Theory of Electron Transport in Semiconductors*, Springer, Berlin, 2010.

[153] M. Uchida *et al.*, Nat. Commun. **8**, 2274 (2017).

[154] J. Hellerstedt *et al.*, Nano Lett. **16**, 3210 (2016).

[155] J. Niu *et al.*, PRB **95**, 035420 (2017).

[156] L. He *et al.*, npj Quantum Materials **1**, 16014 (2016).

[157] Y. Zhou *et al.*, PNAS **113**, 2904 (2016).

[158] S. Pezzini *et al.*, Nat. Phys.14, 178 (2018).

[159] G. Zheng *et al.*, Phys. Rev. B **96**, 121401(R) (2017).

[160] B. Bradlyn *et al.*, Science **353** (6299), aaf5037 (2016).

[161] B. Q. Lv *et al.*, Nature **546**, 627 (2017).

[162] J. -Z. Ma *et al.*, Nat. Phys. **14**, 349 (2018).